

AD-A089 456

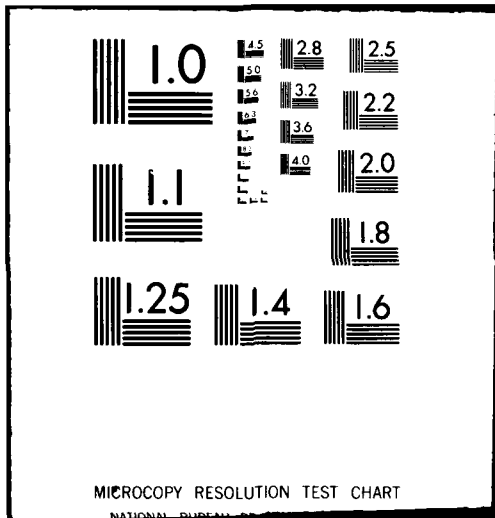
GEORGIA INST OF TECH ATLANTA ENGINEERING EXPERIMENT --ETC F/8 20/7  
GROWTH AND CHARACTERIZATION OF IN(1-X)GA(X)AS(Y)P(1-Y) AND SAAS--ETC(U)  
MAR 80 D W COVINGTON, E L MEEKS, W H HICKLIN N00173-79-C-0033

UNCLASSIFIED

NL

1 of 2

AD-A089 456



AD A089456

# LEVEL II

Ⓟ

## GROWTH AND CHARACTERIZATION OF $\text{Al}_x\text{Ga}_{1-x}\text{As}$ , $\text{Ga}_{1-x}\text{As}_x\text{P}_{1-y}$ , AND $\text{GaAs}$ USING MOLECULAR BEAM EPITAXY

Annual Report  
A-1981

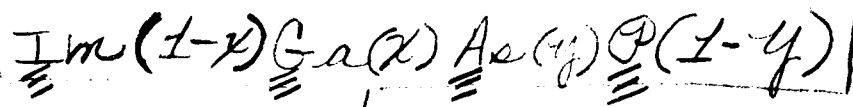
by  
D. M. Carrington, E. L. Marks, and W. H. Hockett

DTIC  
ELECTE  
SEP 24 1981  
S D  
E

PHYSICS RESEARCH LABORATORY  
WASHINGTON, D. C. 20375

Contract No. N00075-78-C-0033  
Reporting Period 1 February 1978 - 7 February 1980

REPRODUCTION OF THIS DOCUMENT IS UNLIMITED



6  
GROWTH AND CHARACTERIZATION OF  $\text{In}_{1-x}\text{Ga}_x\text{As}_y\text{P}_{1-y}$   
AND GaAs USING MOLECULAR BEAM EPITAXY,

9 Annual Report, 9 Feb 79 - 7 Feb 80

10 D.W. Covington, E.L. Meeks and W.H. Hicklin

A-2291

Engineering Experiment Station  
Georgia Institute of Technology  
Atlanta, Georgia 30332

11  
March 1980

12 1271

Report for Period 9 February 1979 - 7 February 1980

Contract No. N00173-79-C-0033<sup>new</sup>

15

Prepared for  
Naval Research Laboratory  
Washington, D.C. 20375

253 850

JB

PREFACE

This report describes work primarily performed at the Georgia Institute of Technology Engineering Experiment Station under Contract No. N00173-79-C-0033 during the period 9 February 1979 through 7 February 1980. Funding for the program is provided by Mr. Nate Butler of the Naval Electronics Systems Command. The Scientific Officer responsible for the technical administration of the program is Dr. John E. Davey of the Naval Research Laboratory.

General contributions to this report were supplied by D.W. Covington, E.L. Meeks, and W.H. Hicklin. The following specific contributions are gratefully acknowledged. Auger sputter profiles and SIMS profiles of Fe-doped, MBE GaAs layers were supplied by Dr. J.E. Davey (NRL) and Dr. Jim Comas (NRL), respectively. Photoluminescence spectra of Fe-doped layers were taken by Dr. P.W. Yu (University of Dayton). Dr. P.E. Mackie, Jr. (Georgia Tech) ran the X-ray rocking curves of the ternary and quaternary MBE samples. Additional information on the crystal structure of the compound alloy semiconductor films is contained in the reflection electron diffraction data generated by Dr. J.E. Davey (NRL) and Mr. J.W. Johnson (Georgia Tech).

Accession For	
NTIS GRA&I	<input checked="" type="checkbox"/>
DDC TAB	<input type="checkbox"/>
Unannounced	<input type="checkbox"/>
Justification	<input type="checkbox"/>
<i>Letter on File</i>	
By _____	
Distribution/	
Availability Codes	
Dist.	Avail and/or special
<i>A</i>	

*summary*

SUMMARY

*less than but close to*

This report describes the technical work accomplished during the first year of a two-year study of binary and quaternary semiconductors grown by molecular beam epitaxy. Research on GaAs materials demonstrated doping profiles for peeled film, mixer diodes and low-high-low, millimeter wave IMPATT diodes. Iron has been investigated as a potential MBE dopant for FET buffer layer applications. Although compensated layers exhibiting the  $Fe_{L1}^{(2+)}$  line at 0.371 eV were obtained for doping oven temperatures  $\approx 1013^\circ C$  at GaAs growth rates of  $1.0 \mu m/hr$ , there was unintentional accumulation of iron at the outer surface reserved for the active layer in conventional FET structures. Before initiating the study of quaternary materials, the MBE growth conditions were established for the ternary  $In_x Ga_{1-x} As$ . Layers of the latter semiconductor grown on GaAs substrates held at  $510^\circ C$  showed significant changes in surface morphology and electrical properties for  $x \geq 0.3$ . A cryopumped MBE system containing six oven positions has been developed for growing the quaternary  $In_{1-x} Ga_x As_y P_{1-y}$  which requires relatively intense beams of P molecules. Lattice-matched  $In_{1-x} Ga_x As_y P_{1-y}$  layers have been deposited in this system on (001) GaAs substrates using ovens loaded with Ga, In, As, and GaP. Epitaxy was achieved. Compositional inhomogeneties, however, may be suggested by the breadth of the X-ray rocking curve data for  $In_{1-x} Ga_x As_y P_{1-y}$  layers  $\leq 2.0 \mu m$  thick. The presence of P appears to reduce the lateral extent of group III-stabilized growth beneath shadow masked regions.

*greater than but close to*

## TABLE OF CONTENTS

	<u>Page</u>
LIST OF TABLES . . . . .	vii
LIST OF ILLUSTRATIONS . . . . .	ix
CHAPTER	
1.0 INTRODUCTION . . . . .	1
1.1 OVERVIEW . . . . .	1
1.2 PROGRAM GOALS . . . . .	7
1.3 PRINCIPAL RESULTS . . . . .	8
2.0 DESIGN AND OPERATION OF MBE SYSTEMS . . . . .	11
2.1 CONFIGURATION OF QUATERNARY MBE SYSTEM . . . . .	11
2.2 OPERATING TECHNIQUES . . . . .	18
2.2.1 Molecular Flux Measurements . . . . .	18
2.2.2 Shuttering Molecular Beam Sources . . . . .	24
2.2.3 Unintentionally Doped GaAs . . . . .	27
3.0 MATERIALS FOR GaAs DEVICES . . . . .	31
3.1 INVERTED PROFILE MIXER DIODES . . . . .	31
3.2 LOW-HIGH-LOW MILLIMETER WAVE IMPATT DIODES . . . . .	32
4.0 IRON DOPING STUDIES . . . . .	37
4.1 ANALYSIS OF IRON MOLECULAR BEAMS . . . . .	38
4.2 INCORPORATION OF IRON IN MBE GaAs . . . . .	42
4.2.1 General Characteristics . . . . .	42
4.2.2 Auger Analysis of Doping Profiles . . . . .	44
4.2.3 SIMS Analysis of Doping Profiles . . . . .	47
4.2.4 Photoluminescence Spectra . . . . .	52
4.2.5 Electrical Properties . . . . .	54

	<u>Page</u>
5.0 INVESTIGATION OF TERNARY SEMICONDUCTORS . . . . .	64
5.1 GROWTH OF $\text{In}_x\text{Ga}_{1-x}\text{As}$ ON InP . . . . .	65
5.1.1 Oven Temperatures and Ternary Compositions . . . . .	65
5.1.2 Passivation of InP Substrates . . . . .	65
5.1.3 Material Properties . . . . .	71
5.2 GROWTH OF $\text{In}_x\text{Ga}_{1-x}\text{As}$ ON GaAs . . . . .	77
5.2.1 Morphology and Composition . . . . .	77
5.2.2 Electrical Properties . . . . .	81
6.0 INVESTIGATION OF QUATERNARY SEMICONDUCTORS . . . . .	87
6.1 GROWTH OF $\text{In}_{1-x}\text{Ga}_x\text{As}_y\text{P}_{1-y}$ LATTICE-MATCHED TO GaAs . . . . .	87
6.2 ANALYSIS OF STRUCTURE AND COMPOSITION . . . . .	89
6.3 PATTERNED GROWTH OF MULTICOMPONENT ALLOYS USING SHADOW MASKING . . . . .	95
7.0 FUTURE WORK . . . . .	102
APPENDIX I. EFFECT OF CARRIER CONCENTRATION, COMPENSATION AND TEMPERATURE UPON THE MOBILITY OF ELECTRONS IN GaAs . . . . .	103
APPENDIX II. COMPOSITION OF ALLOY SEMICONDUCTORS DETERMINED FROM X-RAY ROCKING CURVES . . . . .	105
REFERENCES . . . . .	107

## LIST OF TABLES

<u>Table No.</u>	<u>Page</u>
1. Deposition Parameters and Electrical Properties (296 °K) of Unintentionally Doped GaAs Layers Grown on Cr-Doped (001) GaAs in the Quaternary MBE System . . . . .	28
2. Characteristics of MBE IMPATT Diodes . . . . .	36
3. Summary of Deposition Parameters and Properties of Fe-Doped GaAs Layers Grown by MBE on (001) GaAs . . . . .	43
4. Deposition Parameters, Thicknesses, and Electrical Properties for Fe-Doped Epilayers Grown on Cr-Doped (001) GaAs . . . . .	57
5. InP Substrate Cleaning Procedure . . . . .	67
6. Deposition Parameters, Compositions, and Electrical Properties for MBE $\text{In}_x\text{Ga}_{1-x}\text{As}$ Layers Grown Directly on (001) InP Substrates . . . . .	72
7. Deposition Parameters, Compositions, and Electrical Properties of MBE $\text{In}_x\text{Ga}_{1-x}\text{As}$ Layers Grown Directly on (001) GaAs Substrates . . . . .	83
8. Mobilities Reported for $\text{In}_x\text{Ga}_{1-x}\text{As}$ Layers Grown on GaAs Substrates . . . . .	85
9. Deposition Parameters and Compositions for MBE $\text{In}_{1-x}\text{Ga}_x\text{As}_y\text{P}_{1-y}$ Layers Grown on (001) GaAs Substrates Held at 510 °C . . . . .	88
10. Composition x in $\text{In}_{1-x}\text{Ga}_x\text{As}_y\text{P}_{1-y}$ by Step Height and Auger Analyses . . . . .	101

## LIST OF ILLUSTRATIONS

<u>Figure No.</u>	<u>Page</u>
1. Energy Gap Data for $\text{In}_{1-x}\text{Ga}_x\text{As}_y\text{P}_{1-y}$ Which Match Lattice Constants for InP and GaAs Substrates . . . . .	3
2. Details of Cryopump Connections for Evacuating the Growth and Interlock Chambers . . . . .	12
3. Quaternary MBE System . . . . .	14
4. Source Flange Open and Rotated for Loading or Adjustments . . . . .	14
5. Major Components of the Growth Chamber of the Quaternary MBE System . . . . .	16
6. Source Holder for Quaternary MBE System . . . . .	17
7. Source Oven Assembly . . . . .	18
8. Impingement Rates for the Direct Components of P, As, In, Ga, and Fe Molecular Beams Incident Upon an Ion Gauge Located 9.0 cm from the Oven Aperture . . . . .	21
9. Transients in the Molecular Beam Intensity of a S'uttered MBE Oven Under Thermocouple Control . . . . .	25
10. Hall Mobility vs. Temperature for p-Type, Unintentionally Doped GaAs Layers Grown in the Quaternary MBE System . . . . .	29
11. Low-High-Low Doping Profiles for MBE B0427 Showing Details of the Spike near the Surface and the Interface 1.2 $\mu\text{m}$ Deep Between the Drift Region and the Buffer Layer . . . . .	34
12. Low-High-Low Doping Profiles for MBE B0501 Showing Details of the Spike near the Surface and the Interface 1.0 $\mu\text{m}$ Deep Between the Drift Region and the Buffer Layer . . . . .	35
13. Mass Spectrum of Fe Isotopes Emitted as a Function of Iron Oven Temperature . . . . .	39

<u>Figure No.</u>	<u>Page</u>
14. Doping Concentration vs. Fe Oven Temperature . . . . .	41
15. Auger Spectra Showing Fe at the Surface of GaAs Epilayers Grown at 540 °C and 520 °C . . . . .	45
16. Auger Spectra Showing Trace of Fe at the Surface of GaAs MBE B0327 Grown at 480 °C . . . . .	46
17. Profile of Iron Concentration Near the Surface of Two Fe-Doped GaAs Layers Grown by MBE . . . . .	48
18. SIMS Profile Showing the Segregation of <sup>56</sup> Fe which was Initially Introduced as a Surface Doping Spike (Dotted) During the MBE Growth of GaAs Layer B0613 . . . . .	50
19. SIMS Profile Showing the Segregation of <sup>56</sup> Fe which was Initially Introduced as a Central Doping Spike (Dotted) During the MBE Growth of GaAs Layer B0612 . . . . .	51
20. Photoluminescence Spectra Near the Band Edge for Four Fe-Doped GaAs Layers Grown by MBE . . . . .	53
21. Photoluminescence Spectra in the Mid-Band Gap Region for Four Fe-Doped GaAs Layers Grown by MBE . . . . .	55
22. Hall Mobility for Unintentionally Doped and Fe-Doped MBE GaAs Layers vs. Temperature . . . . .	58
23. Mobility vs. Temperature Variation in the n-Type Active Region Deposited on a 1.0 μm Thick Fe-Doped Buffer in Specimen B0411 . . . . .	63
24. Composition and Growth Rate of In <sub>x</sub> Ga <sub>1-x</sub> As as a Function of In and Ga Oven Temperatures . . . . .	66
25. Auger Responses Monitored During the Heating of Passivated InP Substrates Exposed to UHV Overnight and for Three Hours . . . . .	68
26. Auger Spectrums of a Passivated InP Substrate Before and After Heating for 45 Minutes at 350 °C . . . . .	70

<u>Figure No.</u>	<u>Page</u>
27. Rocking Curves of MBE $\text{In}_x\text{Ga}_{1-x}\text{As}$ Layers on InP Substrates . . . . .	73
28. Optical Interference Patterns of the Growth of $\text{In}_x\text{Ga}_{1-x}\text{As}$ Layer MBE B0517 Near a Shadow Clip . . . . .	75
29. Changes in Surface Morphology for $\text{In}_x\text{Ga}_{1-x}\text{As}$ Layers Grown on (001) GaAs Substrates with $0.12 \leq x \leq 0.5$ . . . . .	78
30. Growth Rate of $\text{In}_x\text{Ga}_{1-x}\text{As}$ vs. In Temperature in the Presence of a Constant Flux of Ga Molecules . . . . .	80
31. Pressure of In Molecular Beam vs. Composition x for $\text{In}_x\text{Ga}_{1-x}\text{As}$ Grown With a Constant Ga Pressure of $2 \times 10^{-7}$ Torr . . . . .	82
32. Increase in In Auger Response for MBE $\text{In}_{1-x}\text{Ga}_x\text{As}_y\text{P}_{1-y}$ Layers as the Outer $\text{GaAs}_y\text{P}_{1-y}$ Surface is Removed by Sputtering with 3.0 keV Argon Ions . . . . .	90
33. Auger Spectra of $\text{In}_{1-x}\text{Ga}_x\text{As}_y\text{P}_{1-y}$ Layers Grown by MBE on (001) GaAs . . . . .	91
34. Relative Intensities of (400) Diffraction vs. Bragg Angle for $\text{In}_{1-x}\text{Ga}_x\text{As}_y\text{P}_{1-y}$ Layers on (001) GaAs . . . . .	93
35. Reflection Electron Diffraction Patterns (100 keV, [110] azimuth) for $\text{In}_{1-x}\text{Ga}_x\text{As}_y\text{P}_{1-y}$ Layers on (001) GaAs . . . . .	94
36. Source-Substrate Geometry in the Quaternary MBE System . . . . .	96
37. Shadow Pattern Produced by Noncoincident Molecular Beams of In, Ga, As, and P . . . . .	97
38. Micrograph of the Interference Fringe Pattern of Growth in the Shielded Area of Layer C1109-II, $\text{In}_{0.08}\text{Ga}_{0.92}\text{As}_{0.12}\text{P}_{0.88}$ . . . . .	98

Figure No.

Page

39. Optical Micrograph of  $\text{In}_x\text{Ga}_{1-x}\text{As}$  Layer C1107-II  
Showing the Dark As Shadow in Addition to the Ga  
and In Shadows . . . . . 100

## 1.0 INTRODUCTION

### 1.1 OVERVIEW

This program of basic materials research in molecular beam epitaxy (MBE) is directed toward the growth and analysis of semiconducting layers of the binary, ternary, and quaternary III-V compounds. In MBE, beams from multiple source ovens impinge upon single crystal substrates located in an ultra-high vacuum environment [1]. The process provides almost monoatomic control of the extent and location of the interfaces which separate regions of abrupt or graded changes in semiconductor doping and composition. An objective inherent in this materials study is the identification of fundamental advantages and limitations afforded by the development of MBE materials in devices that perform separate and integrated functions at microwave, millimeter wave, and optical frequencies.

Primary emphasis in the program is focused on the preparation of the quaternary  $\text{In}_x\text{Ga}_{1-x}\text{As}_y\text{P}_{1-y}$  by MBE. In order to introduce changes in refractive indices and absorption coefficients, enhance minority carrier injection, and confine carriers to specific layers; many devices are developed around a heteroepitaxial stack of thin layers with abrupt changes in bandgap energy from one layer to the next. Ternary alloys have a unique value of lattice constant for each composition and bandgap energy. On the other hand, the lattice constants of the quaternary  $\text{In}_{1-x}\text{Ga}_x\text{As}_y\text{P}_{1-y}$  given by [2]

$$a_0 = 0.1894y - 0.4184x + 0.0130xy + 5.8696; \quad (1)$$

can, by carefully selecting the compositions for  $x$  and  $y$ , directly match either GaAs or InP. The direct energy gap for  $\text{In}_{1-x}\text{Ga}_x\text{As}_y\text{P}_{1-y}$  can be

approximated with a cubic surface [3],

$$E_g(x,y) = 1.35 - y + 1.4x - 0.33xy \quad (2)$$
$$- (0.758 - 0.28y) x (1-x)$$
$$- (0.101 + 0.109x) y (1-y) .$$

Simultaneous solutions to Equations 1 and 2 for  $a_{\text{InGaAsP}} = a_{\text{GaAs}}$  and  $a_{\text{InGaAsP}} = a_{\text{InP}}$  are presented in Figure 1. The bandgaps for  $\text{In}_{1-x}\text{Ga}_x\text{As}_y\text{P}_{1-y}$  layers that can be grown on these two substrates span the range 1.88 to 1.43 eV or 0.66 to 0.88  $\mu\text{m}$  (GaAs substrate) and 1.35 to 0.75 eV or 0.92 to 1.73  $\mu\text{m}$  (InP substrate). This flexibility in bandgap engineering is fundamental to the design of efficient optical waveguides and double heterostructure lasers that operate at wavelengths of 1.0 to 1.3  $\mu\text{m}$  where fiber optics show low loss and dispersion [4].

Epitaxial layers of  $\text{In}_{1-x}\text{Ga}_x\text{As}_y\text{P}_{1-y}$  grown primarily by liquid phase epitaxy (LPE) on InP substrates are being extensively investigated for sources and detectors in optical communication systems. Among the sources that have been developed are light emitting diodes (LEDs) emitting at 1.05 to 1.5  $\mu\text{m}$  with external quantum efficiencies on the order of two percent [5-8] and double heterostructure lasers operating in the 1.05 to 1.31  $\mu\text{m}$  range with room temperature threshold current densities as low as  $1500 \text{ A cm}^{-2}$  [9-15]. Progress is also being exhibited in the photodetector field with LPE  $\text{In}_{1-x}\text{Ga}_x\text{As}_y\text{P}_{1-y}$  [16-24]. Quantum efficiencies of 50 to 70 percent are typical for avalanche photodiodes covering the spectral range 0.9 to 1.7  $\mu\text{m}$ . Gains  $> 12$  and rise times  $\leq 150 \times 10^{-12}$  sec have been achieved for these devices.

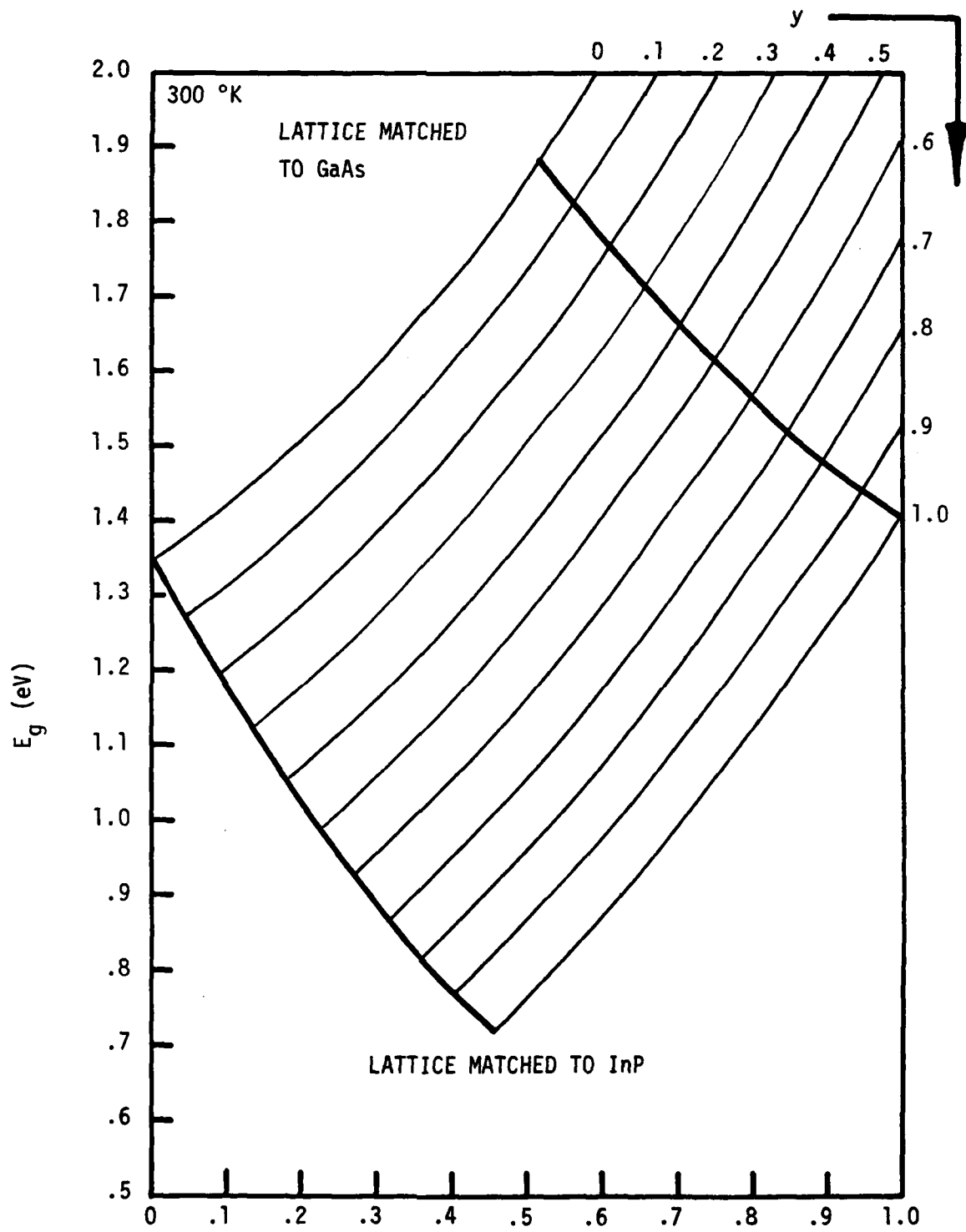


Figure 1. Energy Gap Data for  $\text{In}_{1-x}\text{Ga}_x\text{As}_y\text{P}_{1-y}$  Which Match Lattice Constants for InP and GaAs Substrates.

Theoretical calculations for  $\text{In}_{1-x}\text{Ga}_x\text{As}_y\text{P}_{1-y}$  indicate that this material has significant potential for microwave and millimeter wave devices including field effect transistors (FETs) and transferred electron oscillators (TEOs). In order to increase the current gain cut-off frequency in MESFET devices, the semiconductor material must show higher peak velocities and high low field mobilities at high doping levels. Improvements in both areas are predicted for the quaternary in comparison to either GaAs or InP [25,26]. For doping levels of  $10^{17} \text{ cm}^{-3}$ , the drift mobility of  $\text{In}_{0.73}\text{Ga}_{0.27}\text{As}_{0.6}\text{P}_{0.4}$  is 1.5 to 1.7 times the GaAs mobility, and the maximum drift velocity for the quaternary is 1.4 to 1.6 times the GaAs drift velocity. In addition to the MESFET structure on InP, the heterojunction gate FET configuration may have potential for  $\text{In}_{1-x}\text{Ga}_x\text{As}_y\text{P}_{1-y}$  similar to the  $\text{Al}_{0.5}\text{Ga}_{0.5}$  gate GaAs FETs [27]. Lower leakage currents, self aligning processing, and compatibility with integrated optics technology are projected advantages for heterojunction gate FETs. Large peak-to-valley ratios of 3.1 to 3.6 in the drift velocity-electric field characteristic are computed for  $\text{In}_{0.73}\text{Ga}_{0.27}\text{As}_{0.6}\text{P}_{0.4}$  doped in the  $10^{17} \text{ cm}^{-3}$  level [26]. Since the corresponding ratio for GaAs is 2.1, the quaternary should have an important advantage in maximizing the efficiency of TEO devices. There has been relatively little experimental work to date which demonstrates the actual capabilities of  $\text{In}_{1-x}\text{Ga}_x\text{As}_y\text{P}_{1-y}$  for microwave applications. Layers of  $\text{In}_{0.87}\text{Ga}_{0.13}\text{As}_{0.37}\text{P}_{0.63}$  grown by LPE were processed into a TEO that yielded a peak output power of 2.0 mW at 27.5 GHz with an efficiency of 0.5 percent [28]. A maximum available gain of 5 dB at 10 GHz was observed for FETs with gate dimensions of  $1 \times 200 \mu\text{m}$  that were fabricated in LPE  $\text{In}_{1-x}\text{Ga}_x\text{As}_y\text{P}_{1-y}$  (bandgap of 1.2 eV) grown on InP [29]. Mobilities measured for  $\text{In}_{1-x}\text{Ga}_x\text{As}_y\text{P}_{1-y}$  layers that are lattice-matched to InP generally fall below the theoretically expected values in

the mid-composition range of  $y$  [29,30].

Although MBE is receiving widespread attention in preparing a variety of III-V semiconductors including GaAs [31-33], InP [34-37], GaP [38-42], InAs [43-44], InSb [45],  $Al_xGa_{1-x}As$  [46-52],  $GaAs_yP_{1-y}$  [39-41, 53-55],  $GaSb_{1-y}As_y$  [56-60],  $In_{1-x}Ga_xP$  [61], and  $In_{1-x}Ga_xAs$  [55-57, 60-64], only limited information exists on the extension of the MBE technique to the quaternary forms of III-V alloys such as  $In_{1-x}Ga_xAs_yP_{1-y}$  [58,65]. Consequently, the actual mechanisms which govern the MBE growth of quaternary materials are not well understood at the present time.

There is, in general, a complex relationship between the substrate temperature and the intensities of the incident molecular beams. Beams of Ga and In have a finite lifetime on substrates heated to the 300 to 600 °C temperatures required to achieve a high degree of crystalline perfection in the homoepitaxial growth of the binaries GaAs and InP [1,34,66]. Congruent processes dominate under Langmuir (free) evaporation conditions until a temperature of approximately 657 °C is reached for the (001) surface of GaAs [67] and approximately 365 °C is attained for the (001) surface of InP [68]. At still higher temperatures, there is an additional surface population of the group III element created by the disproportionate desorption of the group V element. The desorbing  $As_2$  and  $P_2$  can be replaced by incident beams of As and P, respectively. The high vapor pressure, group V elements have a very short lifetime on the heated substrate unless there is a surface coverage of the group III elements. The latter condition yields a dramatic increase in the sticking coefficient of the group V elements. Stoichiometry is therefore ensured by the presence of an excess flux of the group V elements. Growth rates and alloy compositions of ternary

alloys containing two group III elements are primarily controlled by adjusting the arrival rates of the group III elements [56,61]. It is significant that the growth of alloys containing two group V elements requires ratios of the incident group V fluxes that differ from the composition of these elements in the resulting epilayer [39,53,57,65]. Since As appears to react preferentially with group V sites that are available to incident molecules of As and P, the control of composition  $y$  for  $\text{In}_{1-x}\text{Ga}_x\text{As}_y\text{P}_{1-y}$  layers grown by MBE involves establishing a relationship between substrate temperature and the excess P flux required to limit the relative supply of As molecules. Simple, noncompeting processes operate for the group III elements, and the composition  $x$  is a direct function of the intensities of the In and Ga molecular beams.

A secondary thrust of this research program exploits the characteristics of MBE for shadow masking and precise doping control which have the potential for extending the present planar technology and for enhancing the performance of specific microwave and millimeter wave GaAs devices. Experimental studies have recently demonstrated that the isolation of active GaAs devices can be achieved by shadow masking and by polycrystalline growth techniques. Patterned metal or silicon masks placed between the source ovens and the substrates lead to selective growth with lateral dimensions on the order of a few  $\mu\text{m}$  [69,70]. Tapers in thickness, doping, and composition can be directly written into the epilayer by translating the mask with respect to the substrate during growth [71]. Self masked growth of  $[\bar{1}\bar{1}0]$  stripes a few  $\mu\text{m}$  wide can be formed at the bottom of undercut channels that have been preferentially etched in (001) oriented substrates [72,73]. High resistivity GaAs forms on regions of a substrate coated with a dielectric

film ( $\text{SiO}_2$ ) during the deposition of epitaxial GaAs in regions previously inlaid in the dielectric by standard photolithographic processes [74]. Planar GaAs mixer diodes fabricated by this technique showed conversion losses at 51.5 and 103.0 GHz that were approximately 2 dB lower than the figures measured for identical conventional devices.

Since MBE provides very tight control of layer thickness and both p- and n-type doping profiles in GaAs, it represents an excellent technique to use in experimental investigations of the performance of microwave devices which depend sensitively upon the accurate definition and reproduction of doping profiles. Of particular interest are devices where doping concentrations change by orders of magnitude over distances that are only a fraction of a micron thick. Examples of devices fabricated with MBE GaAs layers include Schottky barrier and p-n junction varactors with hyperabrupt doping profiles [75,76], low-high-low IMPATTs delivering 2.8 w at 11.7 GHz with an efficiency of 18 percent [77], millimeter wave mixer diodes that are characterized by state of the art noise figures and conversion losses [74,78-80] including Mott barrier diodes with an average noise temperature of 47 °K, low noise FETs [81-84] featuring a minimum noise figure of 1.5 dB with associated gains of 15 dB at 8.0 GHz, and power FETs [83,85,86] producing a 4.0 GHz power output of 4.9 W at 3 dB gain and an 8.0 GHz power output of 1.1 W at 1.0 dB gain compression with a 7.5 dB power gain.

## 1.2 PROGRAM GOALS

The objective of this research is to investigate the growth of  $\text{In}_{1-x}\text{Ga}_x\text{As}_y\text{P}_{1-y}$  and GaAs using molecular beam epitaxy and to characterize the resulting structural, electrical, and optical properties of thin layers of

these semiconductors which impact upon their application to microwave, millimeter wave, and optical devices. The deposition parameters for forming heteroepitaxial layers of  $\text{In}_{1-x}\text{Ga}_x\text{As}_y\text{P}_{1-y}$  will be defined in an MBE system that is specifically designed for growing III-V alloy semiconductors. Layer properties which are an inherent feature of the MBE growth process will be identified by a comprehensive materials analysis program. Layers will be grown with targeted values of thickness, n- and p-type doping profiles, and compositions x and y that are selected to demonstrate the potential of MBE for achieving the high quality required in such quaternary device structures as FETs, TE0s, and double heterostructure lasers formed on InP substrates. Unique masking capabilities of MBE that show promise for developing planar technologies will also be investigated. Additional studies in GaAs will concentrate on using the doping control in MBE to provide an experimental basis for exploring the limits of performance of microwave and millimeter wave devices which require finely resolved doping profiles (e.g., mixer diodes, IMPATTs, and FETs). Quaternary and GaAs MBE layers with specific profiles for materials analysis and device fabrication will be prepared and delivered to the Navy for evaluation by NRL and other appropriate laboratories.

### 1.3 PRINCIPAL RESULTS

During the first year of the research program, the following results were obtained:

- The fast pumping speed of a single cryopump can be used advantageously to evacuate both the interlock and growth chambers in an MBE system developed for growing alloy semiconductors (pp. 11 - 18). The GaAs layers grown in this system before the introduction of P were unintentionally doped with a shallow

acceptor at levels of  $1.0$  to  $6.0 \times 10^{15} \text{ cm}^{-3}$  (pp. 27 - 30).

- Monitors such as ionization gauges and quadrupoles which sample direct molecular beam intensities are useful in estimating impingement rates (pp. 18 - 24) and in characterizing undesirable flux transients during the shuttering of MBE ovens operating under thermocouple control (pp. 24 - 26).
- Inverted profile, peeled film mixers (pp. 31 - 32) and millimeter wave IMPATT structures (pp. 32 - 36) have been prepared with MBE GaAs.
- Characteristics of iron as a new MBE dopant are established. Although iron is incorporated on Ga sites (pp. 54 - 55) which should lead to high resistivity material, a shallow compensated donor is dominant in layers grown at  $540 \text{ }^\circ\text{C}$  (pp. 54 - 60). Iron-doped layers grown at  $460 \text{ }^\circ\text{C}$  are semi-insulating (pp. 60 - 63) and incapable of supporting excitation emission at  $1.514 \text{ eV}$  at  $4.2 \text{ }^\circ\text{K}$  (pp. 52 - 53). Both Auger (pp. 44 - 47) and SIMS (pp. 47 - 52) depth profiles indicate a strong segregation of iron. This feature limits the usefulness of iron for conventional MBE application in FET buffer layers.
- Layers of  $\text{In}_x\text{Ga}_{1-x}\text{As}$  grown on passivated InP substrates (pp. 65 - 71) show a sharp decrease in carrier mobilities for undoped epilayers with lattice constants smaller than the substrates ( $x < 0.53$ ) (pp. 72,76).
- Significant changes in morphology and free In are observed at the surface of  $\text{In}_x\text{Ga}_{1-x}\text{As}$  layers deposited on GaAs substrates held at  $510 \text{ }^\circ\text{C}$  when the composition  $x \geq 0.3$  and the Ga flux is maintained at a constant rate equivalent to a GaAs growth rate of  $0.64 \text{ } \mu\text{m hr}^{-1}$  (pp. 77 - 81).
- Epitaxial layers of  $\text{In}_{1-x}\text{Ga}_x\text{As}_y\text{P}_{1-y}$  have been grown using ovens loaded with Ga, In, As, and GaP (pp. 87 - 95). Apparently, this is the first reported growth of this quaternary on GaAs substrates using molecular beam epitaxy. The broad peaks detected in rocking curves of X-rays diffracted by thin quaternary layers

( $\leq 2.0 \mu\text{m}$  thick) are tentatively attributed to compositional inhomogenities (pp. 92,93).

- The limited diffusion of As typically leads to group III-stabilized growth with a rough surface texture in shadow masked regions during the deposition of GaAs and  $\text{In}_x\text{Ga}_{1-x}\text{As}$  layers. This feature is missing in the  $\text{In}_{1-x}\text{Ga}_x\text{As}_y\text{P}_{1-y}$  layers where both As and P beams are present (pp. 95 - 100).

## 2.0 DESIGN AND OPERATION OF MBE SYSTEMS

Section 2.1 describes an extremely versatile and reliable MBE system that is explicitly designed for conducting research on III-V quaternary semiconductors. Careful calibration of the molecular flux intensities expedites the initial setup of MBE systems. The basic procedure for relating flux intensity to the convenient experimental variable, oven temperature, is reviewed in Section 2.2.1. Experimental results, however, in Section 2.2.2 emphasize the unintentional transients in emission that can occur for an abruptly shuttered oven that is drawing power in proportion to the output from a thermocouple attached to the rear of the oven. The growth of unintentionally doped GaAs in the cryopumped MBE system is detailed in Section 2.2.3

### 2.1 CONFIGURATION OF QUATERNARY MBE SYSTEM

Novel design features of the quaternary MBE system include cryopumping of the growth and interlock chambers, extensive use of cryoshrouds in the growth region, direct monitoring of the molecular beams from six source ovens, and visual evaluation of the optical smoothness of the growing epilayer.

A schematic drawing of the system components is shown in Figure 2. The cryopump provides a base system pressure of mid  $10^{-9}$  Torr and circumvents the special handling procedures that are typically required to prolong the life of ion pumps exposed to P ambients [87]. The interlock allows substrates to be loaded without exposing the growth chamber and sources to atmospheric pressures of the laboratory ambient. This maximizes the cleanliness of the growth chamber. Valves in the foreline provide rough pumping of the cryopump, growth chamber, or interlock chamber. During growth and

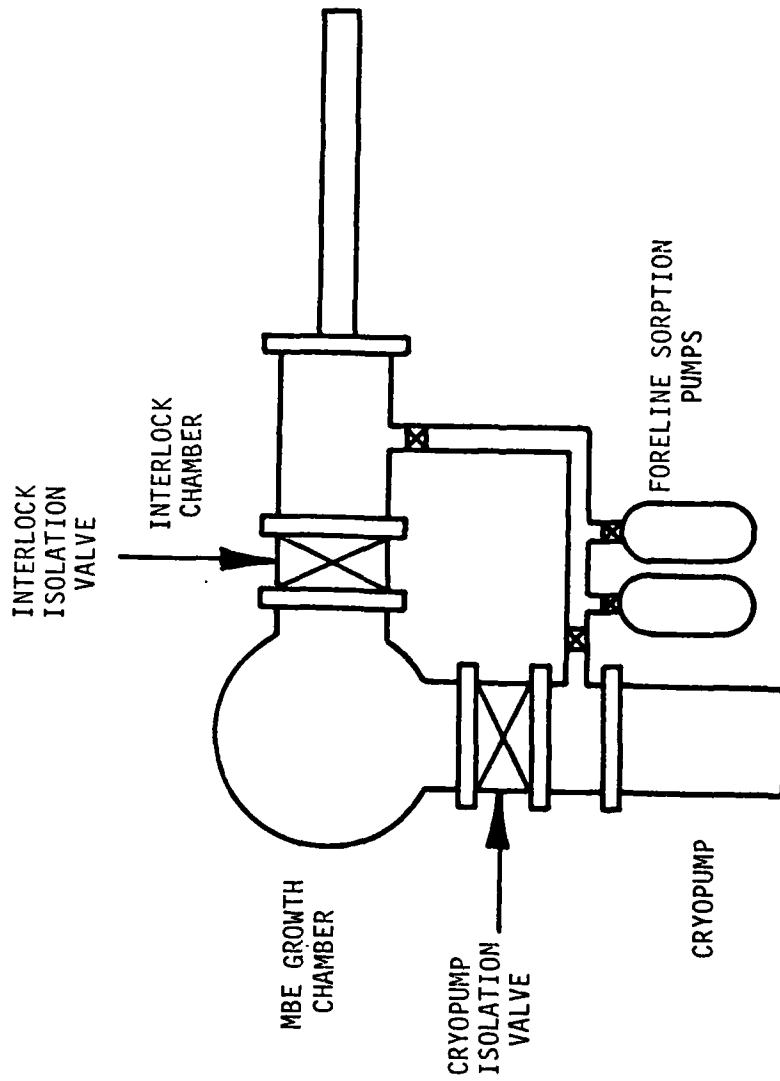


Figure 2. Details of Cryopump Connections for Evacuating the Growth and Interlock Chambers.

system bakeout, the gate valves are open and condensable materials will be deposited in the cryopump. These materials (including As and P) can then be transferred into the roughing sorption pump by closing the gate valve and baking out the cryopump. The main chamber and sources can be maintained under UHV ambient while the cryopump is regenerated and each regeneration will eliminate undesirable materials from the system. Operation can be continued in this manner until source loads have to be replenished or internal system modification are incorporated. There is an auxiliary vacuum line for evacuating the interlock chamber with the cryopump following sample retrieval and loading of a fresh substrate. Consequently, the pressure in the growth chamber never rises above the  $10^{-7}$  Torr range when the main gate valve between the interlock and growth chambers is opened.

Figure 3 is a picture of the quaternary MBE system. The growth chamber is closed and under vacuum but the interlock chamber is open with the sample insertion flange removed for loading. The panel under the table holds the ion gauge control and controls for system bakeout. The rack on top of the table holds power supplies and temperature controllers for the substrate heater and source ovens. Water connections for the source holder and thermocouple and power connections for four source ovens are shown.

The heavy source flange is over 14 inches in diameter, however, it is easily handled because it is mounted on a ball bearing drawer slide carrier. The carrier is counter weighted; and, once the bolts are removed, the source flange will slide out of the chamber to any partially open position. Figure 4 shows the source flange in the fully open position. The flange rotation capability facilitates loading source materials or making mechanical adjustments. The end of the  $\text{LN}_2$  trap that surrounds the growth region can be seen

1. GROWTH CHAMBER
2. OVEN FLANGE
3. INTERLOCK CHAMBER
4. CRYOPUMP
5. LN<sub>2</sub> ROUGHING PUMPS

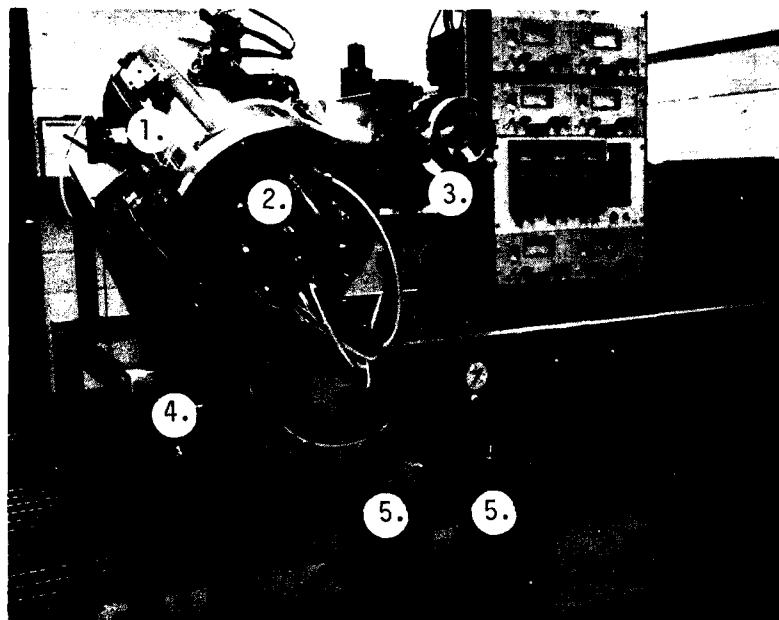


Figure 3. Quaternary MBE System

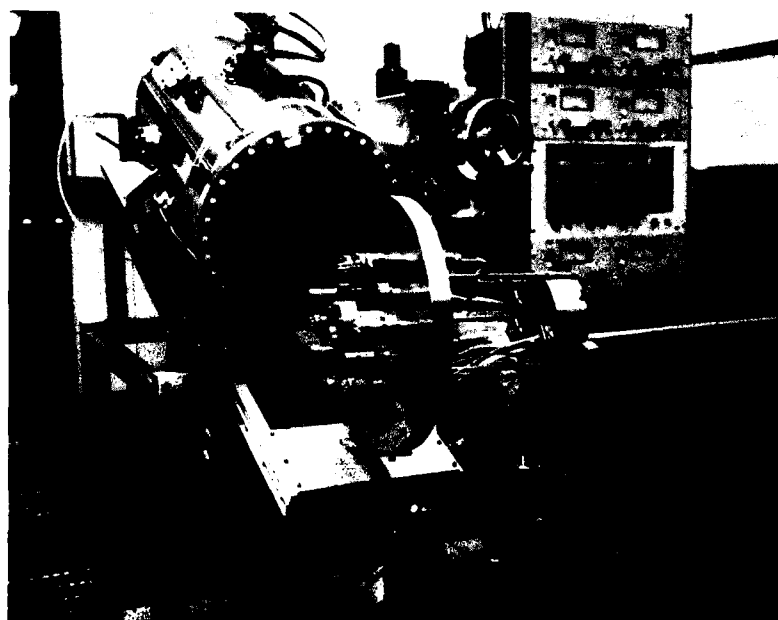


Figure 4. Source Flange Open and Rotated for Loading or Adjustments

inside the chamber. The substrate is inserted inside this trap during growth by means of the interlock insertion mechanism.

Figure 5 is a cross-sectional drawing that shows the placement of the major components in the growth chamber. The six sources have rotational symmetry about the central axis of the chamber passing through the viewport. All the sources point at a common point in the center of the substrate as indicated by the dotted lines. Regions partly or completely obscured from the sources by the presence of the substrate and heater are indicated by shaded areas. The interior, unshaded area represents the cone shaped volume behind the substrate that has direct exposure to all sources. The quadrupole mass spectrometer and ion gauge are mounted in the region of direct exposure to make these instruments available for direct flux measurements. A  $\text{LN}_2$  cryopanel surrounds the growth region to isolate it from the rest of the system and confine the effusing materials to as small a volume as possible. Surrounding this volume with a cryogenic panel provides isolation from materials that may be desorbed from the system walls during growth. The cryopanel cannot be made tight enough to prevent passage of undesirable materials but has been constructed to minimize such penetration. In this way, it may be assumed that contamination sources most likely originate from within the growth region and the search for unintentional sources of contamination narrows considerably.

Figure 6 shows the source holder containing six source positions surrounding the central viewport or laser observation port. Good MBE material is very smooth and visual observations of the growing layer allow an early abortion of poor runs. This minimizes the effort wasted on useless material. It may also be desirable to use a laser to observe the smoothness of

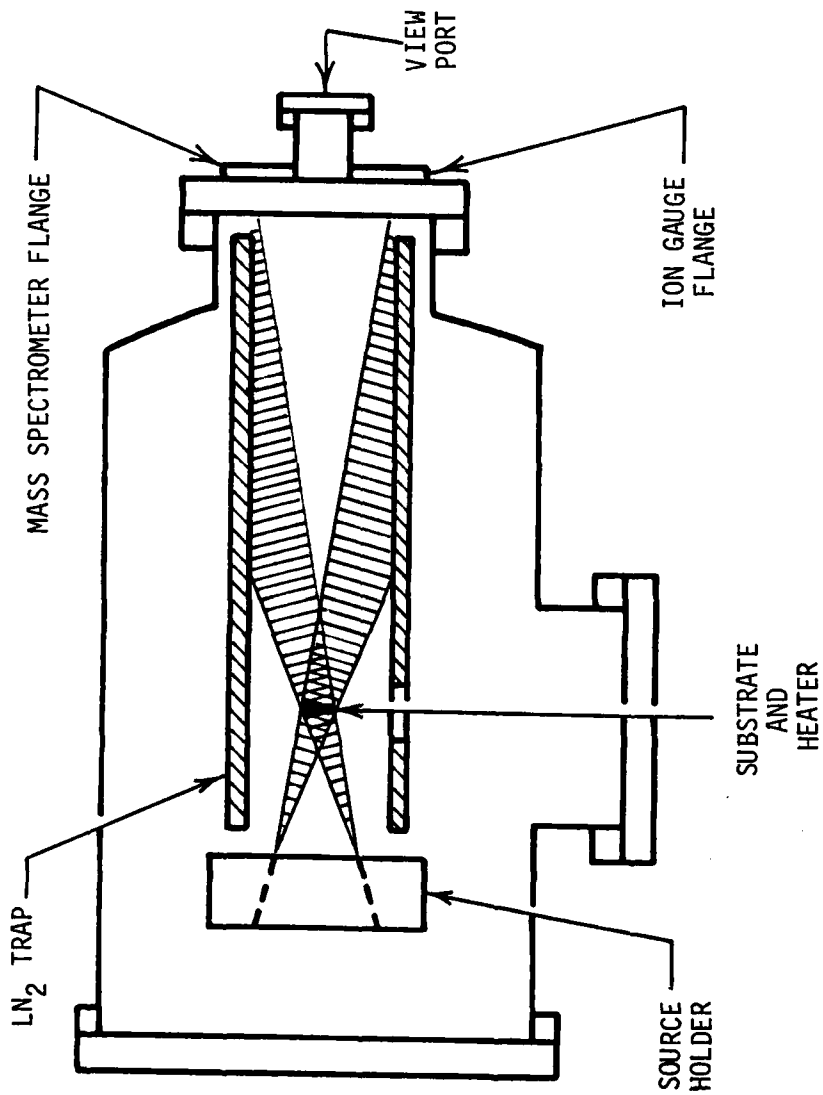


Figure 5. Major Components of the Growth Chamber of the Quaternary MBE System

the epilayer. Minute changes in surface smoothness such as the cross hatching which arise from lattice mismatch can be detected by observing the dispersion of a laser beam specularly reflected from the sample surfaces [35]. These noncontaminating optical techniques are particularly desirable for in situ monitors in the growth chamber. The six tubes that hold the sources have the same diameter as the central observation tube. The active apertures for the sources are defined by the holes punched in the Ta ring that covers the source tubes. This ring shields the substrate from direct exposure to materials other than the oven loads that may be effusing from the source compartments.



Figure 6. Source Holder for Quaternary MBE System

Composite graphite/lucalox ovens in different stages of assembly are shown in Figure 7. The top oven is complete and ready to install in the source flange. The bottom oven has the Ta winding and power lead installed but no thermocouple or Ta foil heat shield. Before the source loads are introduced, the ovens are baked at 1200 °C for 30 minutes in a separate UHV vacuum system and then installed in the MBE system.

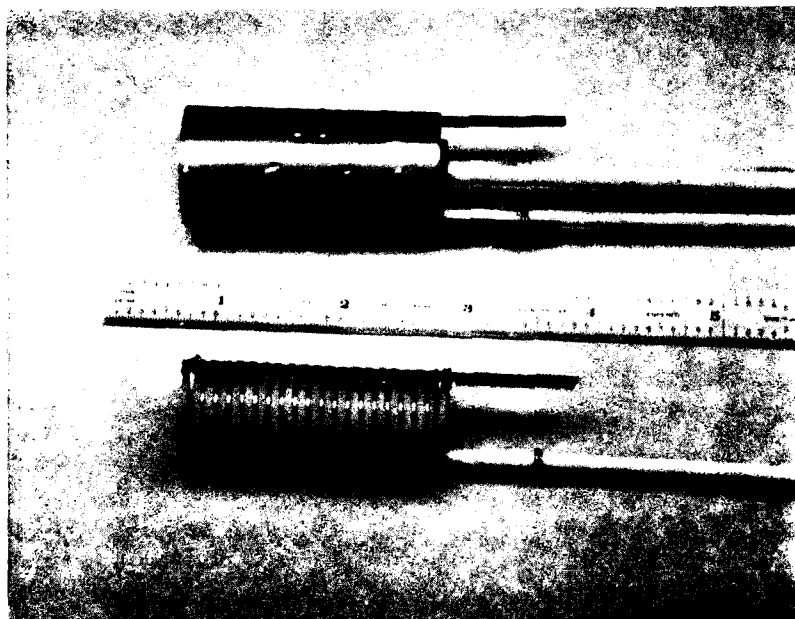


Figure 7. Source Oven Assembly

## 2.2 OPERATING TECHNIQUES

### 2.2.1 Molecular Flux Measurements

The molecular fluxes effusing from the source ovens can be measured using an ion gauge positioned to intercept the direct flux components which are incident upon the substrate during epitaxial growth. The

basic technique is described in the following discussion and representative data are presented for a gauge located 9.0 cm from the oven apertures.

The relationship between the gas ion current  $I_j$  flowing in an ionization gauge and the gas pressure  $p$  is written [88]

$$I_j = I_e \ell \sigma p \quad (3)$$

where  $I_e$  = constant electron emission current,  
 $\ell$  = electron path length, and  
 $\sigma$  = gas ionization probability.

The ionization probability depends specifically upon the electron energy (typically set to approximately 150 eV) and the type of gas. While equivalent ionization probabilities of the common residual gases such as  $H_2(2.0)$ ,  $O_2(1.22)$ ,  $H_2O(1.11)$ ,  $CO(.93)$ ,  $CO_2(.73)$ , and  $Ar(.85)$  have been established with respect to  $N_2(1.0)$ , equivalent values of  $\sigma$  for the metallic beams effusing from MBE ovens are not generally available.

The impingement rate  $F(\text{cm}^{-2} \text{sec}^{-1})$  of the number of gas molecules striking a surface is conveniently written as [89]

$$F = 3.513 \cdot 10^{22} \frac{p}{(MT)^{1/2}} \quad (4)$$

where  $p$  = pressure (Torr),  
 $M$  = molar mass, and  
 $T$  = temperature ( $^{\circ}K$ ).

The impingement rate can also be expressed in terms of the oven geometry and equilibrium pressure  $p^*$

$$F = 3.513 \cdot 10^{22} \frac{a p^*}{\pi h^2 (MT)^{1/2}} \quad (5)$$

where  $a$  = area of oven aperture and  
 $h$  = source to receiver spacing.

The equilibrium pressure is a function of the source temperature:

$$\log p^* = B - AT^{-1} + \dots \quad (6)$$

where  $A, B$  = empirical constants derived from tabulated vapor pressure data for each element.

Experimental values of the impingement rates from the As, In, Ga, and Fe ovens were determined using Equation 4 and the measured beam pressures and oven temperatures. Beam pressures were read on a modified CVC Model G1C-001 ionization gauge driven by a VEECO RG-3A control unit. The gauge was calibrated against a Varian UHV-24 nude ion gauge and a Varian 971-0003 control unit. Since the As oven operates at temperatures below 400 °C, an estimate of the As temperature was formed by monitoring the output of a chromel/alumel thermocouple embedded in the oven. A Leeds and Northrup No. 8622 optical pyrometer gave a direct measure of the Ga and Fe temperatures. The experimental data are plotted in Figure 8. For comparison, theoretical curves of  $F(T)$  are also drawn in Figure 8 using Equation 5, tabulated vapor pressure data [89], and the given oven/gauge geometrical

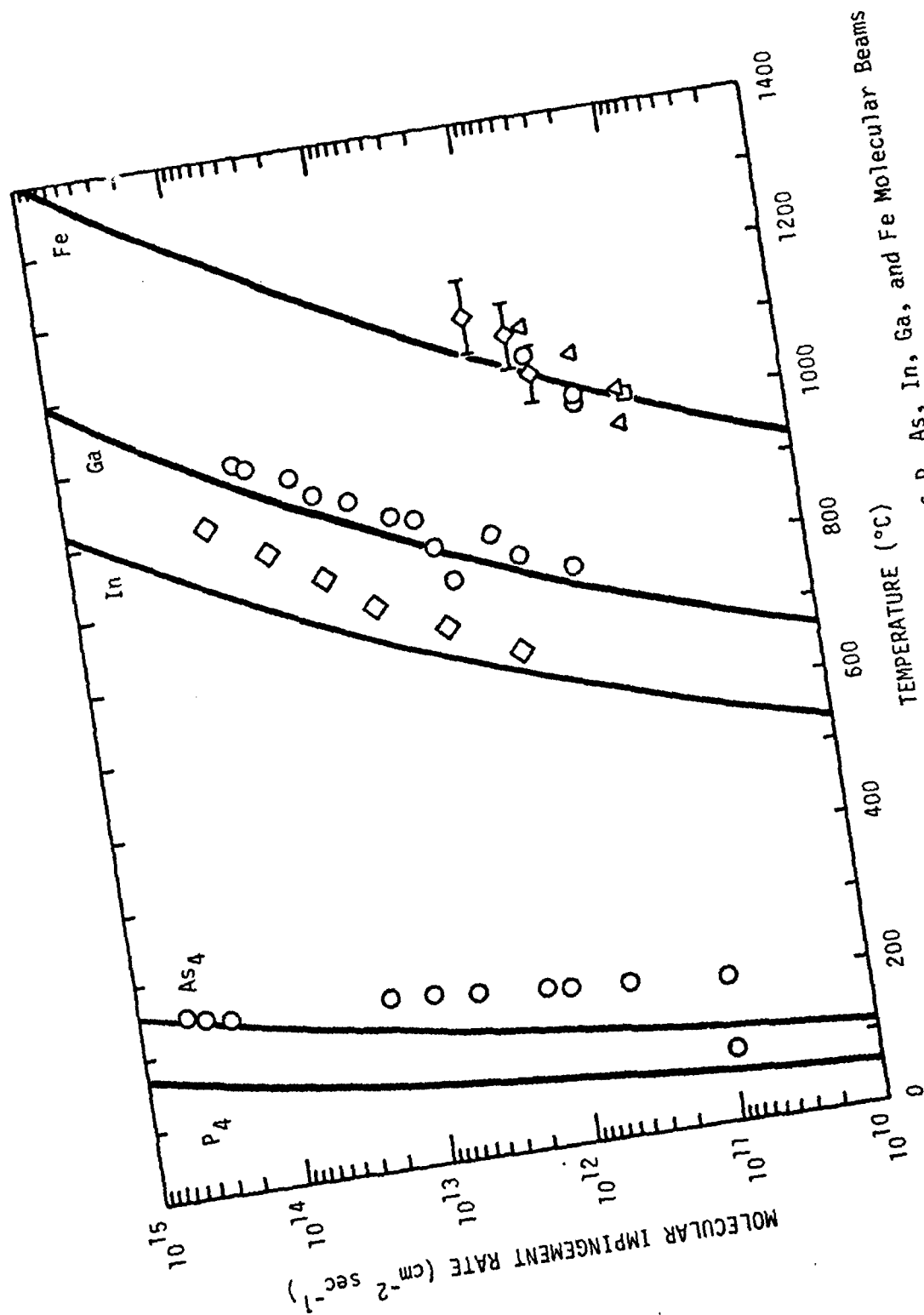


Figure 8. Impingement Rates for the Direct Components of P, As, In, Ga, and Fe Molecular Beams Incident Upon an Ion Gauge Located 9.0 cm from the Oven Apertures.

configuration. In general, the agreement between the theoretical and experimental results is satisfactory. The four symbols representing Fe data points identify data taken on four separate occasions. The error bars shown on one data set indicate the range of temperatures observed at different regions of the 1.0 mm diameter Fe wire load coiled inside the oven. It is not practical to operate the Fe oven at the temperatures ( $> 1200$  °C) which would yield the greatest discrimination in separating the direct beam and residual gas components. There is nevertheless evidence that iron beams of  $10^{12}$  cm $^{-2}$  sec $^{-1}$  are available at oven temperatures of 1100 °C. This is equivalent to a doping level of approximately  $10^{20}$  cm $^{-3}$  at the substrate position under conditions of unity sticking coefficient and a GaAs growth rate of 1.0  $\mu$ m hr $^{-1}$ . Gallium, indium, and arsenic impingement rates were monitored by the ion gauge over the range from  $10^{11}$  to  $10^{14}$  cm $^{-2}$  sec $^{-1}$ . Since consistent offsets are observed in the In and Ga data, the experimental results suggest that

$$\frac{\sigma_{\text{In}}}{\sigma_{\text{N}_2}} \sim \frac{\sigma_{\text{Ga}}}{\sigma_{\text{N}_2}} < 1.0. \quad (7)$$

There is limited evidence in the As results that the time required to reach a stable equilibrium condition exceeded the sampling time between incremental step increases in the oven power at the lower temperatures.

Figure 8 highlights the difficulty in maintaining constant flux levels by keying on temperature to control the emission of an oven loaded with a high vapor pressure, group V element such as arsenic and phosphorous. An error analysis of Equation 5 reveals that incremental changes of pressure  $\Delta p^*$  and temperature  $\Delta T$  lead to different changes in the beam impingement

rate. The following inequality is satisfied under normal operating conditions for the As oven:

$$10 < B - \log p^* = \frac{A}{T} < 20 \quad . \quad (8)$$

Therefore, the relative incremental change  $\Delta F/F$  for the As oven is approximately given as  $\Delta F/F = 0(10^{-3})$  for pressure control and  $\Delta F/F = 0(5 \times 10^{-2})$  for temperature control where  $\Delta p^*/p^* = \Delta T/T = 10^{-3}$ . In the present investigations, elemental As is employed for the As source, and the As flux is controlled to within approximately  $\pm 10$  percent using a chromel/alumel thermocouple to sense oven temperature. Tighter temperature/flux control is generally achieved at the higher oven temperatures in the 600 to 1000 °C range. Polycrystalline GaP is employed for the P source (operating temperature: 800 to 900 °C). As section 6.3 indicates (p. 95), the Ga emission from this source is not entirely negligible.

An ion gauge located near the substrate position can directly monitor beam impingement rates of  $10^{14}$  to  $10^{15} \text{ cm}^{-2} \text{ sec}^{-1}$  which correspond to GaAs growth rates of approximately  $1.0 \text{ } \mu\text{m hr}^{-1}$ . Preliminary results for MBE  $\text{In}_x\text{Ga}_{1-x}\text{As}$  (Section 5.1.3, p. 71) indicate that monitoring the ion gauge pressures of In and Ga beams constitutes a convenient method for presetting the composition  $x$ . Additional background discrimination techniques such as modulation of the beam samples by the gauge would be needed to provide control of ovens adjusted for intentional doping at  $10^{16}$  to  $10^{18} \text{ cm}^{-3}$  levels. Beam data measured at higher levels is useful, however, since such data can be extrapolated to lower values for setting incident doping beam intensities. Quite apart from the potential contamination problem, actual gauge operation

inside the primary ovens such as As and Ga involves pressures of  $10^{-4}$  to  $10^{-1}$  Torr which is a range that is not readily covered by conventional ionization gauges.

### 2.2.2 Shuttering Molecular Beam Sources

In addition to monitoring the steady state impingement rates of molecular beam sources, quadrupole and ion gauge monitors have also been employed to investigate transients in flux levels associated with shuttering operations. The inset in Figure 9 gives the basic experimental arrangement for measuring the Ga<sub>69</sub> flux with a Granville Phillips Spectra Scan 750 quadrupole located 11.8 cm from the gallium oven. During these tests, oven control was derived from the W 5%Re/W 26%Re thermocouple, a Leeds and Northrup Electromax III controller, and a Hewlett-Packard HP-6286 A programmable power supply. The impingement rate at the quadrupole under steady state conditions was set at  $1.7 \times 10^{12}$  molecules  $\text{cm}^{-2} \text{sec}^{-1}$ .

Several interesting features are observed in the recorder trace of the quadrupole output presented in Figure 9. Although the longest observation period in this test is relatively brief when compared to a time span of several hours representative of MBE growth runs, the present data do suggest that the long term stability of the quadrupole will probably satisfy oven control loop requirements. The small oscillatory ringing is believed to be derived from hunting action in the controller. The most interesting features in Figure 9 are the sharp peaks in molecular flux when the oven shutter is opened. The transient decline in molecular beam intensity is linked to thermal cooling of the front emitting surface which has received heat that is reradiated by the closed shutter. The outer emitting surface cools to a new equilibrium temperature when the shutter is open. This is

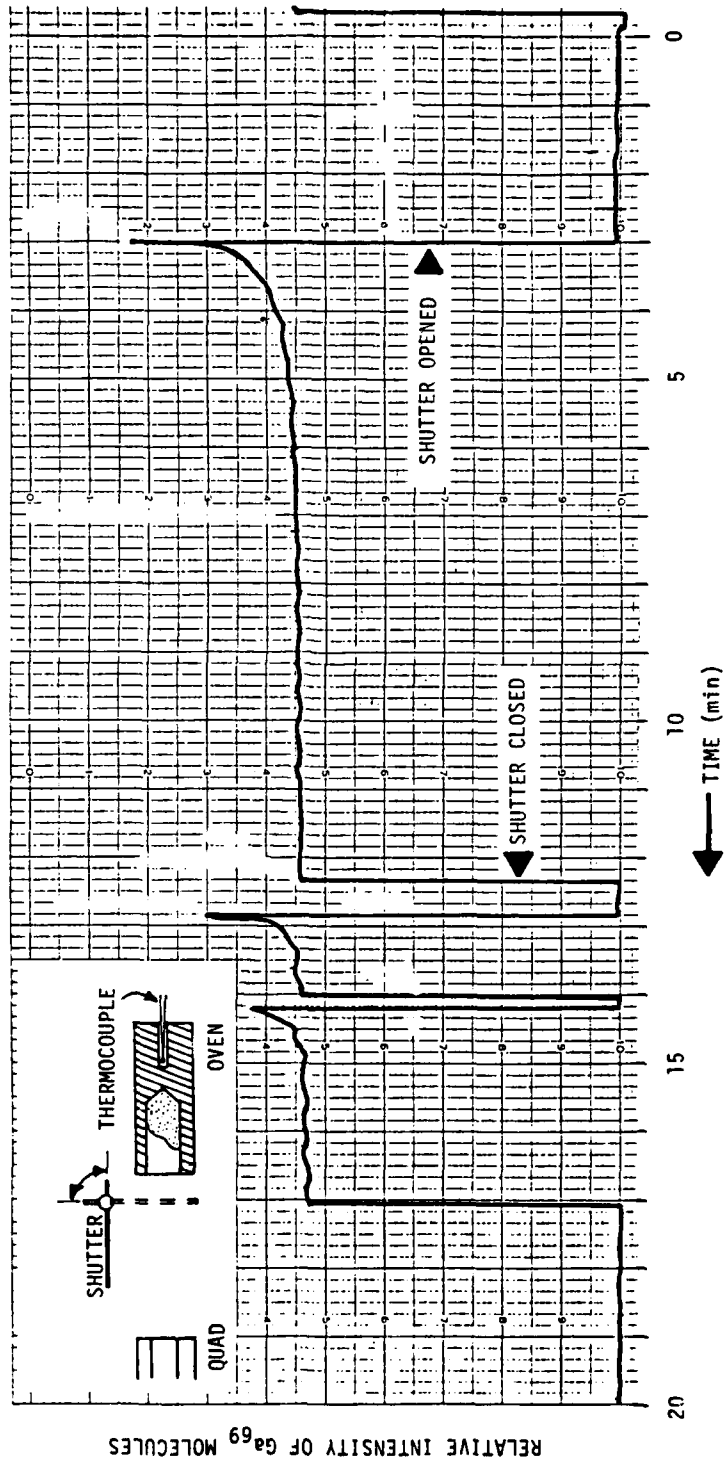


Figure 9. Transients in the Molecular Beam Intensity of a Shuttered MBE Oven Under Thermocouple Control.

accompanied by a change in flux level that cannot be entirely accommodated by a sensing thermocouple embedded in the rear of the oven. As Figure 9 clearly indicates, the magnitude of the transient peak depends upon the length of time that the shutter remains closed. A drop in the Fe oven load temperature when the shutter was opened could be visually observed with an optical pyrometer. The load in this oven was not thermally coupled as tightly to the oven walls as the Ga, Ge, and Sn oven loads.

Molecular beam transients such as those shown in Figure 9 are basically undesirable because:

- the initial growth rate is rapidly decreasing at the interface and this impacts on the crystalline structure of the MBE epilayers,
- doping profiles at the substrate/epilayer interface will be a complex function of a transient dopant flux (higher doping) and a faster growth rate (lower doping), and
- the interfacial composition of alloy semiconductors will be graded over an extended region at typical MBE growth rates of  $1.0 \mu\text{m hr}^{-1}$ .

A technique for reducing the effusing flux overshoot in the present MBE GaAs system consists of holding oven temperatures below the desired set point while oven shutters are closed. Immediately after a shutter is opened, the controller for that oven is reset to the target temperature and molecular impingement rate. Careful optimization of the rate and approach controls in this mode of operation effectively eliminates the transient overshoot. Another possible approach which is being investigated involves the direct control of the emitted flux level with a quadrupole positioned to always sample a fraction of the oven emission.

### 2.2.3 Unintentionally Doped GaAs

The background doping level of the cryopumped MBE system was established by growing a series of six unintentionally doped GaAs layers on (001) Cr-doped GaAs substrates. The ovens were loaded with 6N Ga (Alusuisse) and 6N As (Preussag). Base system pressures immediately prior to growth fell in the range of  $6 \times 10^{-9}$  to  $2 \times 10^{-8}$  Torr. Deposition rates of 0.3 to  $0.9 \mu\text{m hr}^{-1}$  and substrate temperatures of 580 °C were employed in these depositions. The first GaAs layer grown in the quaternary system contained a residual donor concentration of  $1 \times 10^{16} \text{ cm}^{-3}$ . High resistivities greater than 30 ohm-cm and close compensation were found in the following two layers, C0926-II and C1001-II. After these runs, the system parameters appeared to stabilize and the dominant background dopant was a residual acceptor at concentrations of 1.0 to  $6.0 \times 10^{15} \text{ cm}^{-3}$ . The major deposition conditions and electrical properties of the unintentionally doped GaAs layers are listed in Table 1.

Measurements of the Hall coefficients in the temperature range between 77 and 296 °K for layers C1011-II and C1012-II were interpreted in terms of a model based on a single acceptor level. This emphasized the shallow activation energy of the acceptor (0.009 to 0.012 eV). Higher binding energies have been established for the common acceptor dopants in GaAs such as C (0.026 eV), Be (0.0284 eV), and Zn (0.0307 eV) [90].

Figure 10 gives the temperature dependences of the Hall mobilities measured for three p-type layers which show the least compensation. Also plotted in Figure 10 is the mathematical expression

$$\mu = 400 (300/T)^{2.3} \quad (9)$$

Table 1. Deposition Parameters and Electrical Properties (296 °K) of Unintentionally Doped GaAs Layers Grown on Cr-Doped (001) GaAs in the Quaternary MBE system

MBE Layer	Thickness ( $\mu\text{m}$ )	Growth Rate ( $\mu\text{m hr}^{-1}$ )	$T_{\text{substrate}}$ ( $^{\circ}\text{C}$ )	Carrier Type	Concentration ( $\text{cm}^{-3}$ )	Mobility ( $\text{cm}^2\text{V}^{-1}\text{sec}^{-1}$ )	Activation Energy (eV)
C0925-II	0.6	0.3	580	n	$1 \times 10^{16}$	4268	*
C0926-II	0.3	0.7	580	p	$9 \times 10^{14}$	198	*
C1001-II <sup>†</sup>	0.4	0.6	580	*	*	*	*
C1011-II	1.7	0.9	580	p	$6 \times 10^{15}$	268	0.009
C1012-II	6.9	0.8	580	p	$1 \times 10^{15}$	266	0.012
C1017-II	4.2	0.7	580	p	$4 \times 10^{15}$	312	*

† Closely compensated, high resistivity layer

\* data not available

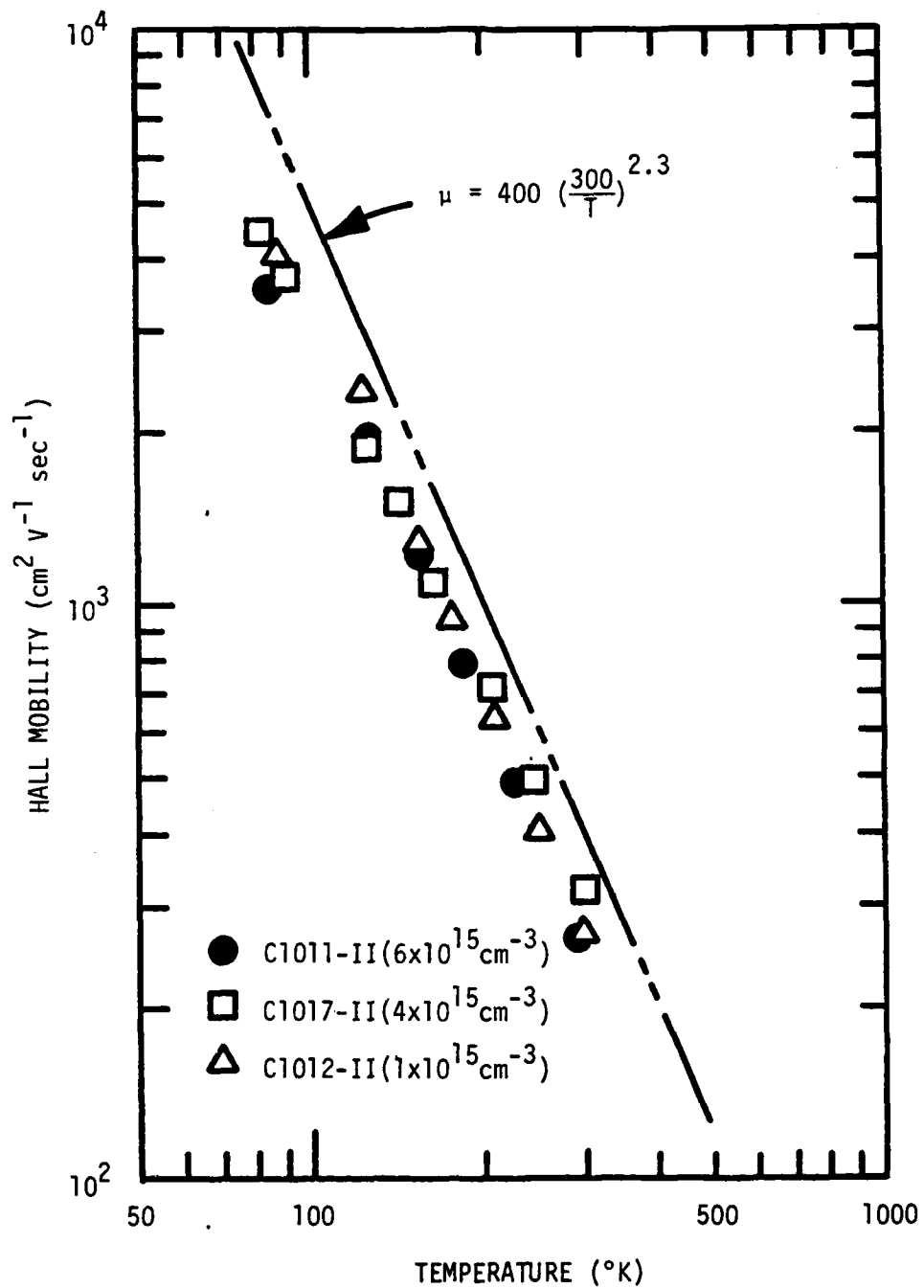


Figure 10. Hall Mobility vs Temperature for p-Type, Unintentionally Doped GaAs Layers Grown in the Quaternary MBE System

which reflects the behavior of high purity, p-type GaAs [91]. Compensation and ionized impurity scattering becomes increasingly important in decreasing the low temperature mobility for the three MBE layers.

### 3.0 MATERIALS FOR GaAs DEVICES

The study of GaAs grown by MBE has been extended to include inverted doping profiles for microwave mixers and spike profiles for millimeter wave IMPATTs. Details of the mixer diode material are presented in Section 3.1. The growth and characterization of GaAs IMPATT structures are discussed in Section 3.2.

#### 3.1 INVERTED PROFILE MIXER DIODES

One of the fundamental principals employed in designing low-noise, GaAs mixer diodes involves the selection of heavily doped substrates ( $\rho \leq 0.0005$  ohm cm) [92] in order to reduce the series resistance of the completed device to the lowest possible value [93]. This design feature can be pushed to the limit by eliminating the substrate and forming the back ohmic contact directly on the thin buffer layer adjacent to the lightly doped active layer.

Two MBE GaAs layers were grown on (100) Ge substrates to investigate the potential applications of a peeled film technology for fabricating GaAs mixer diodes. The doping profiles of the GaAs epilayers were the inverse of standard mixer profiles. The active region (0.5  $\mu\text{m}$  thick, doping approximately  $1 \times 10^{17} \text{ cm}^{-3}$ ) adjacent to the substrate was capped by a 3.4  $\mu\text{m}$  thick buffer region (doping approximately  $1 \times 10^{18} \text{ cm}^{-3}$ ). Both regions were doped n-type with Ge by growing under As-stabilized conditions. The Naval Research Laboratory has developed a sequence for processing the inverted profile mixers which includes attaching a conducting handle on the GaAs buffers, stripping away the Ge substrates by selective etching, and forming Schottky metallizations on the exposed active regions. Preliminary results indicate that improved noise figures are measured for

mixer diodes processed in this manner [94]. The basic peeled film approach may find further application in processing other devices such as millimeter wave IMPATTs or FETs [95].

### 3.2 LOW-HIGH-LOW mm IMPATT DIODES

Gallium arsenide layers with low-high-low doping profiles have been grown to assess the potential of MBE in fabricating millimeter wave IMPATT diodes. Workers at Bell Laboratories have prepared MBE GaAs IMPATTs which oscillated at a frequency of 11 GHz [77]. The diodes developed an output power of 2.8 W with 18 percent efficiency. While these X-band results are significant, the close control of layer thickness and doping afforded by MBE makes the process particularly attractive for preparing millimeter wave IMPATTs. Developing the control required in growing GaAs millimeter wave IMPATTs using chemical vapor deposition (CVD) techniques is a difficult technological problem. Some progress is being achieved in this area, and recent experimental results with CVD materials are providing the motivation for considering GaAs for millimeter wave IMPATTs. Powers as high as 710 mW with an efficiency of nine percent have been reported for 36 to 38 GHz GaAs IMPATTs [96], and peak pulse powers of approximately one mW have been obtained at 60 to 96 GHz for uniformly doped, GaAs IMPATTs [97].

High efficiency, high power IMPATT operation can be realized with a narrow, highly-doped spike that is positioned in the active region near the junction interface. The spike serves to confine the width of the avalanche zone. This minimizes the voltage drop  $V_a$  across the avalanche region and improves the diode efficiency  $\eta$ . In the simple model,  $\eta$  is proportional to the ratio  $V_d/(V_d + V_a)$  where  $V_d$  is the voltage drop across the drift region of the diode. The frequency of operation depends upon the

carrier transit time which is related to the depletion width at breakdown and the time required to initiate the avalanche. Control of the low-high-low doping profile becomes increasingly difficult at the millimeter wavelengths because the dimensions of the spike depth  $W_s$ , the width of the spike, and the width of the drift region  $W_d$  are defined on submicron scales. In previous MBE studies, tin was used to form high-low doping profiles for n-type GaAs layers designed for X-band IMPATT operation [98]. The interface between the high and low regions was poorly resolved because there is significant segregation of tin during the growth of GaAs by MBE [99-101]. Such segregation is intolerable for profiles requiring the precise positioning of abrupt interfaces with lateral extensions on the order of tens of monolayers. Therefore, Ge - a nonsegregating, n-type dopant - was selected to form the low-high-low profiles of the millimeter wave IMPATTs.

Doping profiles derived from C-V measurements for two IMPATT MBE layers are presented in Figure 11 and 12. The 1.0  $\mu\text{m}$  thick buffer layers and the 400 to 500  $\text{\AA}$  thick spikes were injected by mechanically shuttering the Ge molecular beam. Doping concentrations for these highly doped regions fell in the 1 to 4  $\times 10^{18} \text{ cm}^{-3}$  range. The layers were grown under As-stabilized conditions at growth rates of approximately one  $\mu\text{m hr}^{-1}$  and substrate temperatures of 560  $^\circ\text{C}$ .

Numerical studies of the optimum doping profiles for low-high-low IMPATT diodes in the 3 to 18 GHz range show that the depth of the spike should be approximately 0.15  $\mu\text{m}$ , the integrated charge  $Q_s$  of the spike should be approximately  $3.2 \times 10^{12} \text{ cm}^{-2}$ , and the  $N_d W_d$  product of the drift region doping level and width should be approximately  $2 \times 10^{12} \text{ cm}^{-2}$  [102]. It remains to be shown that these parameters also represent an optimum design for efficient IMPATT operation at higher frequencies where the time

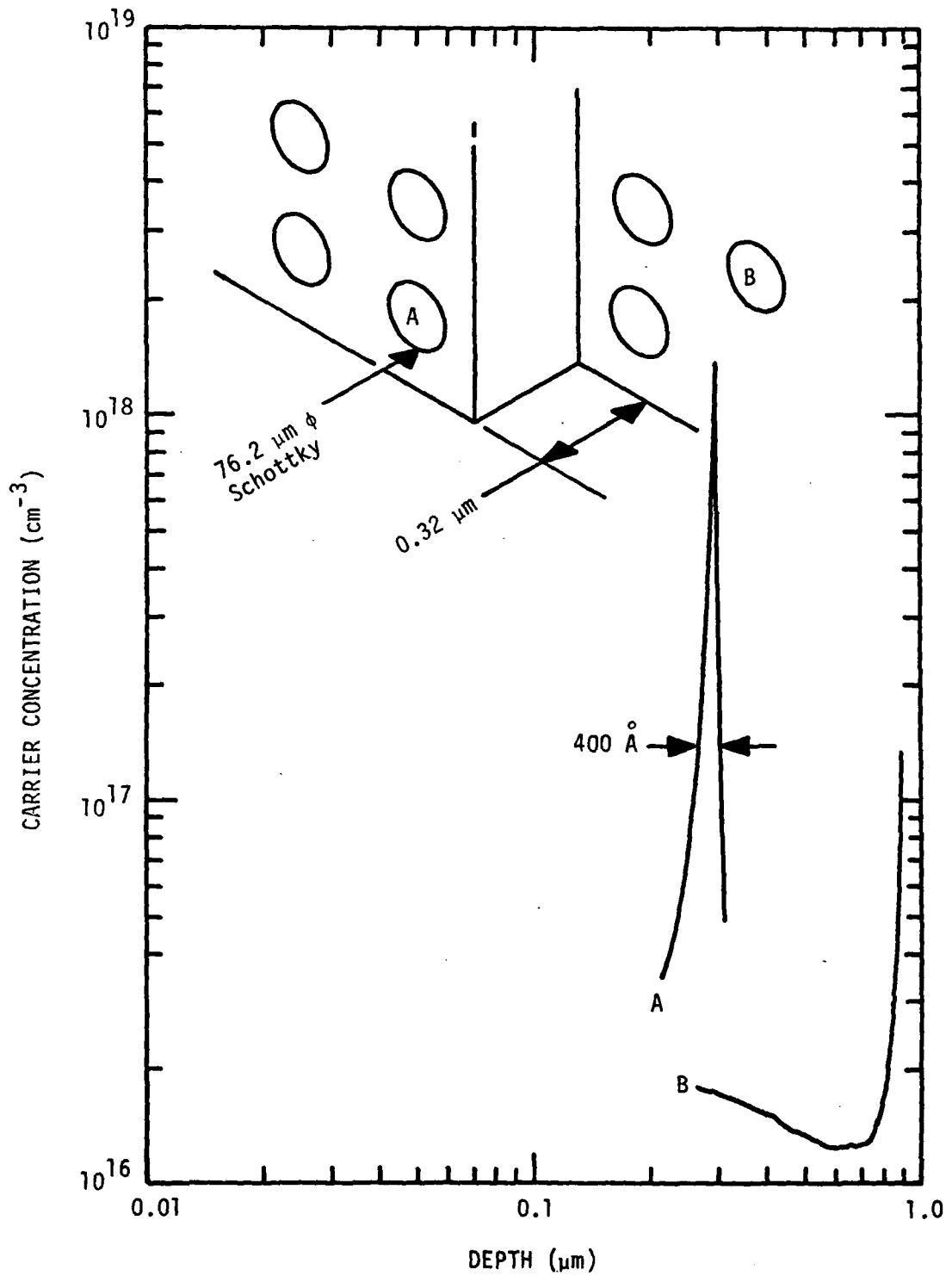


Figure 11. Low-High-Low Doping Profiles for MBE B0427 Showing Details of the Spike near the Surface (A) and the Interface 1.2  $\mu\text{m}$  Deep Between the Drift Region and the Buffer Layer (B).

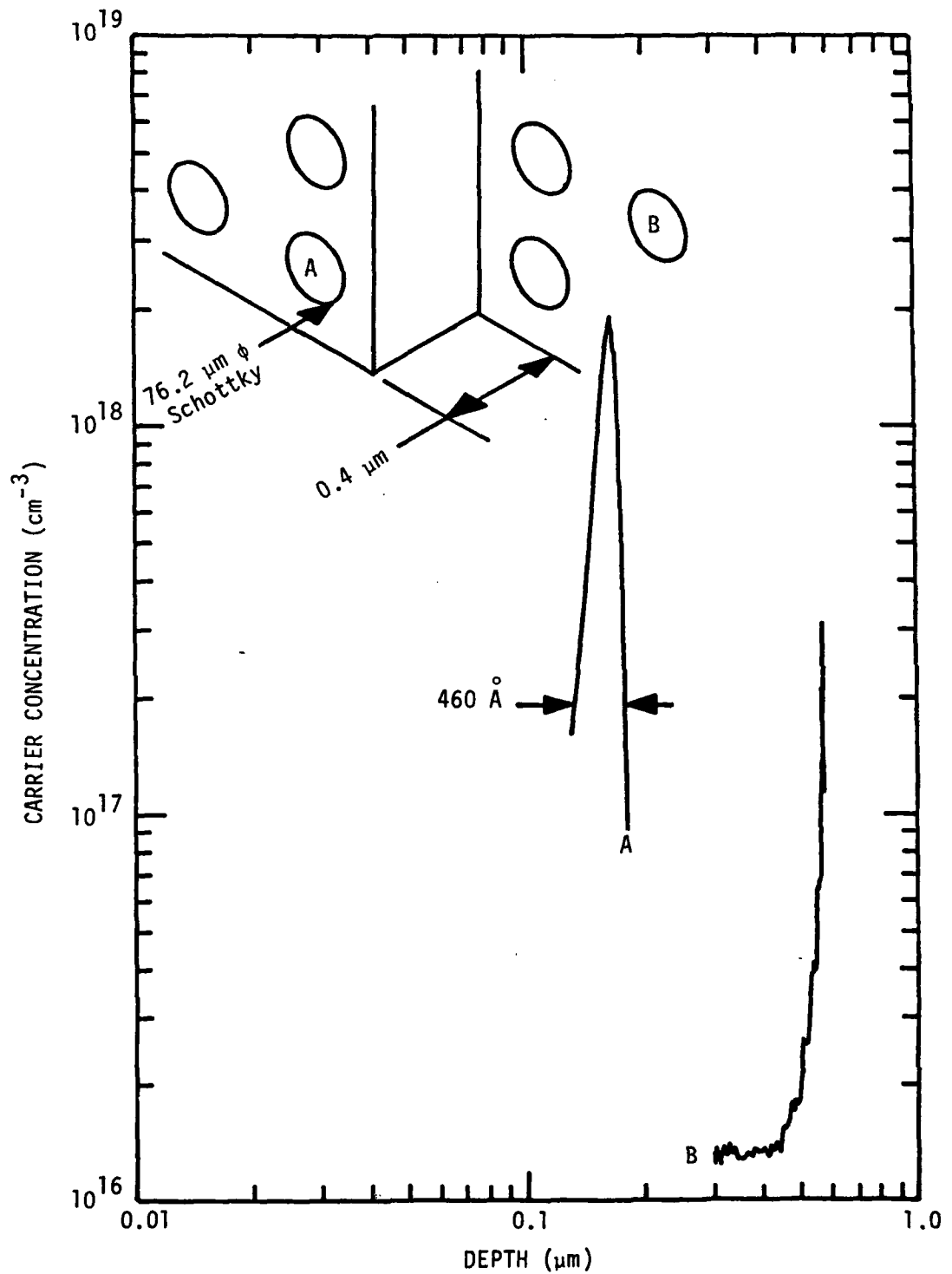


Figure 12. Low-High-Low Doping Profiles for MBE B0501 Showing Details of the Spike near the Surface (A) and the Interface 1.0  $\mu\text{m}$  Deep Between the Drift Region and the Buffer Layer (B).

required to form the avalanche becomes a significant fraction of the RF period. The parameters  $W_s$ ,  $Q_s$ , and  $N_d W_d$  have been determined from the doping profiles of B0427 and B0501. The results are summarized in Table 2. In line with the above discussion, these tabulated data and the doping profiles represent an encouraging characterization of the MBE layers. Junction temperatures for IMPATT diodes typically exceed 200 °C, and a reliable Schottky metallization, Pt/Ti/Au, and a suitable heat sink and package are being developed for evaluating the RF performance in the millimeter wave region.

TABLE 2. CHARACTERISTICS OF MBE IMPATT DIODES

Layer	$W_s$ ( $\mu\text{m}$ )	$Q_s$ ( $\text{cm}^{-2}$ )	$N_s W_d$ ( $\text{cm}^{-2}$ )
B0427	0.23	$2.4 \times 10^{12}$	$1.5 \times 10^{12}$
B0501	0.16	$4.4 \times 10^{12}$	$1.1 \times 10^{12}$

$W_s$  = depth of the spike below the junction

$Q_s$  = charge per unit area in the spike =  $\int N dx$

$N_d$  = doping concentration in the drift region

$W_d$  = width of the drift region

#### 4.0 IRON DOPING STUDIES

An alternative approach in growing GaAs microwave FETs by molecular beam epitaxy has been investigated which uses an iron-doped buffer layer sandwiched between the thin n-type, active layer and the semi-insulating GaAs substrate. Heretofore in MBE this buffer has usually been eliminated [82] or formed from unintentionally doped layers [83]. Neither approach is entirely satisfactory. Defects near the interface degrade the electrical properties of active layers of FETs grown directly on the substrate. Low unintentional doping ( $N_A = 10^{14} \text{ cm}^{-3}$ ,  $\rho = 10^2 \text{ ohm cm}$ ) is difficult to reproduce in MBE systems [103]. Recently Morkoç and Cho [104] described the characteristics of Cr-doped GaAs buffer layers grown by MBE. A related technique is proposed below; namely, the incorporation of Fe to obtain a high resistivity buffer layer ( $10^4$  to  $10^5 \text{ ohm cm}$ ). While Fe-doped GaAs layers have been prepared by vapor phase epitaxy [105], the possibility of growing Fe-doped GaAs using MBE has apparently not been recognized.

Doping processes in MBE cannot be simply deduced by examining the processes which describe the doping of GaAs layers deposited by chemical vapor transport and liquid phase epitaxial techniques. A number of questions must therefore be answered empirically in order to understand and control the incorporation of an impurity dopant in MBE layers. Is the molecular impingement rate for a particular dopant adequate to achieve the required concentration? How is the adsorbed dopant species incorporated into the bulk of the growing layer? What are the electrical properties of doped layers? Section 4.1 indicates that impingement rates extending to  $4 \times 10^{11} \text{ Fe molecules cm}^{-2} \text{ sec}^{-1}$  (equivalent doping level of  $5 \times 10^{19} \text{ cm}^{-3}$  for a GaAs growth rate of  $1.0 \text{ } \mu\text{m hr}^{-1}$ ) are obtained with Fe ovens operating

at temperatures below 1050 °C. The fundamental physical and electrical features of the Fe-doped layers are presented in Section 4.2. Section 4.2.1 summarizes the basic deposition parameters. Both Auger sputter profiles (Section 4.2.2) and SIMS profiles (Section 4.2.3) exhibit the marked segregation of iron near the outer surfaces of Fe-doped epilayers. The deep acceptor level in the photoluminescence data shown in Section 4.2.4 indicates that iron can be incorporated on a Ga site during the growth of GaAs by MBE under As-stabilized conditions. A shallow, compensated donor concentration of approximately  $10^{17} \text{ cm}^{-3}$  is observed in heavily-doped GaAs layers grown at substrate temperatures of 540 °C and growth rates of approximately  $1.0 \text{ } \mu\text{m hr}^{-1}$ . Closely compensated, high resistivity layers are obtained for GaAs grown at lower substrate temperatures and growth rates. Further details on these electrical characteristics are given in Section 4.2.5. While some control over the uniformity of a segregating dopant can be realized at the initial buffer layer/substrate interface by adjusting As/Ga flux ratios or by dopant predeposition [106], neither approach is satisfactory in obtaining a sharp interface between a Fe-doped buffer layer and the final active layer of a FET device.

#### 4.1 ANALYSIS OF IRON MOLECULAR BEAMS

The characterization of the iron emission flux levels is a particularly important aspect of the doping investigation. General procedures for using an ionization gauge to measure molecular beam intensities and actual flux data for the iron oven are given in Section 2.2.1 (p. 18). A quadrupole located 11.8 cm from the iron oven was also employed in monitoring the oven emission. Figure 13 shows the mass spectra that were recorded for three different source temperatures. The three most abundant iron isotopes,  $^{54}\text{Fe}$ ,

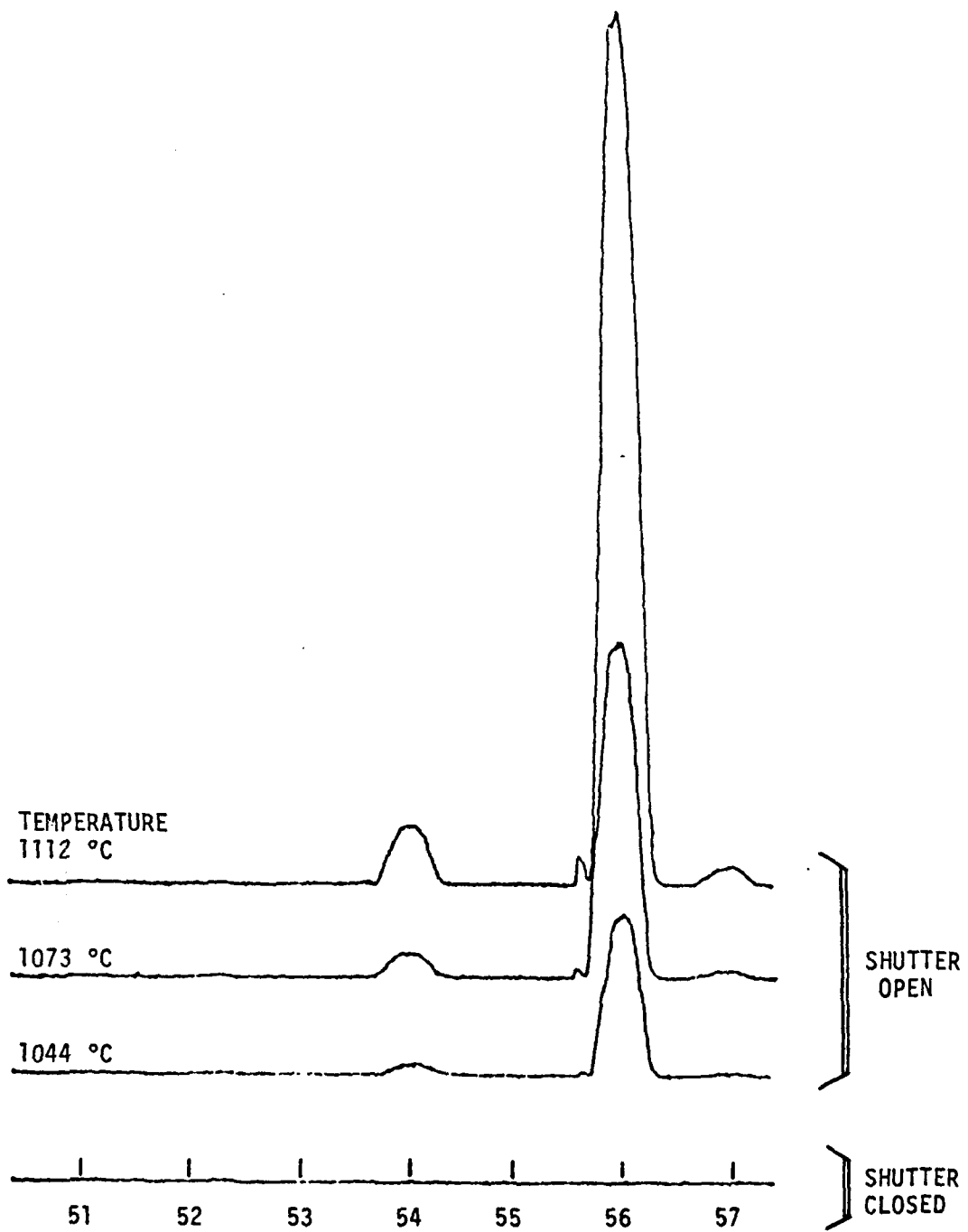


Figure 13. Mass Spectrum of Fe Isotopes Emitted as a Function of Iron Oven Temperature.

$^{56}\text{Fe}$ , and  $^{57}\text{Fe}$  are present in percentages that closely duplicate the levels of natural occurrence for these three isotopes (5.9, 91.5, and 2.2 percent, respectively). The molecular impingement rates associated with the output signals from the quadrupole and the ionization gauge can be transformed into equivalent doping levels assuming a GaAs growth rate of  $1.0 \mu\text{m hr}^{-1}$ , a sticking coefficient of unity, and that the flux at the substrate  $F_s$  is related to the flux at the detector  $F_d$  as

$$\frac{F_s}{F_d} = \left(\frac{\lambda_d}{\lambda_s}\right)^2 \quad (10)$$

where  $\lambda_d$  = oven to detector spacing and  
 $\lambda_s$  = oven to substrate spacing.

These transformed experimental data expressed in terms of the iron oven temperature are plotted in Figure 14. The solid line in Figure 14 is a theoretical curve computed from Equation 5 (p. 20) and the tabulated vapor pressure data for iron. Reasonably close agreement is obtained between these three sets of data.

Estimates of the upper limit of iron actually incorporated in three MBE GaAs epilayers grown at  $540^\circ\text{C}$  are also shown in Figure 14. The points were determined from an analysis of the level of compensation shown in Hall data for these n-type layers. While the electrical analysis is considered in some detail in Section 4.2.5 (p. 54), it is significant to note that, in this instance, the Fe flux is not easily related to the measured carrier concentration.

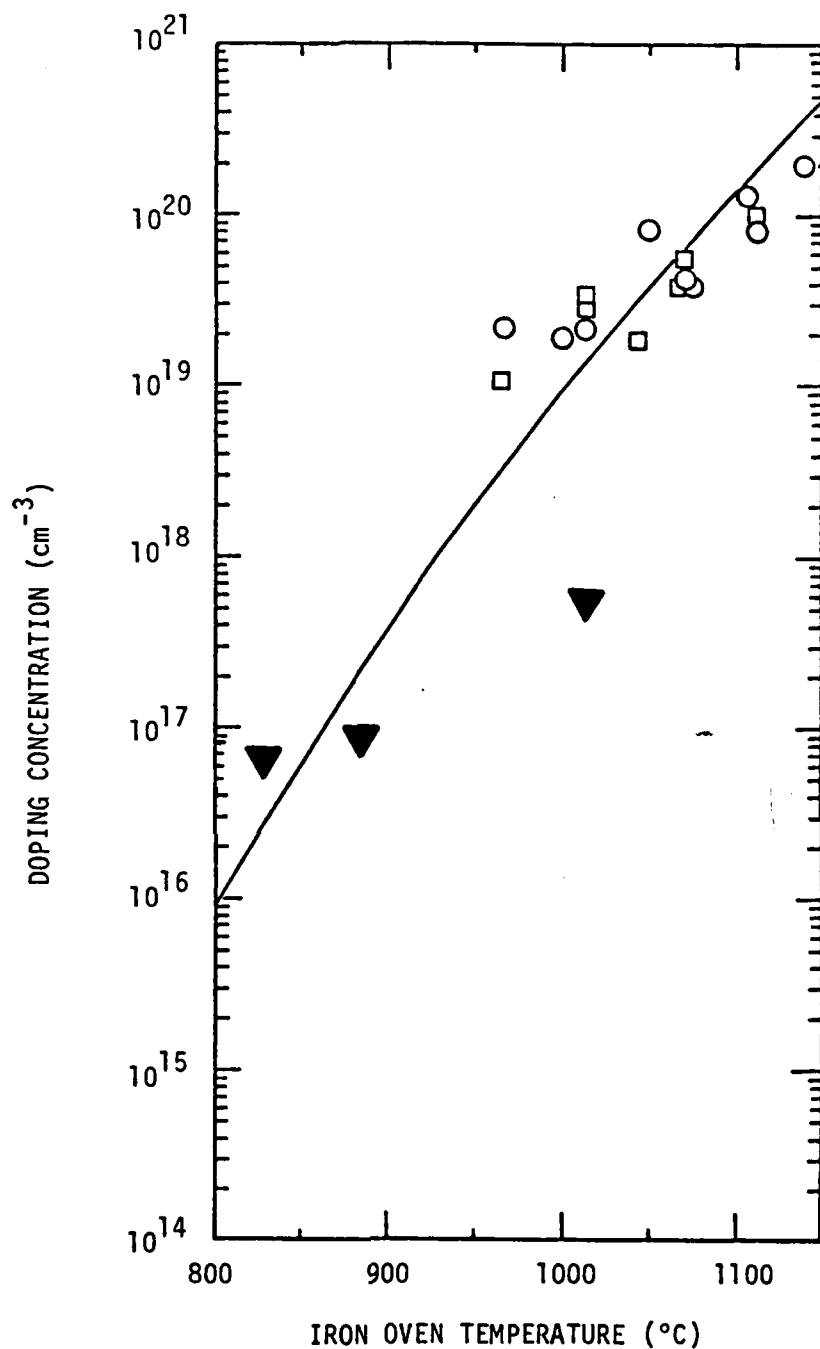


Figure 14. Doping Concentration vs Fe Oven Temperature. The Theoretical Curve was Computed from Tabulated Vapor Pressure Data for a GaAs Growth Rate of  $1.0 \mu\text{m hr}^{-1}$ . Open Experimental Points Denote Doping Levels Determined from Ion Gauge (O) and Quadrupole (□) Measurements of the Incident Iron Flux. The Solid Points Indicate the Upper Limit of Acceptor Concentrations Determined from Hall Measurements on Three Fe Doped MBE GaAs Layers.

## 4.2 INCORPORATION OF IRON IN MBE GaAs

### 4.2.1 General Characteristics

The effusion cells were loaded with 6N Ga (Alusuisse), 6N As (Preussag), m6N Ge (Alfa), and Specpure Fe wire (Johnson Matthey) which contained a total metallic impurity of approximately 15 ppm. The source-to-substrate spacing was 6.0 cm, and typical ranges for the operating temperatures of the Ga, Ge, and Fe ovens were 866 to 921 °C, 730 to 785 °C, and 805 to 1013 °C, respectively. Prior to loading in the MBE system, the polished (001) GaAs substrates were etched in  $\text{H}_2\text{SO}_4:\text{H}_2\text{O}_2:\text{H}_2\text{O}$  (5:1:1) and 2.0 percent Br in methanol [98]. The final step in the substrate cleaning procedure consisted of a rinse in hot DI water. This left the substrate preferentially covered with an oxide layer that was thermally desorbed in the ultra high vacuum system by heating the substrate to 600 °C for five minutes in an As pressure of approximately  $10^{-6}$  Torr just before epilayer growth.

All of the Fe-doped layers were grown under conditions of As-stabilized growth with As/Ga ratios ranging between 10 and 20. The major deposition parameters, target doping profiles, and probe-to-probe breakdown voltages for 14 Fe-doped MBE GaAs layers are given in Table 3. The crystalline quality of epilayers grown at lower substrate temperatures can be preserved by reducing the growth rate, and this practice was generally followed in growing the Fe-doped layers over a broad range of deposition conditions. Doping spikes were injected into layers B0313 and B0327. The spike regions were capped by 1.8 to 2.0  $\mu\text{m}$  thick regions that were uniformly doped with Fe. Both B0313 and B0327 were grown on  $n^+$ -GaAs substrates for Schottky barrier doping profile studies. Although the profile results were inconclusive, the 180 V probe-to-probe voltages measured on the outer surfaces

**Table 3. Summary of Deposition Parameters and Properties of Fe-Doped GaAs Layers Grown by MBE on (001) GaAs**

Layer	Thickness ( $\mu\text{m}$ )	Growth Rate ( $\mu\text{m hr}^{-1}$ )	$T_{\text{substrate}}$ ( $^{\circ}\text{C}$ )	$T_{\text{Ge}}$ ( $^{\circ}\text{C}$ )	$T_{\text{Fe}}$ ( $^{\circ}\text{C}$ )	$V_{\text{probe-probe}}$ (V)	Target Profile
B0212	4.7	1.2	540	*	828	28	uniform
B0213	4.9	1.2	540	*	882	20	uniform
B0214	4.1	1.0	540	*	1013	18	uniform
B0313	9.0	1.5	520	730	975/1000	180	spike
B0327	4.0	0.7	480	730	860/965	180	spike
B0330	3.2	0.5	460	*	870	>400	uniform
B0403	3.1	0.5	460	*	930	>400	uniform
B0405	~ 1.2	~ 0.5	460	730	880	>400	FET
B0406	~ 1.1	~ 0.5	459	730	820	>400	FET
B0411	1.4	0.5	456	784	805	14	FET
B0413	1.6	0.6	460	748	805	>400	FET
B0612	2.3	0.5	460	*	1000	94	spike
B0613	~ 1.1	~ 0.5	460	*	990	100	spike
B0614	2.9	0.6	462	860	1000	6	spikes

lie between the 18 to 28 V and > 400 V recorded for layers grown at higher and lower substrate temperatures, respectively. Layers B0612, B0613, and B0614 were also grown on  $n^+$ -GaAs. Narrow doping spikes of Fe and Ge were positioned in these samples designed for subsequent analysis of dopant segregation using SIMS. Constant fluxes were maintained in forming the Fe-doped portions of the remaining epilayers which were grown on Cr-doped substrates.

#### 4.2.2 Auger Analysis of Doping Profiles

Auger spectra show iron is incorporated nonuniformly in GaAs grown by MBE. This is evidenced from the strength of the characteristic Auger peaks for iron at the outer surface of samples where the doping profile was intended to be uniform.

A Physical Electronics Industries electron gun and cylindrical mirror analyzer (Model No. 10-155) mounted in a separate ultra high vacuum system were utilized in the initial Auger study. The Auger spectra for four Fe-doped layers shown in Figures 15 and 16 were taken on "as-received" surfaces. Some enhancement of the Fe, Ga, and As peaks would be observed if the thin surface oxides were removed by low energy, ion sputtering. In each case, the outer portions ( $\geq 1.8 \mu\text{m}$  thick) of these layers were grown with a constant flux of Fe molecules.

The growth conditions for layers B0214 and B0313 were adjusted to give an iron doping concentration  $\geq 10^{19} \text{ cm}^{-3}$ . Well resolved Fe responses at approximately 598, 651, and 703 eV are easily detected in the Auger spectra for these layers presented in Figure 15. The major LMM Auger electron transition for Ga (1070 eV) was at least 20 times larger than the Fe peaks. A much weaker response is shown in Figure 16 for layer B0327. This layer was

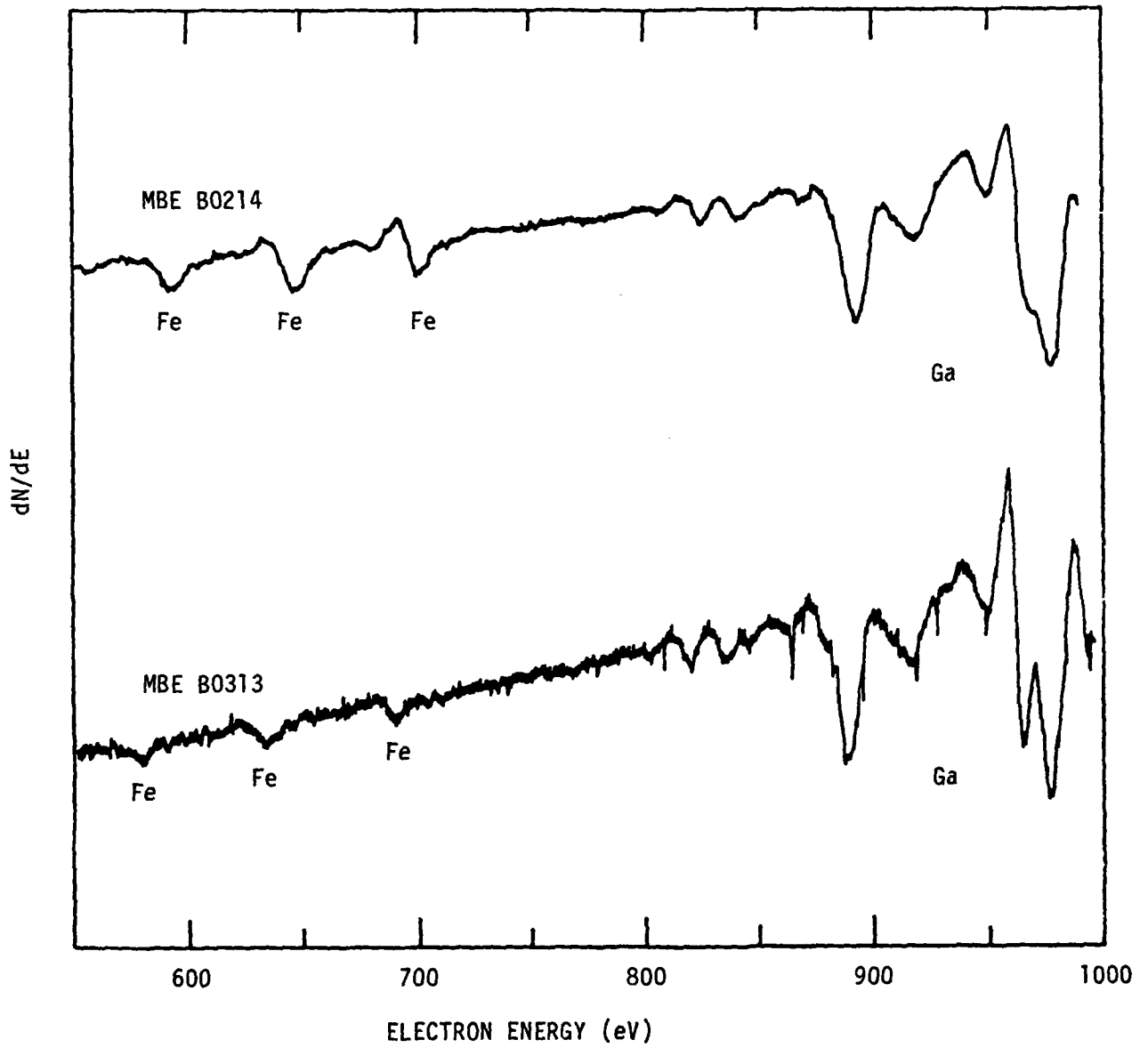


Figure 15. Auger Spectra Showing Fe at the Surface of GaAs Epilayers Grown at 540 °C (MBE B0214) and 520 °C (MBE B0313).

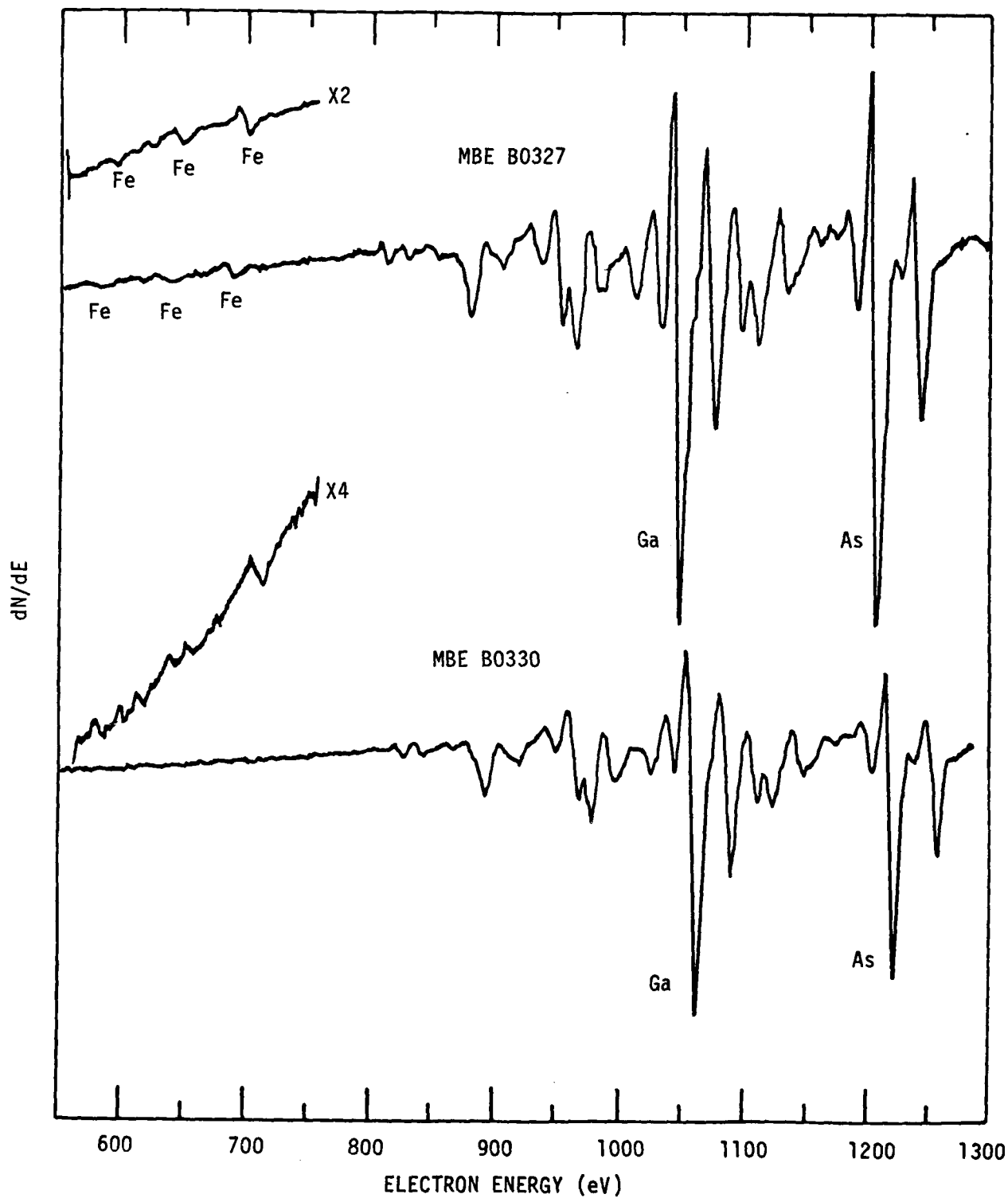


Figure 16. Auger Spectra Showing Trace of Fe at the Surface of GaAs MBE B0327 Grown at 480 °C. Iron, if Present on MBE B0330 (Grown at 460 °C), is < 0.01 Monolayer.

grown at a lower substrate temperature (480 °C) than the growth temperature for either B0214 (540 °C) or B0313 (520 °C). An effective Fe-doping level of  $4 \times 10^{18} \text{ cm}^{-3}$  was projected for layer B0327 based on the Fe oven temperature and the doping data given in Figure 14 (p. 41). Layer B0330 was grown at a substrate temperature of 460 °C and a targeted Fe-doping level of approximately  $4 \times 10^{17} \text{ cm}^{-3}$ . The spectra in Figure 16 for B0330 do not clearly resolve all three Fe peaks, and it is concluded that iron, if present at the surface of B0330, was below the limit of detectability of the available Auger equipment. The limiting Auger sensitivity is typically given as 0.01 monolayer. This corresponds to a doping level in GaAs on the order of  $10^{19} \text{ cm}^{-3}$ . Although the intensities of the Fe peaks shown in Figure 15 and 16 decrease with decreasing flux intensity, the observed concentrations of Fe are at least an order of magnitude higher than the projected doping levels.

A nonuniform distribution of iron at the surface of MBE GaAs layers is revealed in Auger analyses conducted at the Naval Research Laboratory. Figure 17 presents composition-depth profiles of layers B0214 and B0327. The oxygen Auger peak was simultaneously monitored during the generation of the profiles, and this peak decreased by a factor of three in passing from the oxidized surface region to the layer interior. Since the escape of Auger electrons is typically on the order of 10 to 15 Å, the Fe response increases as the oxide is being stripped away. A marked segregation of iron is strikingly exhibited for both specimens.

#### 4.2.3 SIMS Analysis of Doping Profiles

Gallium arsenide epilayers were prepared which contained special test profiles for a SIMS study of iron segregation. The layers were grown

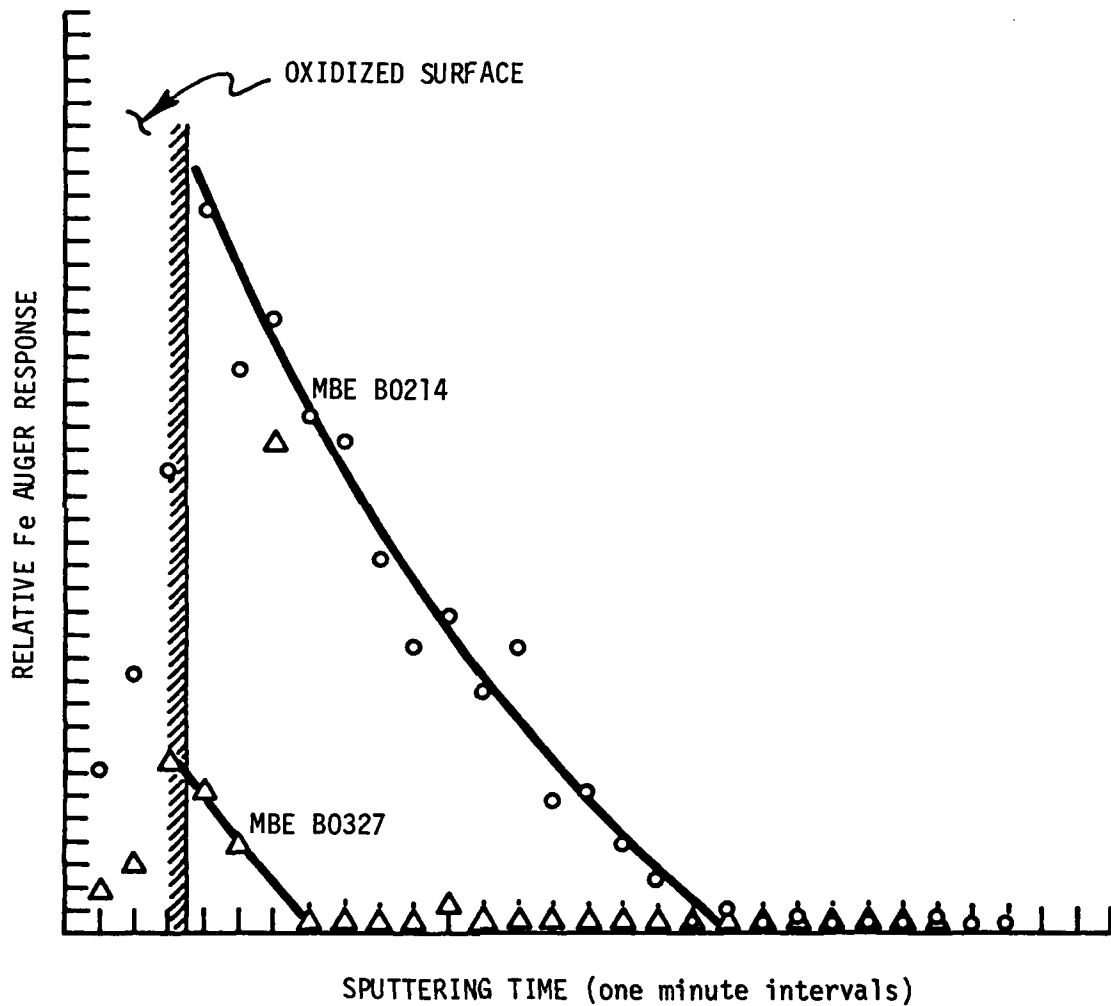


Figure 17. Profile of Iron Concentration Near the Surface of Two Fe-Doped GaAs Layers Grown by MBE

at a temperature of 460 °C on (001) GaAs substrates doped with Si ( $5 \times 10^{18} \text{ cm}^{-3}$ ). The low growth temperature was intentionally selected to minimize segregation effects. Shutters controlled the doping injection, and the epilayer growth was not stopped until the completion of a run. A narrow iron doping spike ( $\leq 10^{19} \text{ cm}^{-3}$ ) was located at the surface of layer B0613. For layer B0612, an Fe-doped section ( $\leq 10^{19} \text{ cm}^{-3}$ ) approximately 0.3  $\mu\text{m}$  thick was sandwiched between two unintentionally doped regions each 1.0  $\mu\text{m}$  thick. Epilayer B0614 was grown with a central Fe spike located just beneath a 1.3  $\mu\text{m}$  thick surface layer doped with Ge ( $\approx 4 \times 10^{18} \text{ cm}^{-3}$ ). The latter was formed to test the effectiveness of Ge as a collection site for segregating Fe atoms.

The SIMS profiles of layers B0613 and B0612 are presented in Figures 18 and 19, respectively; and there is no doubt that most of the Fe is accumulating at the outer surface. The vertical positions of the theoretical doping profiles have been located in Figures 18 and 19 by assuming that the total number of incident Fe molecules determined from the flux measurements are proportional to the total sum of  $^{56}\text{Fe}$  counts for each profile. The relative magnitudes of the spikes in each case are within a factor of 3.5 of the spike height estimated from an Auger measurement of the concentration of Fe at the outer surface of the doped epilayer. Less than six percent of the incident Fe appears to be incorporated in the GaAs lattice during the period of direct exposure to the doping flux from the iron oven. The central spike for layer B0612 is well defined, and there is only slight evidence of the typical thermal diffusion effects which would round the roof of the rectangular Fe spike and broaden the skirts of the spike into a Gaussian shape [107]. The SIMS profile for layer B0614

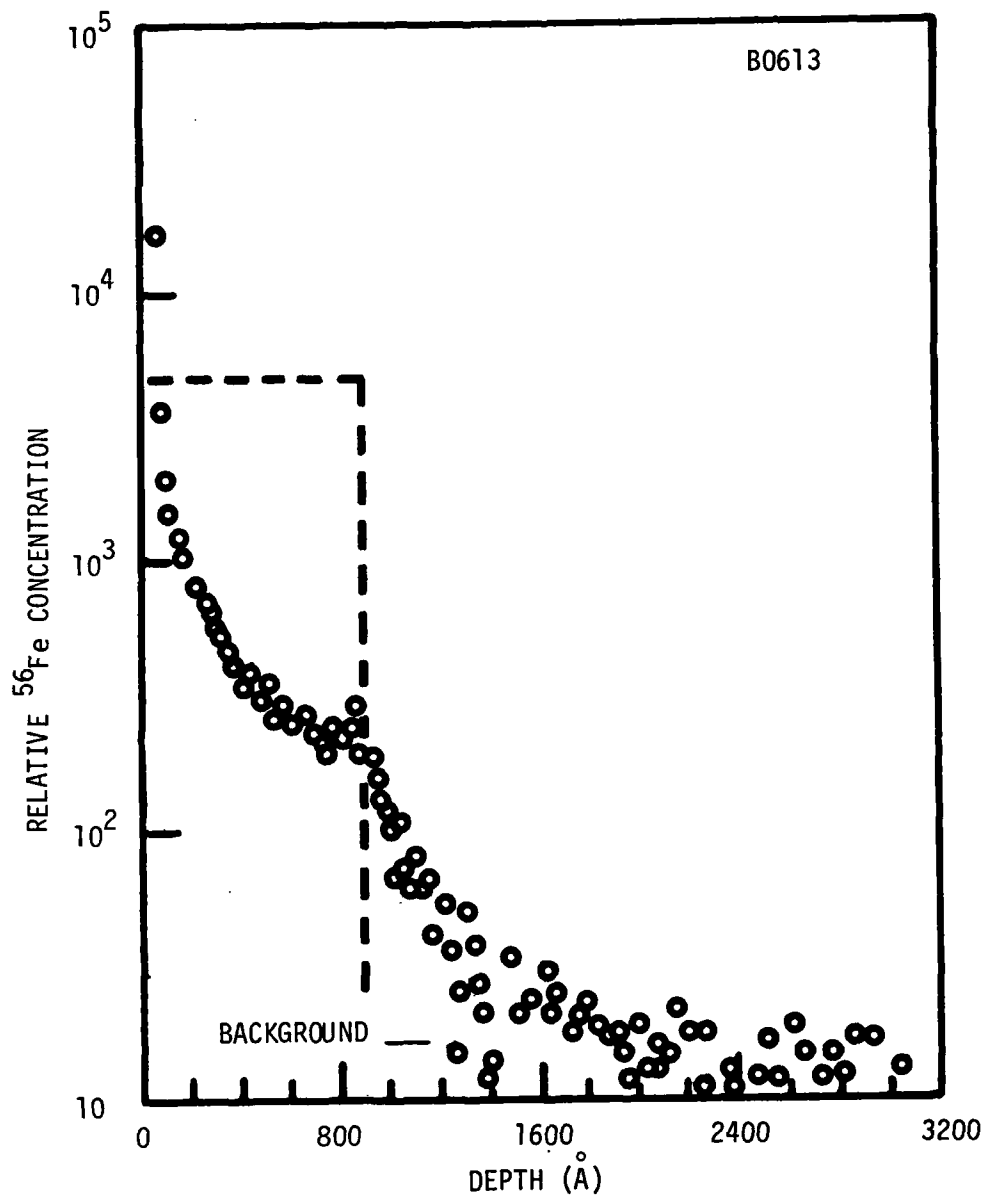


Figure 18. SIMS Profile Showing the Segregation of  $^{56}\text{Fe}$  which was Initially Introduced as a Surface Doping Spike (Dotted) During the MBE Growth of GaAs Layer B0613.

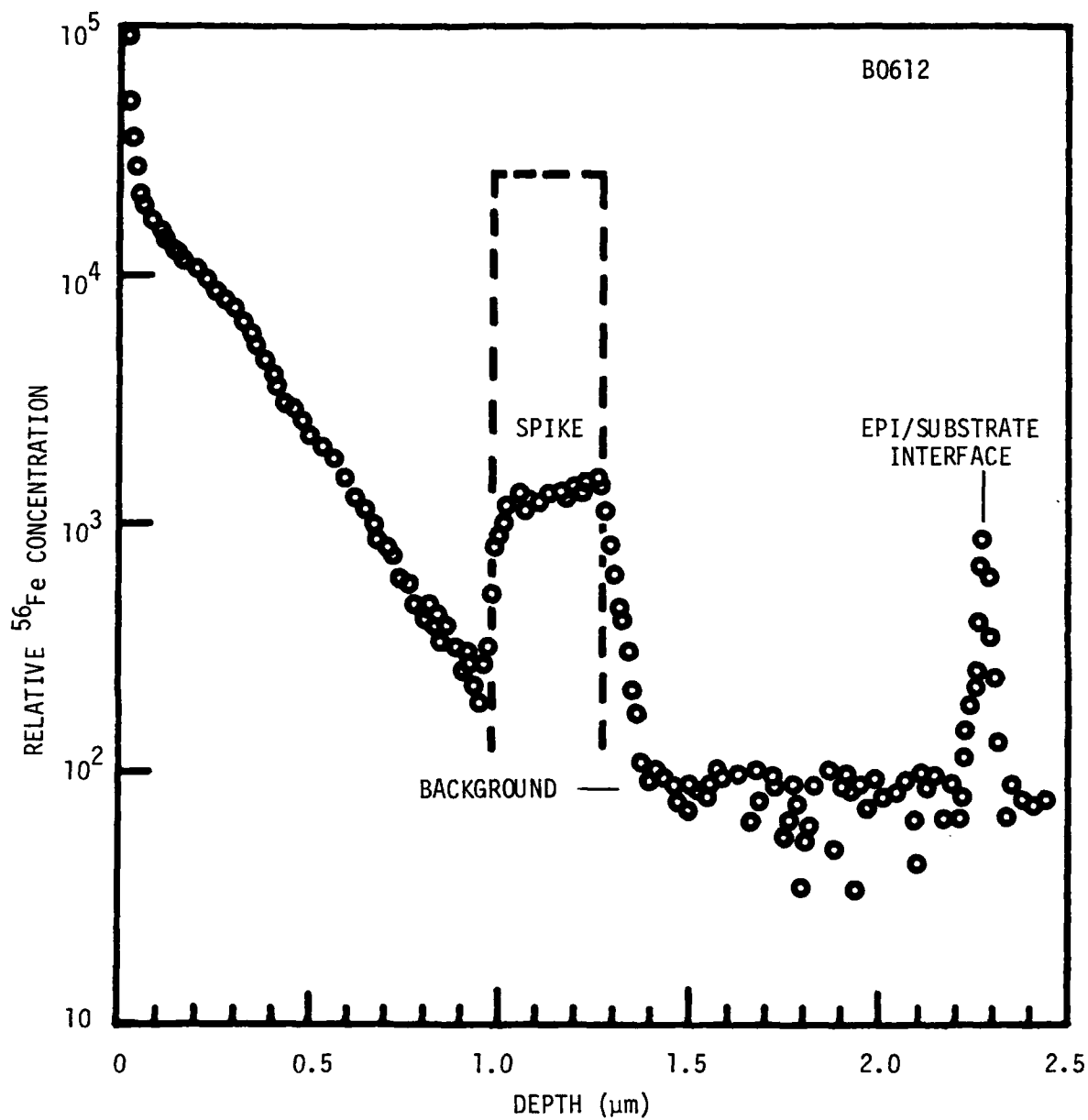


Figure 19. SIMS Profile Showing the Segregation of  $^{56}\text{Fe}$  which was Initially Introduced as a Central Doping Spike (Dotted) During the MBE Growth of Layer B0612.

was very similar to the profile shown in Figure 19 for layer B0612. There was no significant reduction of Fe segregation in the Ge-doped surface region.

What remains unclear at this point is a satisfactory theory to explain the gradual increase in Fe incorporated in layers B0612 and B0614 after the Fe beam was abruptly shut-off. Additional work with ion implanted layers is underway at NRL which will further explore this unexpected result.

#### 4.2.4 Photoluminescence Spectra

Photoluminescence spectra near the band edge for four of the Fe-doped GaAs layers listed in Table 3 (p. 43) are presented in Figure 20. These layers were selected to illustrate the changes in the emission spectra as a function of two parameters; namely, lowering the substrate temperature from 540 °C (layer B0213) to 460 °C (layer B0330) and increasing the iron flux from  $1.8 \times 10^8$  molecules  $\text{cm}^{-2} \text{sec}^{-1}$  (layer B0212) to  $1.7 \times 10^{11}$  molecules  $\text{cm}^{-2} \text{sec}^{-1}$  (layer B0214) at a constant substrate temperature of 540 °C. The emission spectra were run at the University of Dayton using a photomultiplier tube and a nitrogen-cooled PbS detector. The excitation source was a Kr laser operating at 6471 Å with a maximum power of 500 mW.

The weak bands labeled E in Figure 20 at 1.514 eV are attributed to exciton and valance band to donor transitions. The disappearance of this line for layer B0330 is probably due to a higher incidence of residual defects that are incorporated during growth at 460 °C. It is also likely that lattice defects arising from the heavy iron doping cause this line to be missing in the spectrum for layer B0214. There is a broad band DC at 1.438 eV for the latter layer which may be associated with an As vacancy defect complex [108]. Other lines (free to bound acceptor) observed in

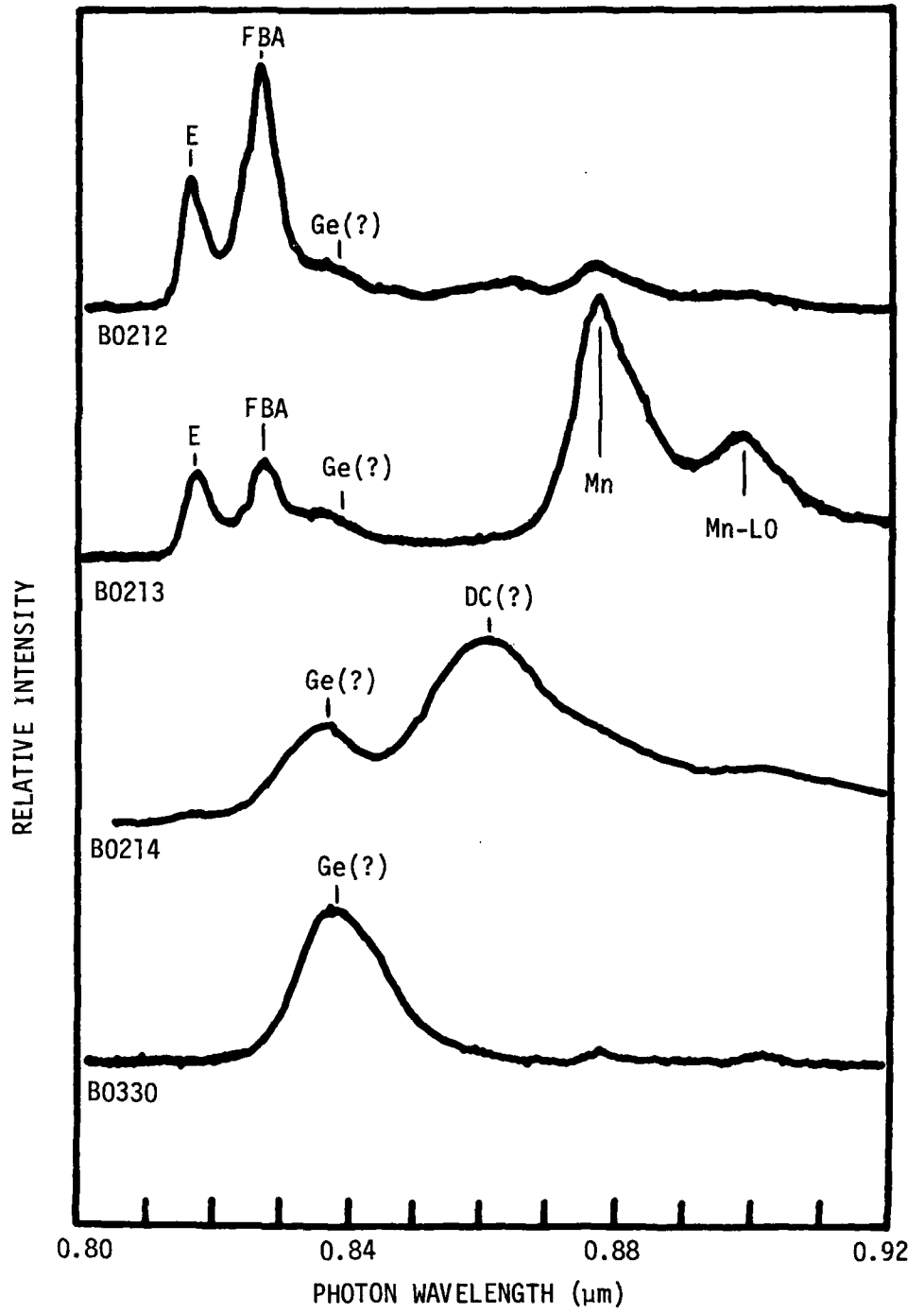


Figure 20. Photoluminescence Spectra Near the Band Edge for Four Fe-Doped GaAs Layers Grown by MBE.

the near band emission are an unidentified acceptor at 0.019 eV (FBA), Ge (0.040 eV), and Mn (0.100 eV).

Lying deeper in the gap for layer B0214 (Figure 21) is a partially resolved  $\text{Fe}^{2+}$  internal transition at 0.371 eV that provides positive confirmation that Fe is occupying a Ga site in the lattice structure. Although the four lines which actually comprise this emission have been observed in bulk GaAs, this is believed to be the first report of an  $\text{Fe}^{2+}$  transition in a GaAs epilayer. A deep  $\text{Fe}^{2+}$  line may also be present in layer B0330, however, the low signal to noise ratio makes this a rather tenuous observation.

#### 4.2.5 Electrical Properties

A relatively complex doping pattern is emerging for iron incorporated during the MBE growth of GaAs. The traditional concept which simply associates Fe with a deep acceptor level in GaAs does not adequately describe all the electrical characteristics observed for Fe-doped MBE layers. At high substrate temperatures (540 °C), n-type growth was obtained. The layers were characterized by low breakdown voltages and doping levels of approximately  $10^{17} \text{ cm}^{-3}$ . At lower substrate temperatures (460 °C) high resistivity layers were formed. Three of four layers grown with FET profiles and Fe-doped buffer layers also contained highly resistive active layers. Since the electrical properties of the Fe-doped layers are such a strong function of substrate temperature, this parameter is a natural classifier in organizing the following discussion.

##### *Fe-Doped, MBE GaAs Grown at 540 °C*

Before initiating the Fe-doping study, two 3.9  $\mu\text{m}$  thick GaAs layers, B0207 and B0208, were grown at 540 °C to establish the background doping level. Both layers were n-type with a room temperature concentration of

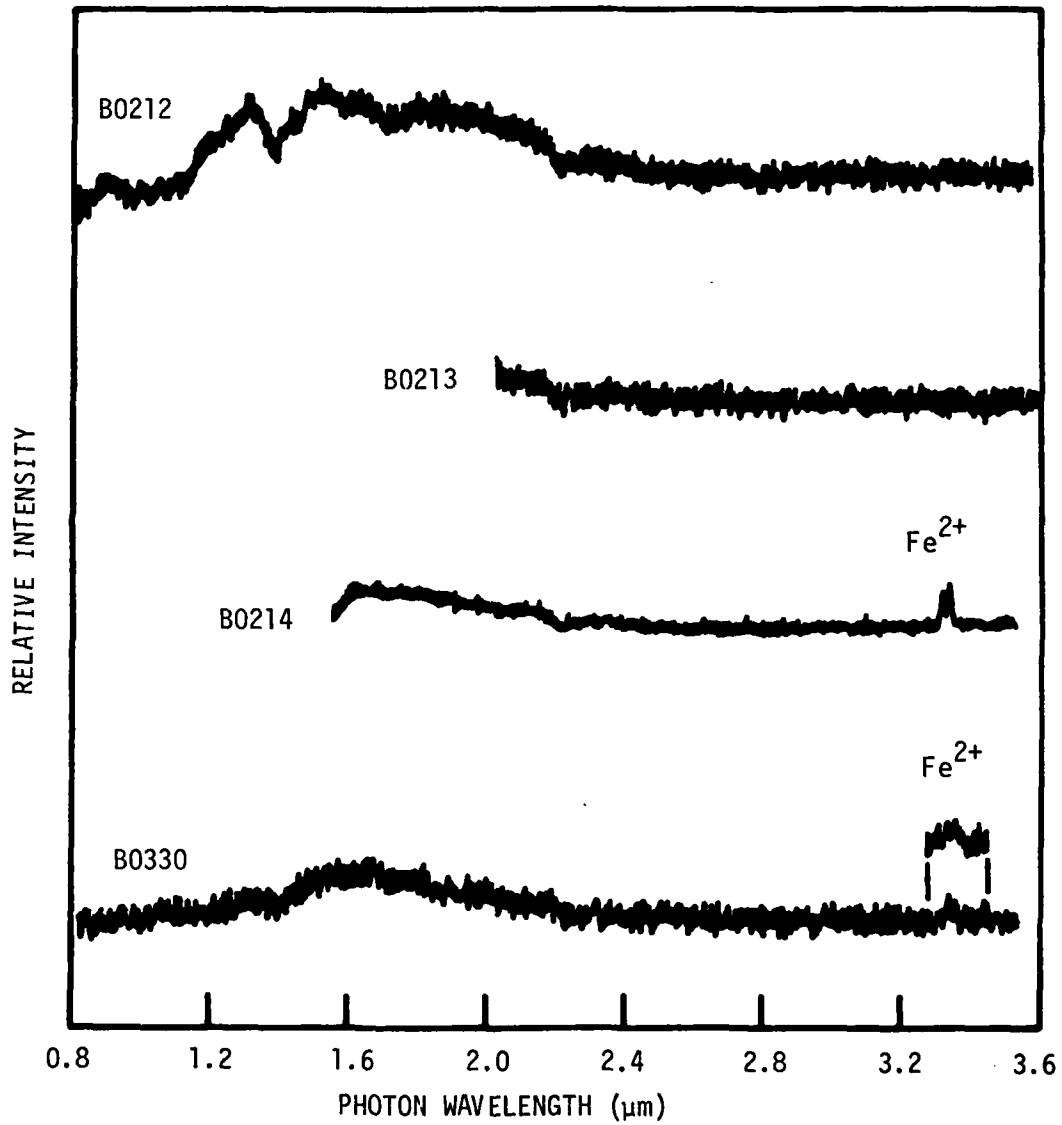


Figure 21. Photoluminescence Spectra in the Mid-Band Gap Region for Four Fe-Doped GaAs Layers Grown by MBE

$1.1 \times 10^{16} \text{ cm}^{-3}$ . An extended series of mixer and Gunn diodes had been grown in the MBE system which required a total of 29.0 hours of buffer layer growth doped n-type with Ge at concentrations of  $3 \times 10^{18} \text{ cm}^{-3}$ . The high residual background in the system may be a direct result of the heavy doping required in these device runs.

The donor that was observed in the three Fe-doped GaAs layers grown at 540 °C has several unique characteristics. Room temperatures values of carrier mobility and concentration determined from van der Pauw measurements [109] for B0212, B0213 and B0214 are given in Table 4. The donor concentration increases only slightly as the iron oven temperature increases from 828 °C to 1013 °C. The electrically active carrier concentration for layer B0214 does not correspond to the iron concentration greater than  $10^{19} \text{ cm}^{-3}$  that was confirmed by the Auger studies. Although there was little change in carrier concentration, there was a significant decrease in mobility  $\mu$  and increase in the level of compensation  $\theta_c$  as the iron flux increased.

Three techniques were used to determine  $\theta_c$  (ratio of ionized acceptors  $N_A^-$  to ionized donors  $N_D^+$ ). The first approach was based on the sensitivity of  $\mu_{300}$  to compensation. Values of  $\theta_c$  were directly interpolated from tabulated data of  $\mu_{300}(\theta_c)$  derived from variational solutions of the transport equation [110]. The second approach employed values of carrier concentration and mobility measured at liquid nitrogen temperatures to enter extrapolated empirical curves of  $\mu_{77}$  vs.  $N_D + N_A$  derived from a Brooks-Herring formulation for ionized impurity scattering [111]. Finally, the  $\mu$  vs. T data for layers B0212, B0213, and B0214 plotted in Figure 22 also show greater compensation for layers grown at higher iron oven temperatures.

Table 4. Deposition Parameters, Thicknesses, and Electrical Properties (296 °K) for Fe-doped Epilayers Grown on Cr-Doped (001) GaAs.

Layer	Thickness ( $\mu\text{m}$ )	Growth Rate ( $\mu\text{m hr}^{-1}$ )	$T_{\text{substrate}}$ ( $^{\circ}\text{C}$ )	$T_{\text{Fe}}$ ( $^{\circ}\text{C}$ )	Carrier Type	Concentration ( $\text{cm}^{-3}$ )	Mobility ( $\text{cm}^2\text{V}^{-1}\text{sec}^{-1}$ )	$N_{\text{A}}^{-}/N_{\text{D}}^{+}$	
								(a)	(b)
MBE B0212	4.7	1.2	540	838	n	$1.2 \times 10^{17}$	4284	0.27	0.54
MBE B0213	4.9	1.2	540	882	n	$1.7 \times 10^{17}$	4023	0.28	0.59
MBE B0214	4.1	1.0	540	1013	n	$1.8 \times 10^{17}$	1989	0.72	0.89

(a) data based on a variational solution of the transport equation [110]

(b) extrapolated data based on Brooks-Herring formulation [111]

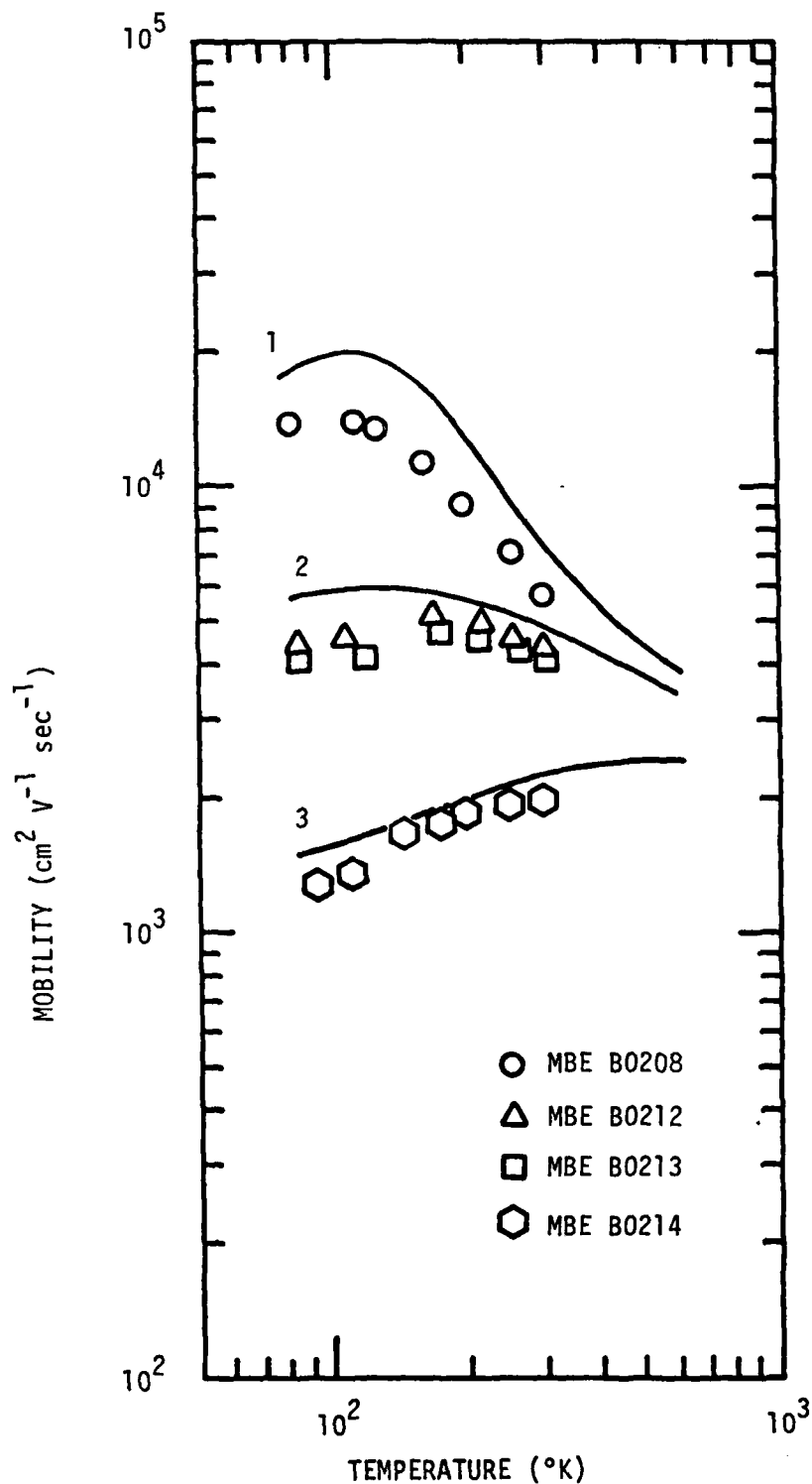


Figure 22. Hall Mobility for Unintentionally Doped (B0208) and Fe-Doped MBE GaAs Layers vs Temperature. Experimental Data for These n-Type Layers are Compared with Theoretical  $\mu(T)$  Curves for Compensated Material,  $\theta_c = N_A^-/N_D^+$ : 1)  $n_{300} = 1 \times 10^{16} \text{ cm}^{-3}$ ,  $\theta_c = 0.4$ ; 2)  $n = 1.5 \times 10^{17} \text{ cm}^{-3}$ ,  $\theta_c = 0.3$ ; 3)  $n = 1.5 \times 10^{17} \text{ cm}^{-3}$ ,  $\theta_c = 0.75$ .

The theoretical curves of  $\mu(T)$  were computed by assuming the validity of Matthiesen's rule

$$\mu^{-1} = \sum_i (\mu_i)^{-1} \quad (11)$$

for the component mobility contributions arising from polar optical mode scattering, piezoelectric scattering, deformation potential scattering, and ionized impurity scattering [111-113]. Details of the mathematical solution of Equation 11 in terms of  $n$ ,  $\theta_c$ , and  $T$  are presented in Appendix I. Theoretical curves for  $\mu(T)$  using  $n$  and  $\theta_c$  values which are representative of the epilayers listed in Table 4 are plotted in Figure 22. The relatively good agreement between the experimental  $\mu(T)$  data and the theoretical  $\mu(T)$  curves further confirms the observation that lower mobilities and higher levels of compensation correspond to growth at higher incident Fe fluxes. The conclusion that the increased compensation is derived from the deep level associated with an increased incorporation of Fe on a Ga site must be tempered by the realization that the higher doping flux also appeared to increase the level of residual defects in the lattice.

The donor found in Fe-doped layers grown at 540 °C is an enigma. Impurities in the Fe oven could, of course, lead to the incorporation of an unintentional donor. This possibility is judged unlikely since the impurities would need to survive the 1200 °C outgassing of the iron oven and load. Furthermore, there was little increase in the donor concentration with a substantial 200 °C increase in the Fe oven temperature.

Iron has traditionally been considered to be an acceptor in GaAs with a level lying between 0.35 and 0.52 eV above the valence band edge [114-117].

Assuming a single donor and a single acceptor level, an analysis [118] of the Fermi level position using the charge neutrality condition

$$n + \sum_i N_{Ai}^- = p + \sum_j N_{Dj}^+ \quad (12)$$

and resistivity data as a function of temperature for layer B0214 indicated that the donor level was very shallow (0.002 eV) in comparison to the typical ionization energy for donors in GaAs (0.005 eV). However, in this model the Fermi level at 77 °K (0.008 eV) was still too far away from the conduction band to explain the low resistivity actually measured for layer B0214 at liquid nitrogen temperatures. Thus, the shallow donor may not be well represented by a single, hydrogen-like substitutional impurity [119]. There may instead be a series of shallow donor levels, and/or level positions with respect to the band edge may be a changing function of temperature.

*Fe-Doped, MBE GaAs Grown at 460 °C*

At the other extreme, semi-insulating layers were obtained when GaAs layers were exposed to beams of Fe molecules during growth at substrate temperatures of 460 °C. Table 3 (p. 43) indicates that the probe-to-probe voltages for uniform Fe-doping profiles exceed 400 V. Hall measurements are more complicated for high resistivity semiconductor epilayers a few  $\mu\text{m}$  thick, and no Hall data were obtained at the  $10^{-9}$  A currents drawn by these samples.

Four layers with FET profiles and Fe-doped buffers were grown at 460 °C. With the exception of the change in the Fe-doping level, layers B0405 and B0406 were grown under otherwise similar conditions. In both layers, the closing of the Fe oven shutter coincided with the opening of the Ge

shutter. The temperature of the latter oven was adjusted to form the n-type channel approximately 0.3 to 0.4  $\mu\text{m}$  thick which was doped at  $1.0 \times 10^{17} \text{ cm}^{-3}$ . The active layers of B0405 and B0406 showed the high probe-to-probe voltages characteristic of semi-insulating material. Auger analyses of both FET layers did not detect the presence of iron at the active layer surfaces.

The impinging iron flux was further reduced to a level which would just compensate the residual background donor; and two FET layers, B0411 and B0413, were grown with modified buffer regions. In constructing the modified buffer, a submicron thick, unintentionally doped region was positioned between the 1.0  $\mu\text{m}$  thick Fe-doped region and the 0.4  $\mu\text{m}$  thick Ge-doped active region. An unintentionally doped region 610  $\text{\AA}$  thick was too thin to prevent compensation of the n-type ( $2 \times 10^{17} \text{ cm}^{-3}$ ) active layer for B0413.

Following the modified buffer with a more heavily doped active region (n-type doping =  $7 \times 10^{17} \text{ cm}^{-3}$ ) yielded a FET profile for B0411. The dependence of carrier mobility along the thickness direction ( $z$ ) of the active layer was monitored by sequentially removing thin surface sections ( $\text{H}_3\text{PO}_4:\text{H}_2\text{O}:\text{H}_2\text{O}_2$  etch) [120] and remeasuring the sheet conductivity  $\sigma_s$  and sheet Hall coefficient  $R_{hs}$  at each step. The mobility of the removed section can be expressed as [121]:

$$\mu(z) = \frac{1}{\sigma(z)} \frac{d(R_{hs}\sigma_s^2)}{dz} \quad (13)$$

where

$$\sigma(z) = \frac{d\sigma_s}{dz}$$

and the derivatives are reduced to differentials. Plots of the thickness dependent mobility vs. temperature are given in Figure 23 for layer B0411. The highest mobility is found near the center of the active region. Lower mobilities were obtained at the active layer boundary planes. Based on the data in Figures 22 and 23, compensation levels in the active region are estimated to be approximately 0.3 to 0.4. Such values have been observed for other Ge-doped MBE layers grown under As-stabilized conditions [98].

As the substrate temperature during growth is reduced, the limited electrical data indicate that Fe-doped layers become more highly resistive. The comparatively high mobility at a doping level of  $7 \times 10^{17} \text{ cm}^{-3}$  for layer B0411 shown in Figure 23 provides some validation of the lateral integrity of the crystalline structure of layers grown at 460 °C as far as electrical transport properties are concerned. There certainly is an increased likelihood of incorporating deep level defects as the growth temperature is lowered, however, which augurs ill for high performance FETs. Previous experience with GaAs mixer diodes grown on Ge substrates at 460 °C does not suggest that deep level structural defects will compensate GaAs epilayers intentionally doped n-type at  $10^{17}$  and  $10^{18} \text{ cm}^{-3}$  levels (Section 3.1, p. 31). Since iron has been shown to accumulate at the outer surface of MBE GaAs, the thin active layers doped at 1 to  $2 \times 10^{17} \text{ cm}^{-3}$  in the remaining three FET profiles could be inadvertently compensated by a narrow spike of segregated iron from the buffer layer doping.

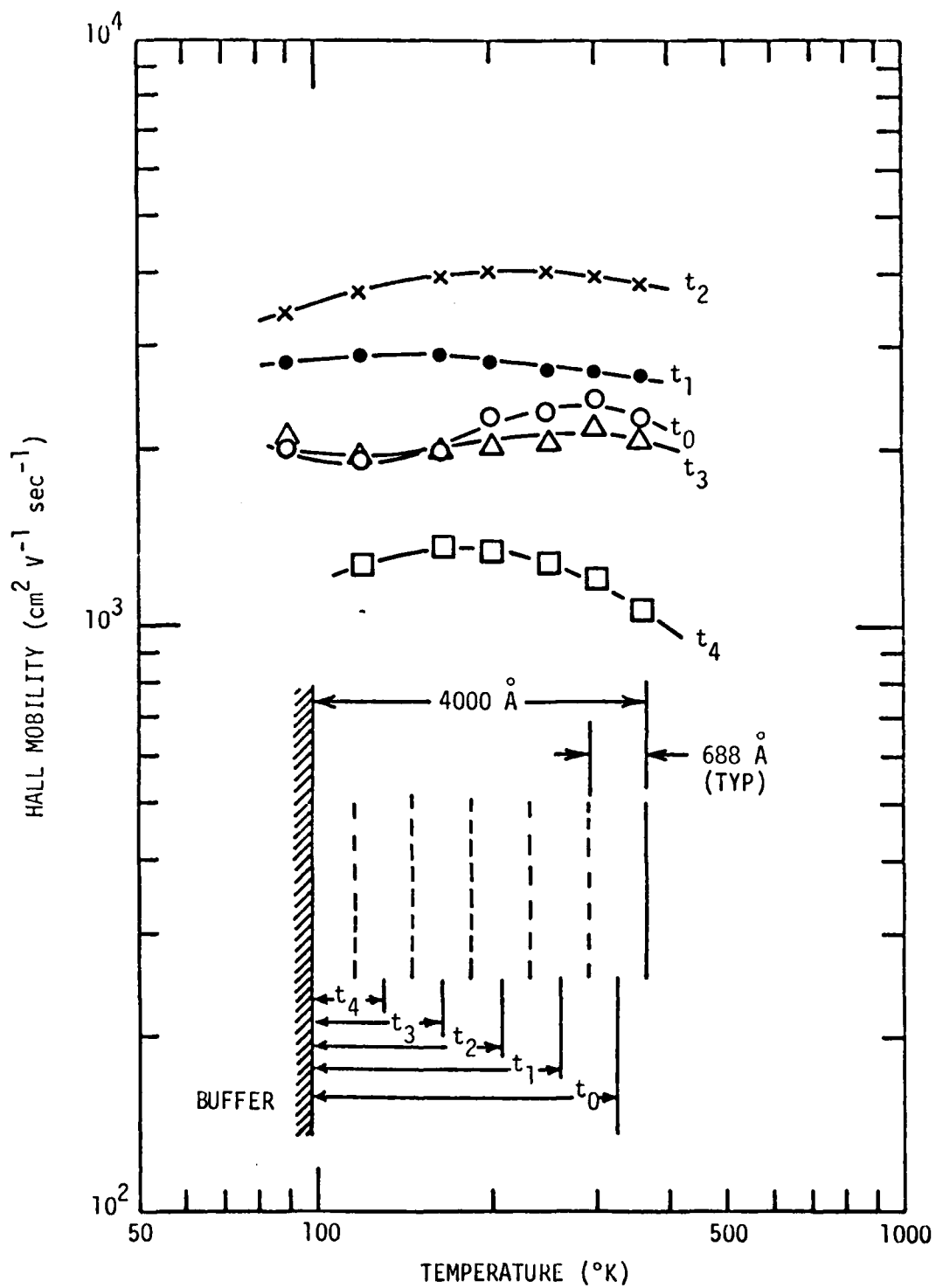


Figure 23. Mobility vs. Temperature Variation in the n-Type Active Region ( $7 \times 10^{17} \text{ cm}^{-3}/\text{Ge}$ ) Deposited on a  $1.0 \mu\text{m}$  Thick Fe-Doped Buffer in Specimen B0411

## 5.0 INVESTIGATION OF TERNARY SEMICONDUCTORS

The investigation of the heteroepitaxial growth of multicomponent, alloy semiconductors by MBE was initiated with the ternary  $\text{In}_x\text{Ga}_{1-x}\text{As}$ . A lattice match is obtained between this ternary and an InP substrate where the composition  $x = 0.53$  [3]. The low bandgap of 0.74 eV and difficulties in forming Schottky barriers may limit the usefulness of  $\text{In}_{0.53}\text{Ga}_{0.47}\text{As}$  for FET applications [26,122,123], however, the material has interesting potential applications in lasers and photodetectors operating in the 1.6  $\mu\text{m}$  region. Preliminary results have been obtained for  $\text{In}_x\text{Ga}_{1-x}\text{As}$  layers grown by MBE on both InP and GaAs substrates. Areas which received the greatest emphasis during the work on InP substrates were as follows:

- definition of system operating parameters (Section 5.1.1),
- development of a procedure for preparing InP substrates for epitaxial growth in MBE systems (Section 5.1.2), and
- the control and analysis of layer properties (Section 5.1.3).

Although the cleaning and passivation procedure appears to produce InP surfaces that are free of chemical contamination, the electrical properties of  $\text{In}_{1-x}\text{Ga}_x\text{As}$  layers grown on these surfaces were noticeably inferior to layers grown with an intentional, lattice mismatch  $\delta$  between the  $\text{In}_x\text{Ga}_{1-x}\text{As}$  layers and GaAs substrates. As Section 5.2.1 indicates, the surface morphology of the ternary layers grown on GaAs deteriorates rapidly for  $x \geq 0.2$  ( $\delta \geq + 0.013$ ). In addition to the morphological changes at the higher compositions, there was an increase in electron concentration and a decrease in carrier mobility (Section 5.2.2). A residual donor dominates the unintentional doping of the  $\text{In}_x\text{Ga}_{1-x}\text{As}$  layers grown on both InP and GaAs substrates.

## 5.1 GROWTH OF $\text{In}_x\text{Ga}_{1-x}\text{As}$ on InP

### 5.1 Oven Temperatures and Ternary Compositions

The basic experimental considerations governing the growth of  $\text{In}_x\text{Ga}_{1-x}\text{As}$  by MBE can be set forth in terms of a simplified model. The alloy composition is predominantly determined by the arrival rates of the two group III elements. An excess As flux can be directed toward the growing layer since the incorporation of As proceeds in proportion to the free In and Ga adsorbed on the surface. The sticking coefficients for In and Ga are essentially unity for growth temperatures on the order of 400 to 500 °C.

The impingement rates of In and Ga molecules can be directly related to the temperatures of ovens containing these elements as shown in Figure 8 (p. 21). The growth rate of  $\text{In}_x\text{Ga}_{1-x}\text{As}$  is determined by the sum of the arrival rates of In and Ga. A series of growth rate calculations have been completed using the expressions given in Section 2.2.1 (p. 18) and the results are displayed in Figure 24. This chart maps the general range of oven temperatures required to hit a target value of composition and growth rate. Information of this type can minimize the time spent in selecting a set of optimum deposition parameters for a practical MBE system.

### 5.1.2 Passivation of InP Substrates

A substrate cleaning procedure has been investigated which leaves (100) InP substrates with a passivating layer of oxygen at the outer surface. Carbon and oxygen contamination could not be detected by Auger electron spectroscopy (AES) analyses of the passivated surfaces after heating in an ultra high vacuum system. The absence of adsorbed carbon is a particularly desirable feature of the cleaning procedure. Once carbon has formed on

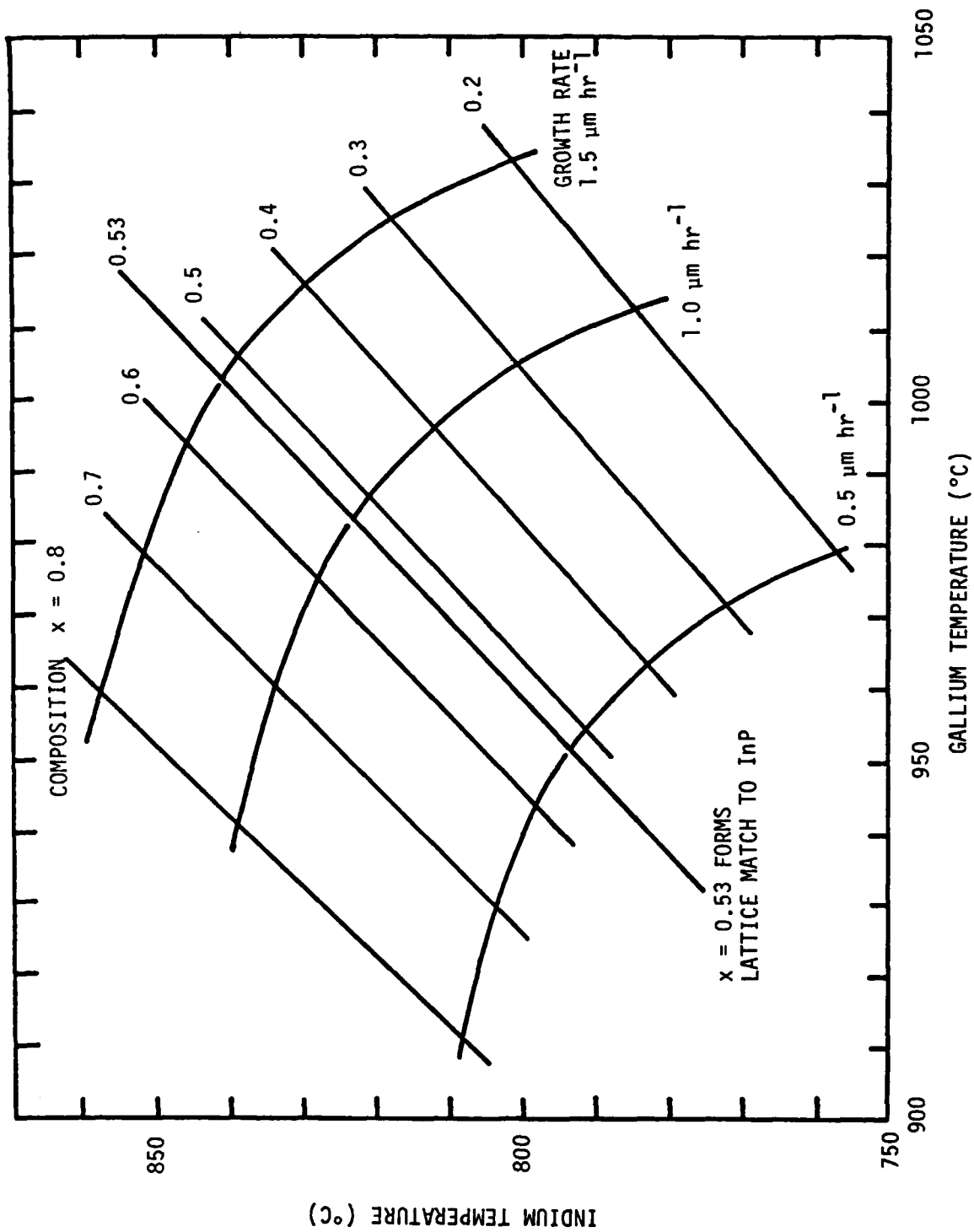


Figure 24. Composition and Growth Rate of  $\text{In}_x\text{Ga}_{1-x}\text{As}$  as a Function of In and Ga Oven Temperatures.

semiconductor surfaces, the surface must be cleaned by ion bombardment. The disordered structure of the ion-bombarded surfaces must then be removed before epitaxial growth by carefully annealing the substrate [36,37].

The wet chemical cleaning and etching process for mechanically polished InP substrates is listed in Table 5. The process is an outgrowth of the processing that has been followed in preparing GaAs substrates for epilayer growth by CVD and MBE [98]. The fundamental operations underlying the procedure given in Table 5 include washing and the removal of particulate matter, vapor degreasing, chemical etch/polishing, and surface passivation.

Table 5. InP Substrate Cleaning Procedure

1. Hot DI H<sub>2</sub>O wash, methanol rinse, N<sub>2</sub> blow dry.
2. Vapor degrease in boiling trichlorethylene vapor for two minutes.
3. Methanol rinse, N<sub>2</sub> blow dry.
4. Etch 2 minutes in Br:methanol (1:99 volume ratio)
5. Methanol wash for 30 sec.
6. Hot DI H<sub>2</sub>O wash for one min.
7. N<sub>2</sub> blow dry.

Time dependent profiles of Auger data and substrate temperature for two InP substrates are shown in Figure 25. Sputter cleaning by ion bombardment was not employed at any stage during these studies. The initial Auger spectra for both substrates exhibited a strong oxygen response (KLL transition). Thermodynamic considerations of the free energy of formation for bulk processes indicate that the oxygen will be bound more tightly to

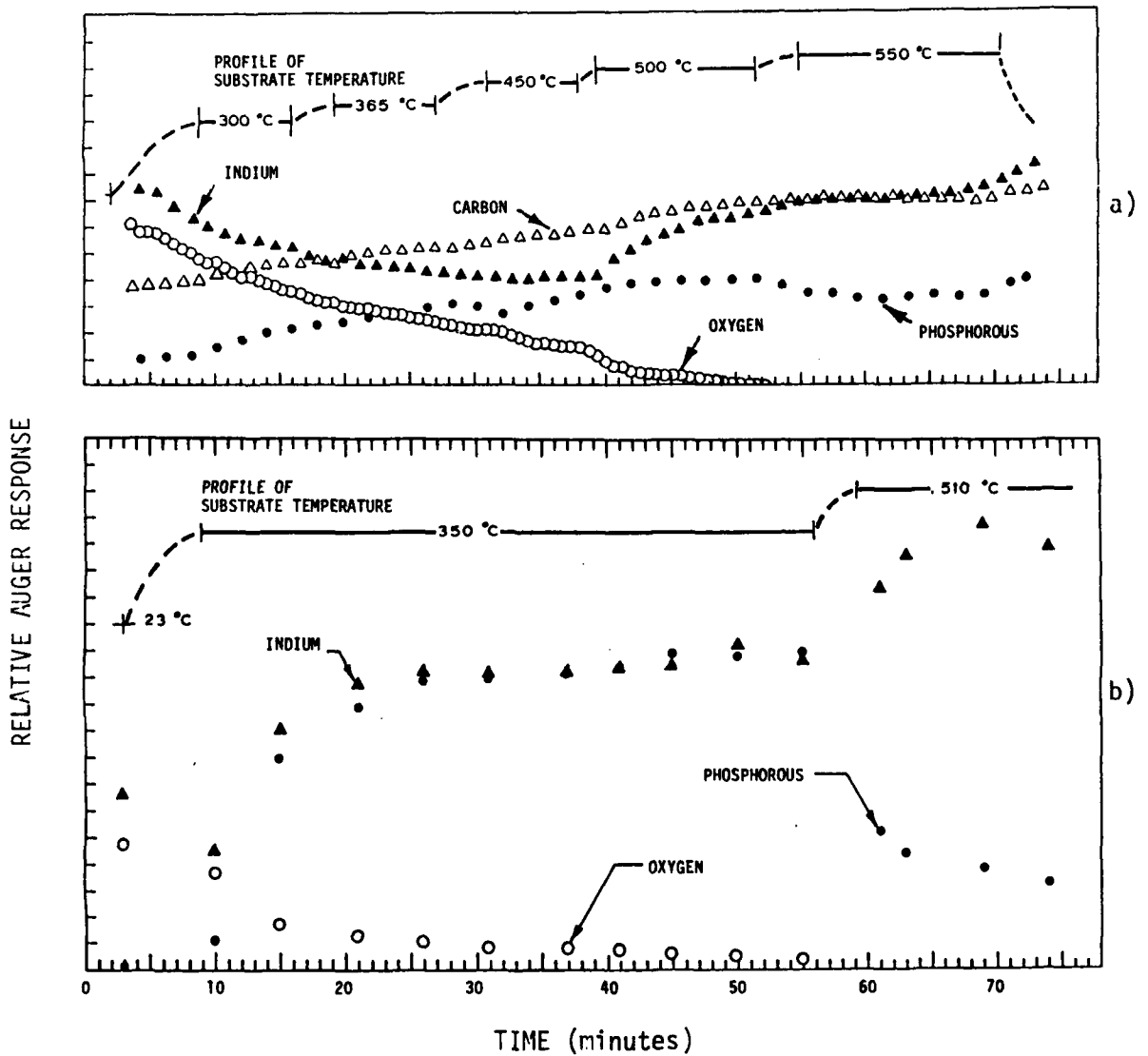


Figure 25. Auger Responses Monitored During the Heating of Passivated InP Substrates Exposed to UHV Overnight (a) and for Three Hours (b).

phosphorous atoms since the oxygen affinity for phosphorous ( $P_2O_3$ ) is slightly higher than the oxygen affinity for indium ( $In_2O_3$ ) [124]. In addition to the oxygen peaks, the initial Auger spectra showed moderate In responses (MNN transition) and very weak P responses (LMM transition). A moderately strong carbon peak was present on the substrate exposed overnight to the UHV ambient of an ion pumped vacuum system\*. As the spectra in Figure 26 indicate, there was no detectable adsorption of C on the surface of the second substrate which was exposed to an UHV ambient for only three hours. Although the data in Figure 25 clearly show that oxygen is desorbing at temperatures on the order of 300 °C, the most rapid desorption occurs for temperatures  $\geq$  500 °C. The low energy phosphorous response increases in magnitude as the oxygen is thermally desorbed.

While the temperature ranges of rapid oxide desorption are similar for InP and GaAs, the congruent temperature for InP is much lower than the value of 657 °C established for GaAs [67]. Congruent processes under Langmuir evaporation conditions exist for (100) InP substrates held at temperatures below approximately 365 °C [68]. Decomposition of (100) InP layers has been reported at temperatures of 420 °C [125]. The present study indicated that macroscopic droplets of molten metal formed in a matter of minutes on InP substrates heated to 550 °C under UHV conditions.

A heating schedule of 45 minutes at a constant temperature of 350 °C produces a substantial increase in the strengths of the P and In Auger

---

\* The gradually increasing strength of the carbon response in Figure 25 is probably an artifact of the experimental technique. The InP surface was continuously irradiated with a 3 keV electron beam during the AES study of the first substrate and this generally enhances the sticking coefficient for residual gaseous contaminants including CO and CO<sub>2</sub>.

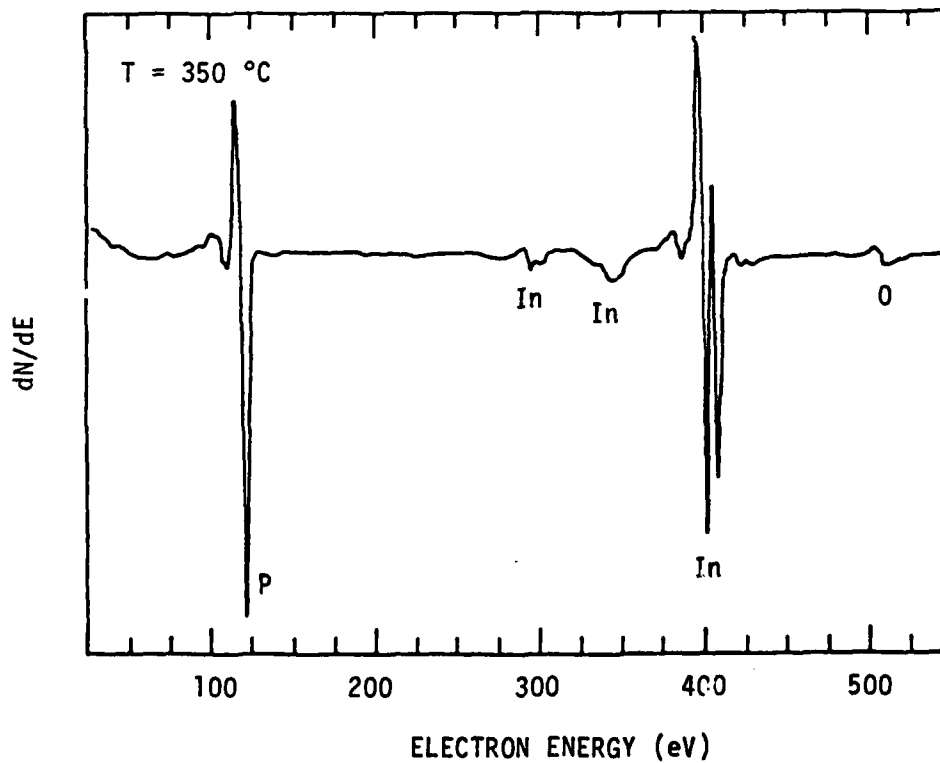
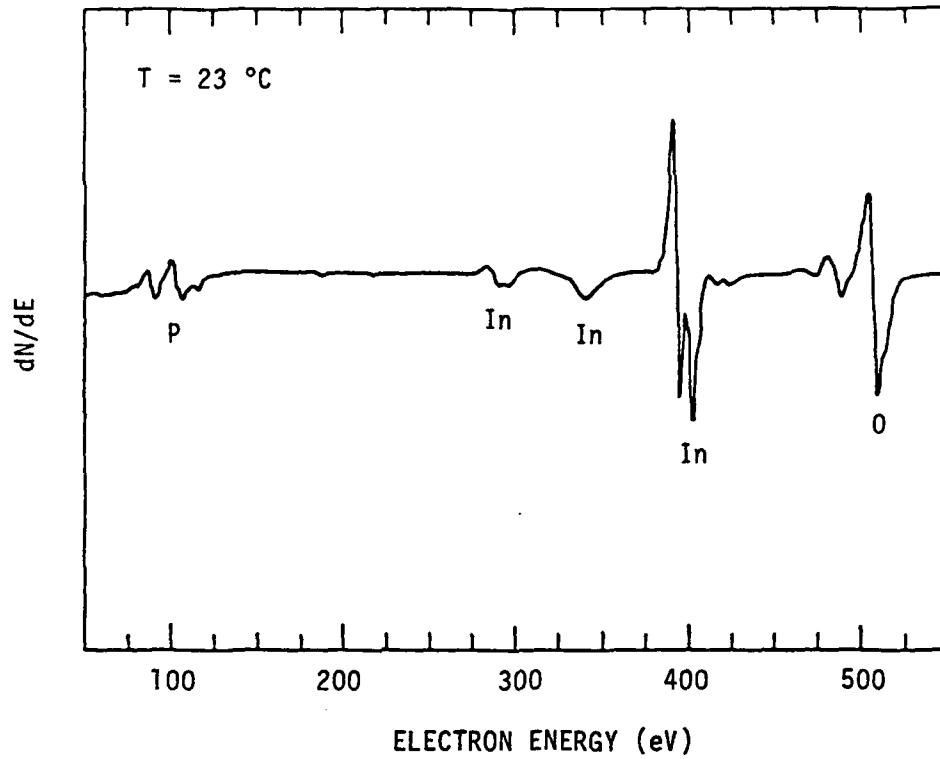


Figure 26. Auger Spectrums of a Passivated InP Substrate Before and After Heating for 45 Minutes at 350 °C.

responses, and the O coverage is reduced to a fraction of a monolayer. Oxygen at this level is desorbed in approximately one minute by raising the substrate temperature to the epilayer growth temperature of 510 °C. Such a schedule of substrate cleaning and heating achieves the goal of providing an uncontaminated InP surface prior to the growth of epitaxial layers.

### 5.1.3 Material Properties

The  $\text{In}_x\text{Ga}_{1-x}\text{As}$  layers were formed from separately heated effusion cells loaded with 6N In (Indium Corporation of America), 6N Ga (Alusuisse), and 6N As (Preussag). The unintentionally-doped layers were deposited on (100) Fe-doped InP substrates obtained from the Royal Signals and Radar Establishment, Malvern, England. Pregrowth processing of the substrates followed the procedure described above in Section 5.1.2. Actual epilayer growth occurred at substrate temperatures of approximately 510 °C. Individual gauge pressures of the In and Ga beams were recorded with a traversing ionization gauge positioned behind the substrate. The control of the In and Ga molecular impingement rates in the present experiments keyed principally on these gauge pressures. Table 6 summarizes the basic deposition parameters and analytical data which characterize the initial layers of  $\text{In}_x\text{Ga}_{1-x}\text{As}$  grown on InP.

The rocking curves in Figure 27 indicate that the halfwidths of the diffraction peaks from the epilayers B0515 and B0525 are significantly broader than the  $K_{\alpha_1}$  and  $K_{\alpha_2}$  lines from the InP substrates. The latter contained a dislocation density of  $3$  to  $7 \times 10^4 \text{ cm}^{-2}$ . High energy reflection electron diffraction patterns (RHEED) for ternary layers B0515 and B0525 are shown in the insets in Figure 27. Epitaxial growth is evident in the spot pattern for B0525. In addition to the isolated high angle

Table 6. Deposition Parameters, Compositions, and Electrical Properties of MBE In<sub>x</sub>Ga<sub>1-x</sub>As Layers Grown Directly on (001) InP Substrates.

Layer	Thickness μm	DEPOSITION PARAMETERS				COMPOSITIONS			ELECTRICAL PROPERTIES*	
		Growth Rate (μm hr <sup>-1</sup> )	T <sub>sub</sub> (°C)	P <sub>In</sub> (Torr)	P <sub>Ga</sub> (Torr)	X <sub>Auger</sub>	X <sub>Microprobe</sub>	X <sub>GaAs Step</sub>	N (cm <sup>-3</sup> )	μ <sub>296</sub> (cm <sup>2</sup> V <sup>-1</sup> sec <sup>-1</sup> )
80525	2.6	1.3	509	1.2 x 10 <sup>-7</sup>	1.0 x 10 <sup>-7</sup>	0.51	0.80	0.54	1.4 x 10 <sup>17</sup>	566.0
80515	2.3	2.3	514	2.1 x 10 <sup>-7</sup>	2.5 x 10 <sup>-7</sup>	0.26	0.45	0.37	1.1 x 10 <sup>15</sup>	121.0
80517	2.3	1.2	510	1.0 x 10 <sup>-7</sup>	1.4 x 10 <sup>-7</sup>	0.20	0.45	0.24	6.2 x 10 <sup>14</sup>	88.8
80518	2.3	1.2	512	0.7 x 10 <sup>-7</sup>	1.5 x 10 <sup>-7</sup>	0.21	0.40	0.30	8.8 x 10 <sup>13</sup>	81.3

\* Uncorrected Hall Data

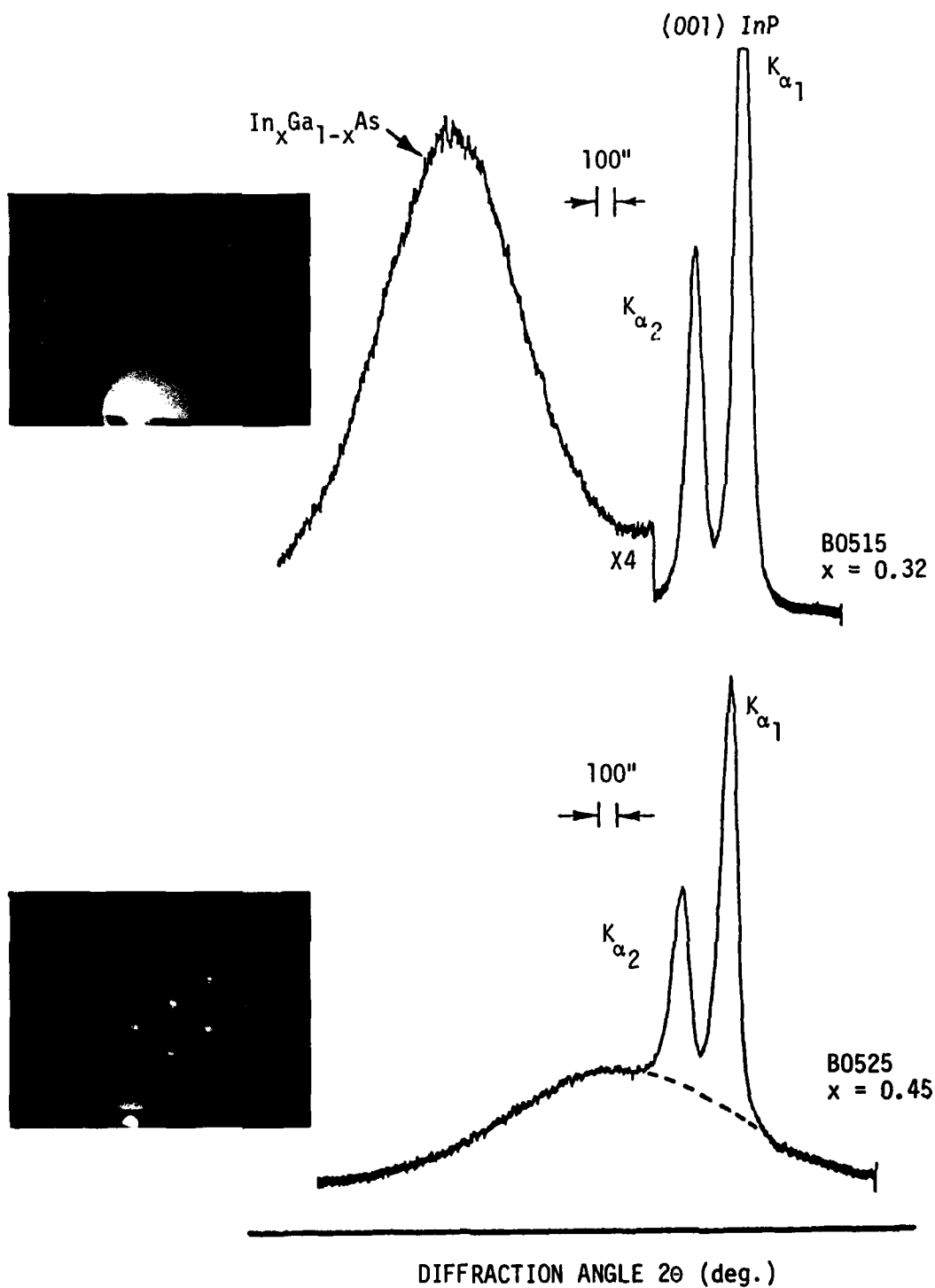


Figure 27. Rocking Curves of MBE  $\text{In}_x\text{Ga}_{1-x}\text{As}$  Layers on InP Substrates ( $\{400\}$   $\text{Cu K}_\alpha$  reflections). Insets Show RHEED Patterns (100 keV,  $[110]$  azimuths) of the  $(001)$  Ternary Surfaces.

spots which characterized layer B0515, the RHEED pattern for the ternary layer with the largest mismatch B0517 ( $\delta = -0.023$ ) also contained Debye Scherrer rings indexed as reflections from {111}, {220}, {113}, and {400} planes.

Some problems have been encountered in determining the compositions for the thin ternary epilayers. An electron microprobe (Acton Laboratories Electron Probe) operating with a 20 keV beam energy should yield concentrations for In and Ga accurate to 0.1 percent. However, the microprobe consistently returned values of  $x$  that were higher than the  $x$  values using the other techniques listed in Table 6. It appears that the probe is sampling some In from the substrate. Better agreement is obtained between compositions determined from quantitative analyses of Auger electron spectra and compositions determined by measuring the height of the GaAs step formed beneath a small shadow clip positioned above the substrate. Details of optical interference patterns of the epilayer growth in the vicinity of the clip are presented in Figure 28. Changes in layer height are expressed in terms of fringe displacements where adjacent fringes are separated by  $\lambda/2 = 2730.5 \text{ \AA}$  for samples illuminated with the mercury green line.

The molecular beam from the In oven was incident from the left hand side of the shadowed area shown in Figure 28 and the molecular beams from the Ga and As ovens fell in a plane normal to the substrate. Thus, the first step nearest the substrate along the right hand edge of the shadowed area received direct illumination from the Ga and As ovens and no direct molecular flux from the In oven. The initial step along the opposite edge was partially shielded from the Ga oven and partially self-masked from the

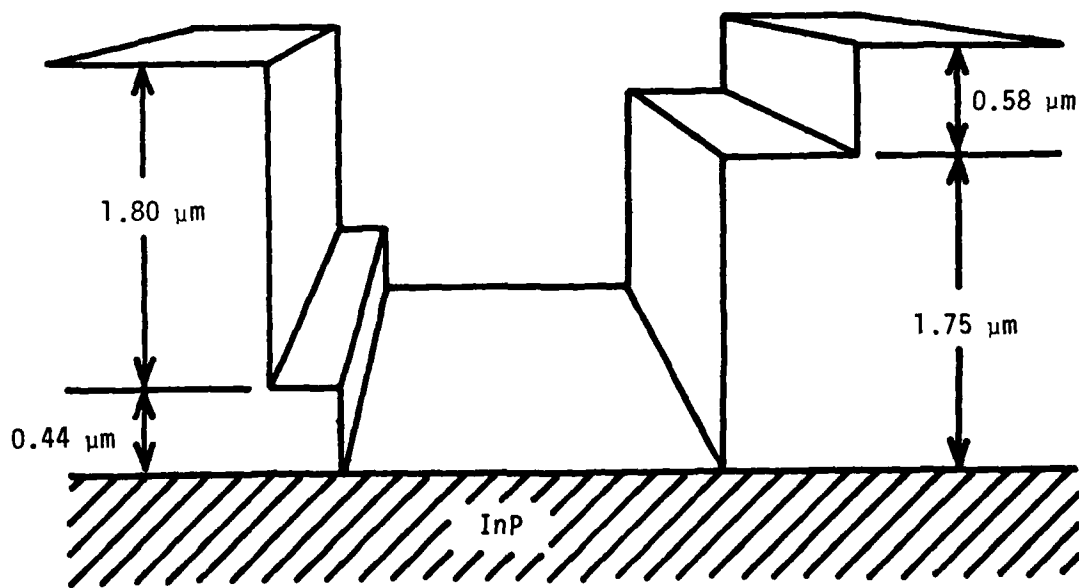
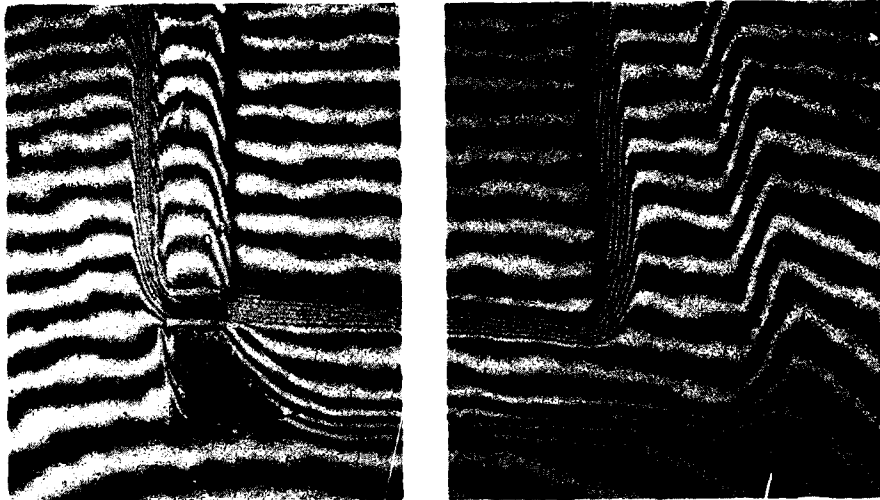


Figure 28. Optical Interference Patterns of the Growth of  $\text{In}_x\text{Ga}_{1-x}\text{As}$  Layer MBE B0517 Near a Shadow Clip.

In molecular beam by the growing  $\text{In}_x\text{Ga}_{1-x}\text{As}$  layer. With a sticking coefficient of unity for both the In and Ga molecular beams, the composition  $x$  is related to the thickness of the GaAs step and the thickness of the  $\text{In}_x\text{Ga}_{1-x}\text{As}$  layer as follows:

$$x \approx \frac{t_{\text{InGaAs}} - t_{\text{GaAs}}}{t_{\text{InGaAs}}} . \quad (14)$$

Further evidence that a lattice match to InP was not achieved in the ternary layers listed in Table 6 was obtained by analyzing the peak positions of the X-ray diffraction lines shown in the rocking curves in Figure 27 for layers B0515 and B0525. The basic technique is outlined in Appendix II. Values of the mole fraction  $x$  for layers B0515 and B0525 are estimated as 0.30 and 0.45, respectively.

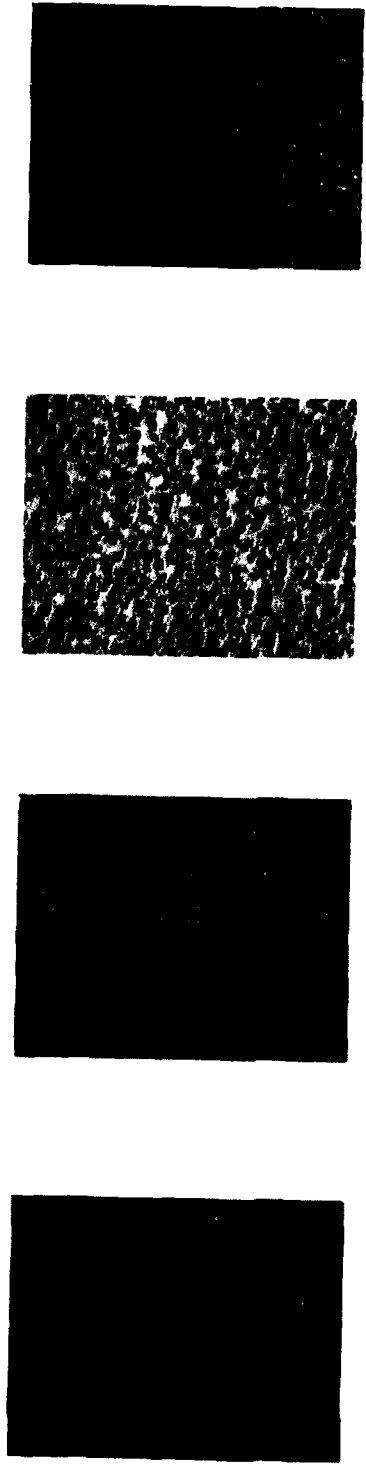
Uncorrected, van der Pauw Hall data for the ternary layers are also shown in Table 6. Evaporated Au(80%)/Sn(20%) pads which were alloyed at 460 °C for 30 seconds gave ohmic contacts for the electrical measurements. The increasing lattice mismatch and onset of polycrystalline growth for layers B0517 and B0518 provide significant compensation of the unintentional donor and reduce Hall mobilities to  $\approx 90 \text{ cm}^2 \text{ V}^{-1} \text{ sec}^{-1}$ . A higher donor concentration was observed for layer B0525 which was more closely matched to the lattice of the InP substrate. The growth conditions and structure have clearly not been optimized for these layers. Room temperature mobilities of  $10^4 \text{ cm}^2 \text{ V}^{-1} \text{ sec}^{-1}$  are more representative for n-type ( $2 \times 10^{17} \text{ cm}^{-3}$ )  $\text{In}_{0.53}\text{Ga}_{0.47}\text{As}$  grown by LPE [126]. A mobility of  $5300 \text{ cm}^2 \text{ V}^{-1} \text{ sec}^{-1}$  was reported at a similar doping level of  $\text{In}_{0.58}\text{Ga}_{0.42}\text{As}$  grown by MBE [62].

## 5.2 GROWTH OF $\text{In}_x\text{Ga}_{1-x}\text{As}$ on GaAs

The deposition of MBE  $\text{In}_x\text{Ga}_{1-x}\text{As}$  layers on GaAs involved keeping the substrate and Ga source temperature constant at 510 °C and 949 °C, respectively. The Ga flux provided a GaAs growth rate of  $0.64 \mu\text{m hr}^{-1}$ . The In source was operated at selected temperatures between 638 °C and 790 °C. The growth occurred under As-stabilized conditions with As flux intensities approximately ten times the Ga and In flux intensities. As In is incorporated in the growing layer, a strain is introduced due to the lattice mismatch between the layer and the (001) GaAs substrate. This has a significant impact on the structural and electrical properties of the deposited layers.

### 5.2.1 Morphology and Composition

Layers grown with low levels of In flux ( $x < 0.15$ ) appear bright shiny to the unaided eye. Under a microscope at 200 X, however, a distinct cross-hatch pattern associated with lattice mismatch strain can be observed. The strain initially increases with the increasing incorporation of In. The optical micrographs of the surfaces of two  $\text{In}_x\text{Ga}_{1-x}\text{As}$  layers shown in Figure 29(a) and 29(b) indicate the degree of enhancement of the cross-hatch pattern. Although both samples appear to be specularly reflecting, a slight haze is noticeable for layer C1031-II. Faint cross-hatch patterns are seen with the optical microscope at even lower In concentrations ( $x \leq 0.05$ ). At In concentrations lying between 20 and 30 percent, the appearance of the surface changes. The cross-hatch pattern disappears and small pits or dimples are formed such as the ones shown for C1029-II in Figure 29(c). The pitting is believed to be caused by the nucleation of In inclusions which relieve the mismatch strain. Further increase in the In flux produces free In metal at the outer surface. Indium droplets can



a) C1101-IIA  
 $\text{In}_{0.12}\text{Ga}_{0.88}\text{As}$

b) C1031-II  
 $\text{In}_{0.18}\text{Ga}_{0.82}\text{As}$

c) C1029-II  
 $\text{In}_{0.30}\text{Ga}_{0.70}\text{As}$

d) C1024-II  
 In on surface

Figure 29. Changes in Surface Morphology of  $\text{In}_x\text{Ga}_{1-x}\text{As}$  Layers Grown on (001) GaAs Substrates with  $0.12 \leq x \leq 0.5$ . Magnification: 200X.

be seen in the bottom half of Figure 29(d). The In was removed from the top half of layer C1024-II by selectively etching the sample in HCl.

From these experiments, it appears that a maximum of 20 to 30 percent In can be incorporated while still maintaining a relatively smooth surface morphology. This limit is probably due to the strain introduced by the larger In atoms. It may also be influenced by the growth rate. A theoretical curve is drawn in Figure 30 which describes the variation in growth rate for  $\text{In}_x\text{Ga}_{1-x}\text{As}$  vs In temperature for a constant flux of Ga molecules of  $3.93 \times 10^{14}$  atoms  $\text{cm}^{-2} \text{sec}^{-1}$  (GaAs growth rate of  $0.64 \mu\text{m hr}^{-1}$ ) emitted from a Ga oven held at  $949^\circ\text{C}$ . The theoretical calculations are based on the Knudsen cell expressions given in Section 2.2.1 (p. 18). It has furthermore been assumed that the sticking coefficients for the Group III elements are unity and that the number of molecules in  $\text{In}_x\text{Ga}_{1-x}\text{As}$  at composition  $x$  can be linearly interpolated from the end point data at  $x = 0$  (GaAs) and  $x = 1.0$  (InAs). Under these conditions, the growth rate  $g$  in  $\mu\text{m hr}^{-1}$  is written as

$$g = 3.6 \times 10^{15} F_{\text{Ga}} (1 + F_{\text{In}}/F_{\text{Ga}})^2 / (2.21 + 1.80 F_{\text{In}}/F_{\text{Ga}}). \quad (15)$$

Experimental values of  $g$  determined from measured layer thicknesses and run durations as a function of the temperatures measured by a thermocouple embedded in the In oven have also been entered in Figure 30. At In source temperatures greater than approximately  $760^\circ\text{C}$ , the experimental points no longer show the anticipated behavior. The observed decrease in growth rate is an indication that part of the In flux is not being incorporated in the layer but exists on the outer surface as free In.

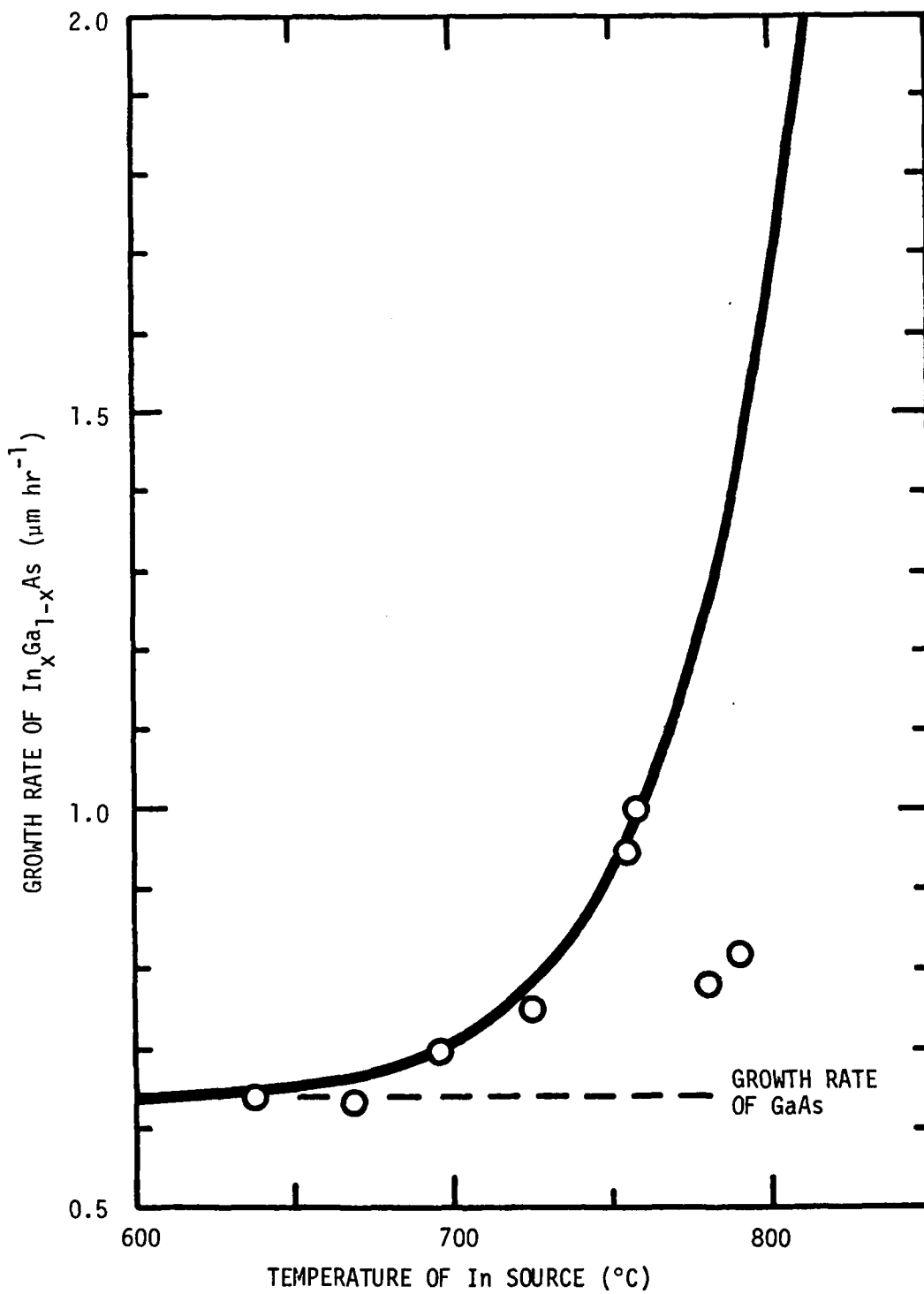


Figure 30. Growth Rate of  $\text{In}_x\text{Ga}_{1-x}\text{As}$  vs In Temperature in the Presence of a Constant Flux of Ga Molecules.

This last observation is, in fact, substantiated by Auger measurements of the composition  $x$  for the  $\text{In}_x\text{Ga}_{1-x}\text{As}$  layers. The composition data given in Figure 31 have been expressed in terms of the pressure measured on the internal ionization gauge mounted just behind the substrate. For  $x \leq 30$  percent the experimentally measured values of  $p_{\text{In}}$  and  $x_{\text{Auger}}$  follow the general behavior of the  $p_{\text{In}}$  vs  $x$  curve computed for a constant  $p_{\text{Ga}}$  of  $2 \times 10^{-7}$  Torr ( $T_{\text{Ga}} = 949$  °C). There is a significant increase in the In Auger signal above this point for layers C1026-II and C1105-II with only a modest increase in the measured In beam pressure. After etching these two layers in HCl to remove free In from the surface, Auger electron spectrometer measurements yielded In compositions of  $0.11 \leq x \leq 0.19$ .

It should be recognized that other possibilities exist for increasing the amount of incorporated In in  $\text{In}_x\text{Ga}_{1-x}\text{As}$  grown on GaAs substrates. These include readjusting the Ga flux to maintain a constant growth rate, changing the substrate temperature, or introducing composition grading in intermediate buffer layers.

### 5.2.2 Electrical Properties

Table 7 presents a summary of the deposition parameters, compositions, and electrical properties of  $\text{In}_x\text{Ga}_{1-x}\text{As}$  layers grown by MBE on GaAs substrates. All of the layers were grown with a constant Ga flux of  $3.9 \times 10^{14}$  atoms  $\text{cm}^{-2}$   $\text{sec}^{-1}$  and a constant As flux of approximately  $5 \times 10^{15}$  atoms  $\text{cm}^{-2}$   $\text{sec}^{-1}$ . The entries in the table have been arranged to show the effects of gradually increasing the intensity of the In molecular beam as the In oven temperature increased from 638 °C to 790 °C. The ionization gauge pressures of the In beam corresponding to In oven operation in this temperature range were  $1 \times 10^{-8}$  Torr to  $3 \times 10^{-7}$  Torr. The oven temperatures listed in Table 7 were roughly 10 to 15 °C lower than the temperature of the

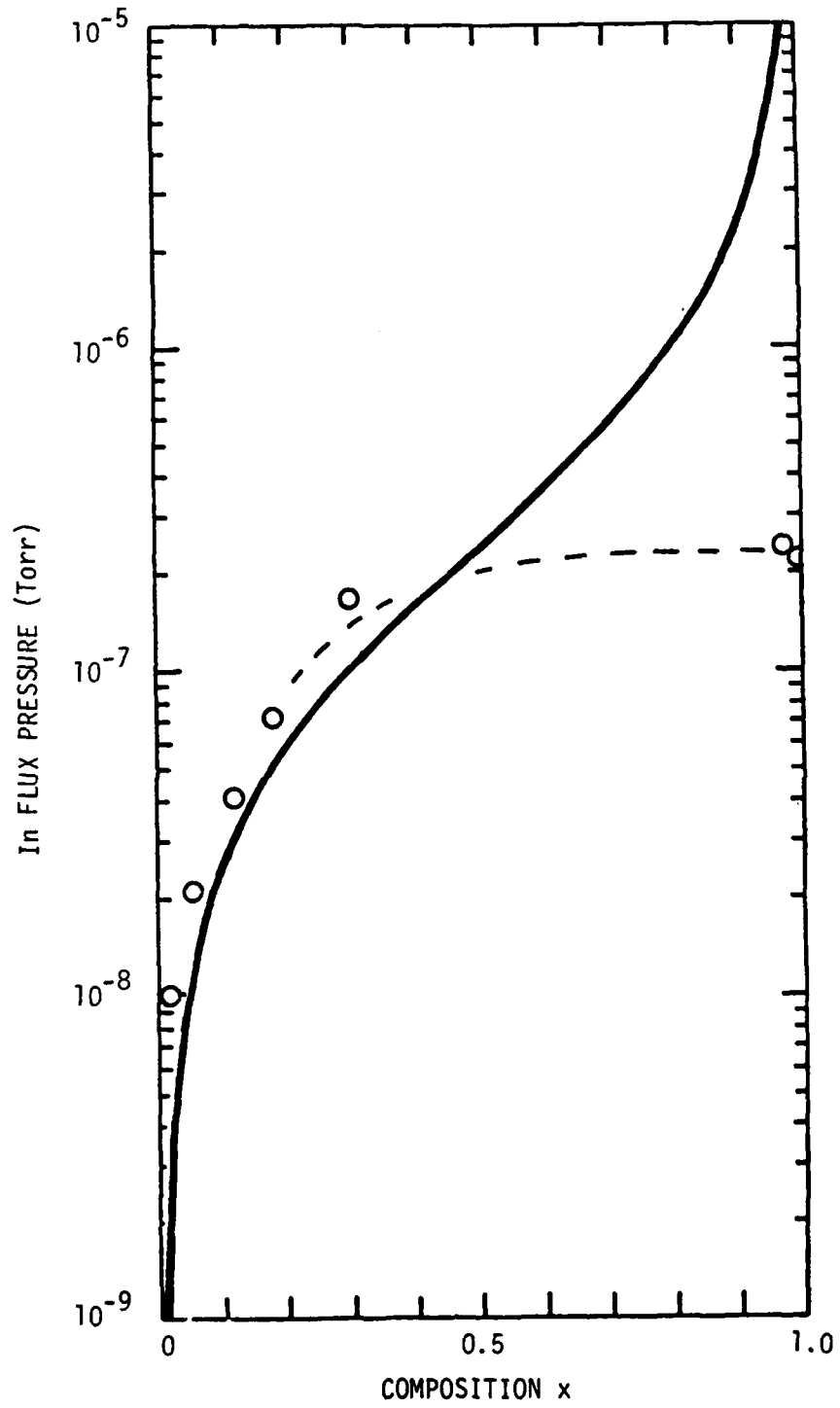


Figure 31. Pressure of In Molecular Beam vs Composition x for  $\text{In}_x\text{Ga}_{1-x}\text{As}$  Grown With a Constant Ga Pressure of  $2 \times 10^{-7}$  Torr

Table 7. Deposition Parameters, Compositions, and Electrical Properties of MBE In<sub>x</sub>Ga<sub>1-x</sub>As Layers Grown Directly on Cr-Doped (001) GaAs Substrates Held at 510 °C

Layer	DEPOSITION PARAMETERS			COMPOSITIONS		ELECTRICAL PROPERTIES		
	Thickness ( $\mu\text{m}$ )	Growth Rate ( $\mu\text{m hr}^{-1}$ )	T <sub>In</sub> (C°)	x <sub>Auger</sub>	x <sub>step height</sub>	Carrier Type	Concentration ( $\text{cm}^{-3}$ )	Mobility at 296 °K ( $\text{cm}^2\text{V}^{-1}\text{sec}^{-1}$ )
C1102-II	1.91	0.64	638	0.016	-	p	$1.8 \times 10^{14}$	84
C1101-IIB	1.89	0.63	674	0.054	-	n	$2.1 \times 10^{13}$	127
C1101-IIA	2.16	0.70	697	0.12	0.09	n	$2.9 \times 10^{15}$	6,266
C1031-II	3.00	0.75	725	0.18	0.15	n	$3.8 \times 10^{15}$	3,826
C1029-II	0.76	0.95	754	0.30	0.33	*	*	*
C1107-II	1.37	1.03	758	0.19	0.30	n	$5.2 \times 10^{13}$	2,660
C1105-II	1.50	0.50	765	(1.00)	-	n	$3.3 \times 10^{16}$	1,283
C1026-II	0.82	0.78	780	(0.97)	0.18	n	$5.8 \times 10^{16}$	460
C1024-II	~1.0	~0.82	790	-	0.22	-	-	-

\* Closely Compensated Sample

load recorded by an optical pyrometer. The change in growth rate and the rejection of In by the lattice for In fluxes greater than  $2 \times 10^{14}$  atoms  $\text{cm}^{-2} \text{sec}^{-1}$  ( $T_{\text{In}} \gtrsim 760$  °C) have been discussed in detail in Section 5.2.1.

The Hall data for the  $\text{In}_x\text{Ga}_{1-x}\text{As}$  layers show two basic features. First, there is an increase in electron concentration as  $x$  increases. Secondly, there is a decrease in carrier mobility for  $x \geq 0.2$  which is associated with increased disorder in the crystalline lattice structure. This effect is particularly noticeable in the layers which are 0.8 to 1.5  $\mu\text{m}$  thick. The donor introduced with  $x = 0.016$  in layer C1102-II provided significant compensation of the residual background acceptor that was identified for GaAs grown in the quaternary MBE system (Section 2.2.3, p. 27). At slightly higher levels of In flux, a residual donor which is commonly observed for unintentionally doped  $\text{In}_x\text{Ga}_{1-x}\text{As}$  dominates the doping of the MBE layers. A peak mobility,  $\mu_{296} = 6266 \text{ cm}^2 \text{ V}^{-1} \text{ sec}^{-1}$ , was measured for layer C1101-IIA ( $\text{In}_{0.12}\text{Ga}_{0.88}\text{As}$ ). This mobility compares favorably with the best mobilities reported by other laboratories for  $\text{In}_x\text{Ga}_{1-x}\text{As}$  grown on GaAs substrates. Representative examples of  $0.11 \leq x \leq 0.24$  are listed in Table 8 [57,64,127-131]. The mobility at 77 °K for C1101-IIA was  $17,400 \text{ cm}^2 \text{ V}^{-1} \text{ sec}^{-1}$ . Values of  $\mu_{77} = 12,400$  and  $14,500 \text{ cm}^2 \text{ V}^{-1} \text{ sec}^{-1}$  were recently reported by Calawa for MBE  $\text{In}_{0.53}\text{Ga}_{0.47}\text{As}$  grown on InP [132]. Further increases in the In flux causes mobilities to decrease and electron concentrations tend to increase. The decline in mobility is consistent with a higher incidence of defects generated by misfit dislocations and strains in the lattice which is partially rejecting the incident In molecules. There is, however, no evidence from RHEED analyses of C1029-II and C1024-II for linking these effects with pronounced polycrystalline growth.

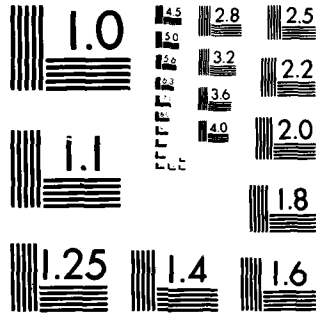
Table 8. Mobilities Reported for  $\text{In}_x\text{Ga}_{1-x}\text{As}$  Layers Grown on GaAs Substrates

Composition, x	Mobility at 300 °K ( $\text{cm}^2\text{V}^{-1}\text{sec}^{-1}$ )	Doping	Growth Technique	Reference
0.11	4,500	U	MBE	64
0.15	3,500	Sn	MBE	57
~0.15	~5,000	U	LPE	127
~0.15	~5,000	U	LPE	128
0.24	570	U	MO	129
0.16	6,050	U	VPE	130
0.15	6,920*	U	VPE	131

\* Compositionally graded buffer layer 3.4  $\mu\text{m}$  thick between substrate and 0.5  $\mu\text{m}$  thick epilayer.

U Unintentionally doped





MICROCOPY RESOLUTION TEST CHART

NATIONAL BUREAU OF STANDARDS-1963-A

Alloy scattering mechanisms [129,133] have also been involked to explain a decrease in mobility for  $\text{In}_x\text{Ga}_{1-x}\text{As}$  layers with compositions  $< 0.2 x < 0.6$ .

## 6.0 INVESTIGATION OF QUATERNARY SEMICONDUCTORS

Quaternary layers of  $\text{In}_{1-x}\text{Ga}_x\text{As}_y\text{P}_{1-y}$  extending over a wide range of composition have been deposited by MBE on (001) GaAs substrates held at 510 °C. Details of the basic growth procedures are presented in Section 6.1. As indicated in Section 6.2, compositions  $x$  and  $y$  for the quaternary layers derived from quantitative analyses of Auger data agree rather closely with the compositions predicted by X-ray rocking curves. The geometric displacement between the four source ovens leads to the growth of binary, ternary, and quaternary alloy semiconductors in regions of the substrate that are partially shadowed from the incident beams. The physical features of growth under these conditions are described in Section 6.3.

### 6.1 GROWTH OF $\text{In}_{1-x}\text{Ga}_x\text{As}_y\text{P}_{1-y}$ LATTICE-MATCHED TO GaAs

The ovens were loaded with 6N Ga (Alusuisse), 6N As (Preussag), 6N In (Indium Corporation of America), and 6N GaP (Alusuisse). Immediately prior to growth the (001) GaAs substrates were heated to 590 °C in an As flux to remove the thin surface oxide layer. Epilayer growth occurred at a substrate temperature of 510 °C. The principal deposition parameters and the resulting layer compositions are listed in Table 9. Intensities of the molecular fluxes impinging upon the substrate were monitored with the quadrupole and ionization gauge mounted in the liquid nitrogen trap assembly that surrounds the growth region. Quaternary growth that was stabilized with the group V elements was achieved with partial pressures of In and Ga of 0.8 to  $1.9 \times 10^{-7}$  Torr and partial pressures of As and P of  $0.6$  to  $1.6 \times 10^{-6}$  Torr.

During the transition periods immediately prior to or following epigrowth, GaAs substrates are commonly exposed to As fluxes of the order of

Table 9. Deposition Parameters and Compositions for MBE  $\text{In}_{1-x}\text{Ga}_x\text{As}_y\text{P}_{1-y}$  Layers Grown on (001) GaAs Substrates Held at 510 °C

Layer	Thickness ( $\mu\text{m}$ )	Growth Rate ( $\mu\text{m hr}^{-1}$ )	$T_{\text{In}}$ ( $^{\circ}\text{C}$ )	$T_{\text{Ga}}$ ( $^{\circ}\text{C}$ )	$T_{\text{As}}$ ( $^{\circ}\text{C}$ )	$T_{\text{P}}$ ( $^{\circ}\text{C}$ )	$x_{\text{Auger}}$	$y_{\text{Auger}}$	Misfit $\Delta a/a$
C1108-II	1.64	0.82	743	915	265	890	0.91	0.22	-0.0213
C1109-II	3.47	0.99	743	915	274	890	0.92	0.12	-0.0256
C1115-II	1.50	0.75	764	888	263	875	0.62	0.36	+0.0049
C1116-II	--	--	764	870	260	875	0.73	0.48	+0.0011
C1121-II	--	--	755	890	260	875	0.76	0.82	+0.0109
C1204-II	1.04	0.52	756	870	256	907	0.60	0.57	+0.0137
C1206-II	1.91	0.64	751	890	255	914	0.86	0.32	-0.0141

Temperatures Monitored by Thermocouples Embedded in Ovens

$10^{15}$  molecules  $\text{cm}^{-2} \text{sec}^{-1}$  whenever the substrate temperature exceeds 350 °C. Therefore, in order to circumvent potential thermal etching of the quaternary layers during the cooldown portion of a growth run,  $\text{As}_4$  and  $\text{P}_2$  fluxes were allowed to impinge upon layers C1108-II, C1109-II, and C1115-II after closing the shutters of the In and Ga ovens. Two to three minutes were required for the substrates to cool to a temperature of 350 °C. At this point, the shutters of the remaining ovens were closed. Since crystalline GaP is presently used for the P source, a limited flux of Ga is present even in the absence of the primary beam from the Ga oven. Thus, the surface stabilization procedure with As and P fluxes left a thin layer of  $\text{GaAs}_y\text{P}_{1-y}$  at the outer surface which almost entirely masked the Auger response of In. A dramatic increase in the percentage of In for layers C1109-II and C1115-II can be observed in Figure 32 as the outer ternary surface is removed by Argon ion bombardment. Only As molecules were subsequently employed in stabilizing the cooling surfaces of quaternary layers.

## 6.2 ANALYSIS OF STRUCTURE AND COMPOSITION

Estimates of compositions for the quaternary layers were obtained from a quantitative analysis of the principal Auger peak-to-peak amplitudes for In, Ga, As, and P. Examples of Auger spectra taken with a primary electron beam energy of 3.0 keV for three MBE quaternary layers are shown in Figure 33. Once the compositions  $x$  and  $y$  have been determined, an approximate value for the misfit  $\delta = (a_0 - a_s)/a_s$  can be derived by using Equation 1 (p. 1) to compute the lattice constant for the epilayer. Using  $a_s = 5.6536 \text{ \AA}$  as the lattice constant for GaAs, the misfits for layers C1206-II, C1116-II, and C1204-II shown in Figure 33 are -0.0141, + 0.0011, and

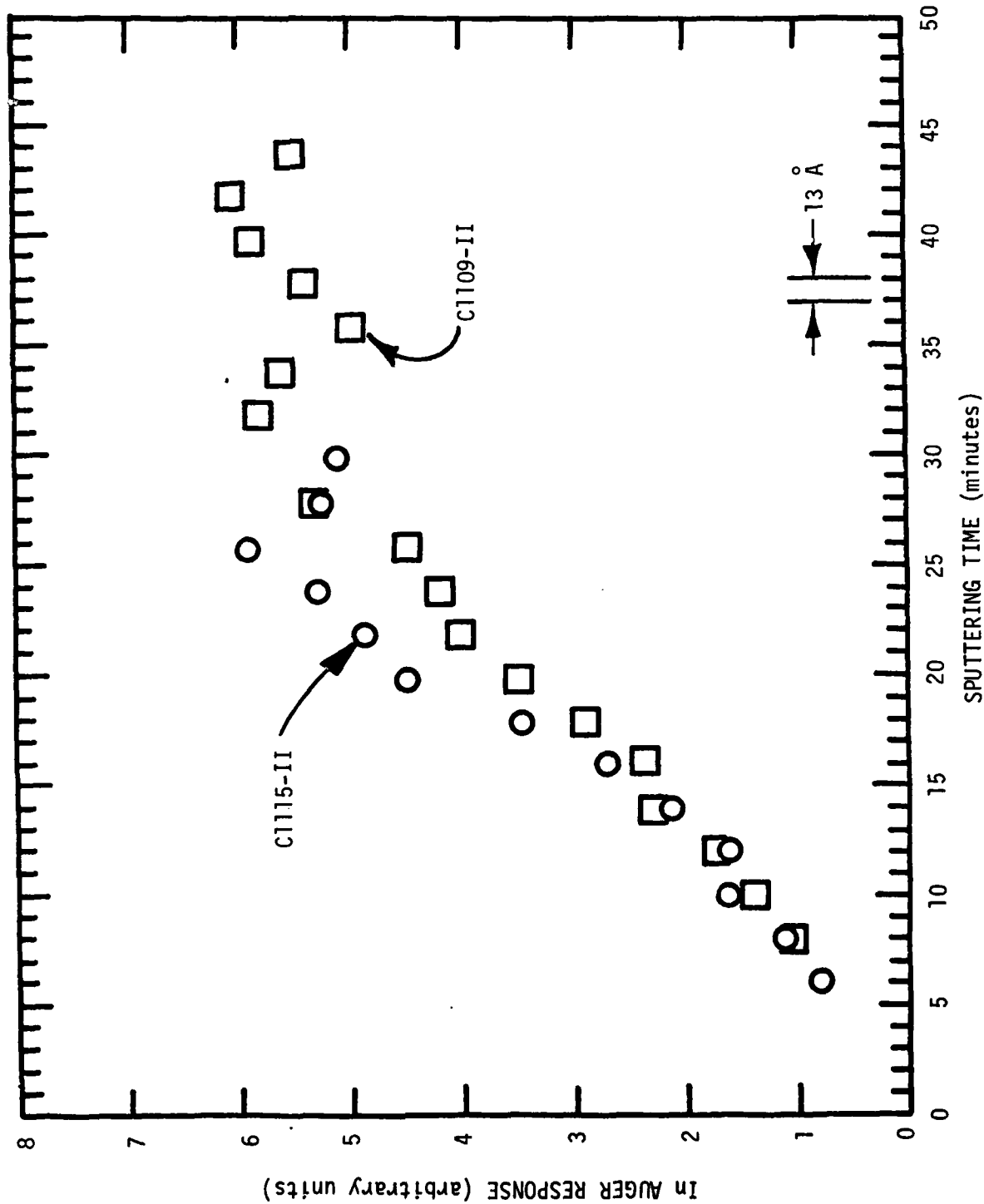


Figure 32. Increase in the In Auger Response for MBE  $\text{In}_{1-x}\text{Ga}_x\text{As}_y\text{P}_{1-y}$  Layers as the Outer  $\text{Ga}_x\text{As}_y\text{P}_{1-y}$  Surface is Removed by Sputtering with 3.0 keV Argon Ions

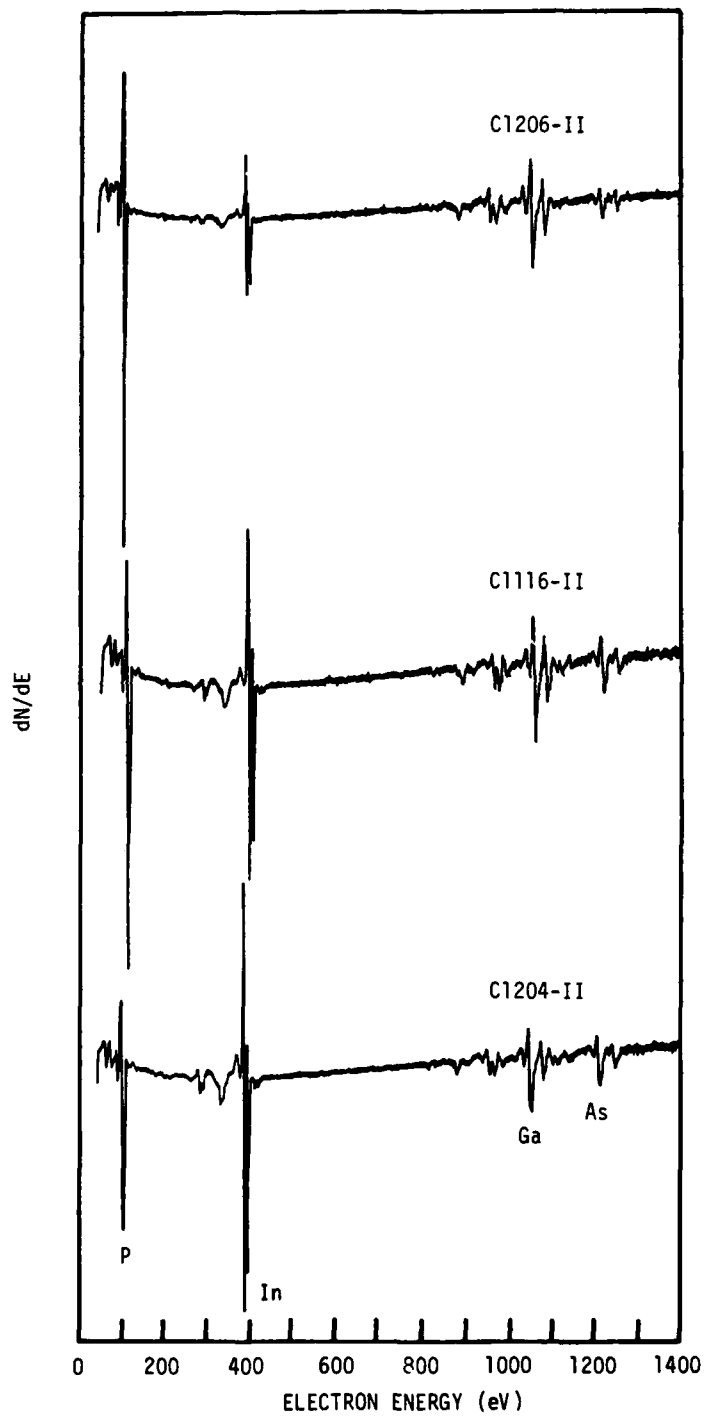


Figure 33. Auger Spectra of  $\text{In}_{1-x}\text{Ga}_x\text{As}_y\text{P}_{1-y}$  Layers Grown by MBE on (001) GaAs. Primary Beam Energy = 3 keV.

+ 0.0137, respectively. Smooth, reflecting surfaces characterized MBE quaternary layers even with misfits of this magnitude.

Composition information was also provided by X-ray diffraction measurements using the procedure outlined in Appendix II. A 50 keV electron beam impinging upon a Cu target provided the source of X-rays. The X-ray beam incident upon the sample was 100  $\mu\text{m}$  wide. No detectable shift could be observed between the position of the diffraction peaks from the substrate and epilayer C1116-II. Figure 34 presents rocking curves for the layers given in Figure 33. In addition to the dominant  $\text{CuK}_{\alpha_1}$  and  $\text{CuK}_{\alpha_2}$  doublet arising from the (400) lattice planes of the GaAs substrate, weak peaks associated with the thin epilayers ( $\leq 2.0 \mu\text{m}$  thick) are also observed. The angular displacements of these peaks lead directly to computed misfit values of -0.010 and +0.015 that agree in sign and relative magnitude with the misfits determined from the Auger results. The broad flat envelope observed in Figure 34 for the sample with the negative misfit is believed to be the convolution of diffraction from regions in the sample with different compositions. This emphasizes the stringent requirements which are placed on the control of the incident molecular flux intensities and/or the potential redistribution of the incorporated species during quaternary growth by molecular beam epitaxy.

High energy reflection electron diffraction studies indicate that heteroepitaxial growth is being achieved for the MBE quaternary layers. The distinct spot patterns given in Figure 35 for 100 keV electron beams oriented along [110] azimuths show that the epilayers have assumed the (001) orientation of the substrates.

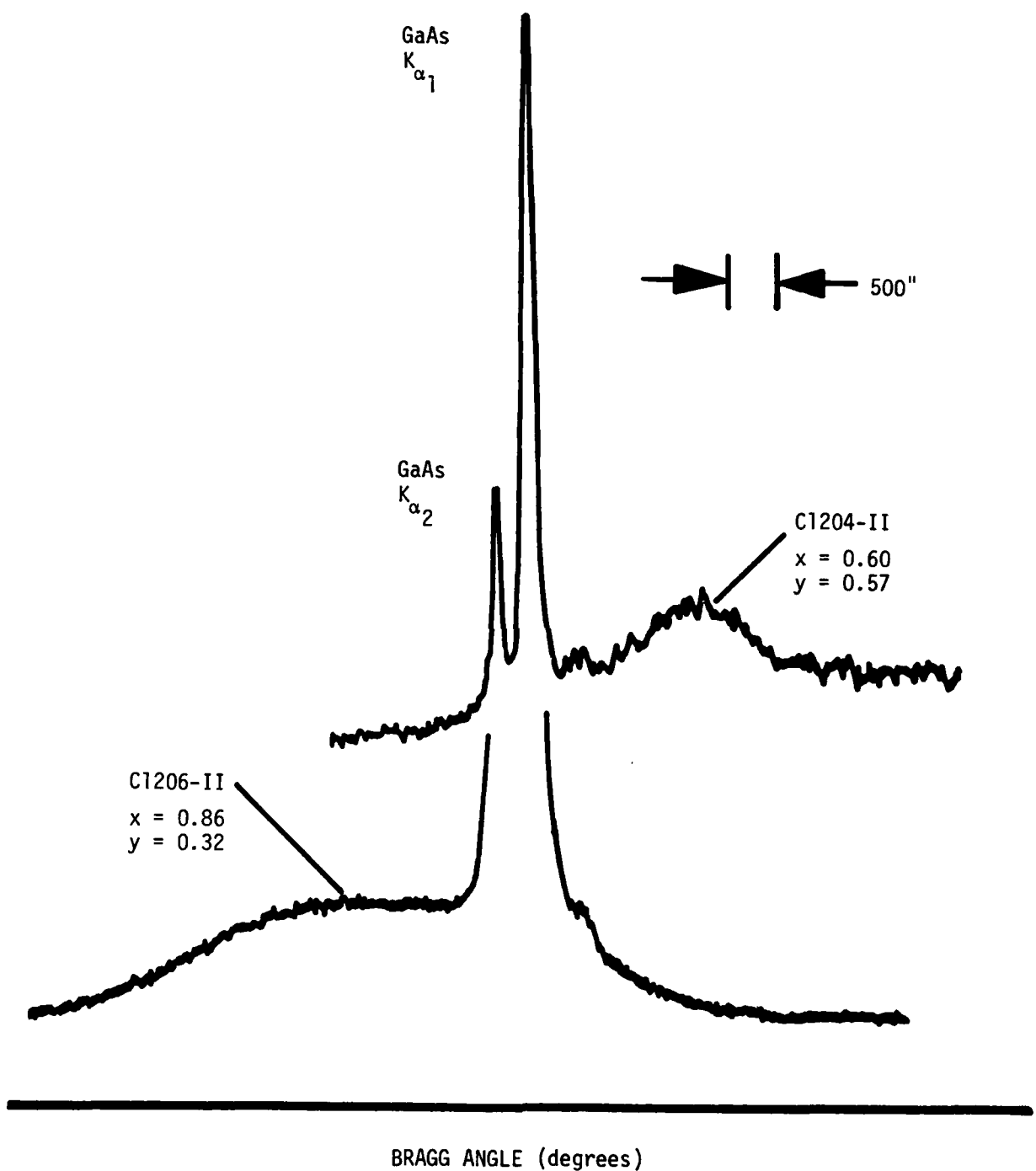
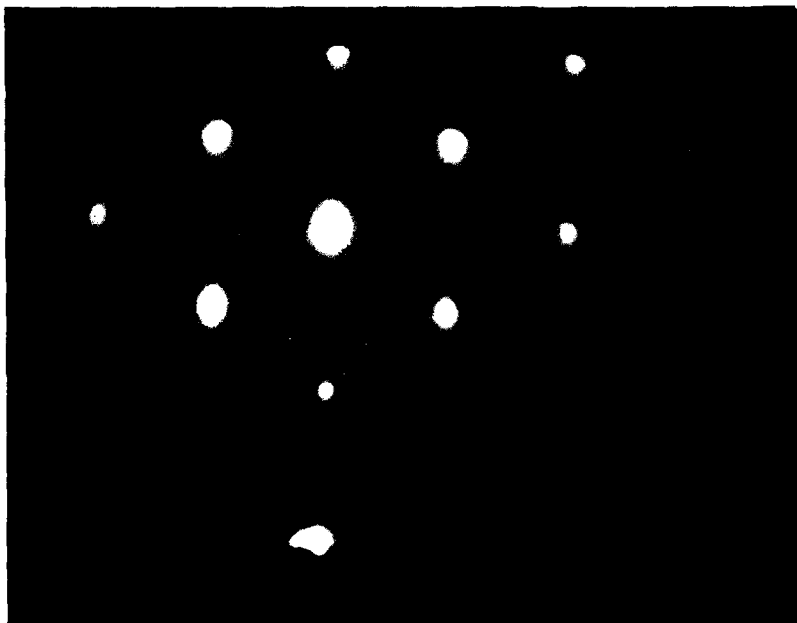
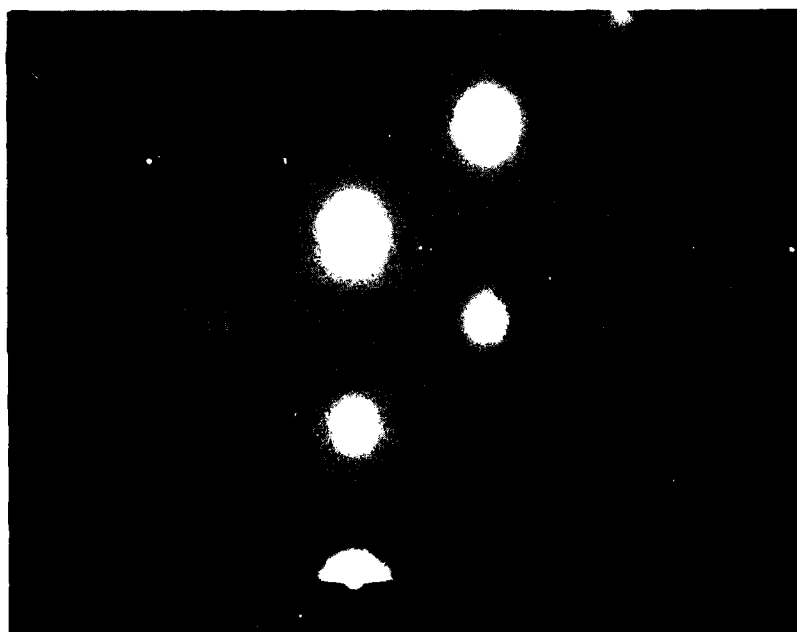


Figure 34. Relative Intensities of (400) Diffraction vs. Bragg Angle for  $In_{1-x}Ga_xAs_yP_{1-y}$  Layers on (001) GaAs.



C1116-II  
x = 0.73  
y = 0.48



C1204-II  
x = 0.60  
y = 0.57

Figure 35. Reflection Electron Diffraction Patterns (100 keV, [110] azimuth) for  $\text{In}_{1-x}\text{Ga}_x\text{As}_y\text{P}_{1-y}$  Layers on (001) GaAs.

Conclusive electrical data have not been obtained for the unintentionally-doped quaternary layers listed in Table 9. Breakdown exceeding 400 volts were measured between two gold-tipped, contact probes on four out of six layers. Layers C1109-II and C1116-II had breakdown voltages of 40 to 60 volts.

### 6.3 PATTERNED GROWTH OF MULTICOMPONENT ALLOYS USING SHADOW MASKING

The internal configuration of the MBE system is such that molecules of each source arrive at the substrate from a different direction. The spatial arrangement of the sources and substrate for the quaternary MBE system is shown in Figure 36. A small mask placed close to the substrate will shield the underlying region and produce patterned growth of multicomponent alloys corresponding to the overlay of separate shadows cast by illuminating the mask from four source positions.

A small Ta ribbon was spot welded to the substrate holder shield and bent to cover a portion of the substrate near one of the vertical edges. A drawing of the source material shadows produced by this shield is shown in Figure 37. The pattern of different alloys expected is also shown. A photograph of this shielded area of the quaternary layer C1109-II grown on a GaAs substrate is shown in Figure 38. Interference fringes trace the difference in elevation of the different areas as in a contour map. The shadow edges outlined in Figure 37 can be identified in the photograph by the abrupt curvature of the interference fringes.

The growth rate of the layers is determined by the flux of column III elements and no significant growth edge should be observed for the As or P shadow if elemental As and P sources are used. A definite growth rate change can be seen in Figure 38 at the P shadow edge. This edge is not due to the P but to Ga which comes from the GaP phosphorous source. The

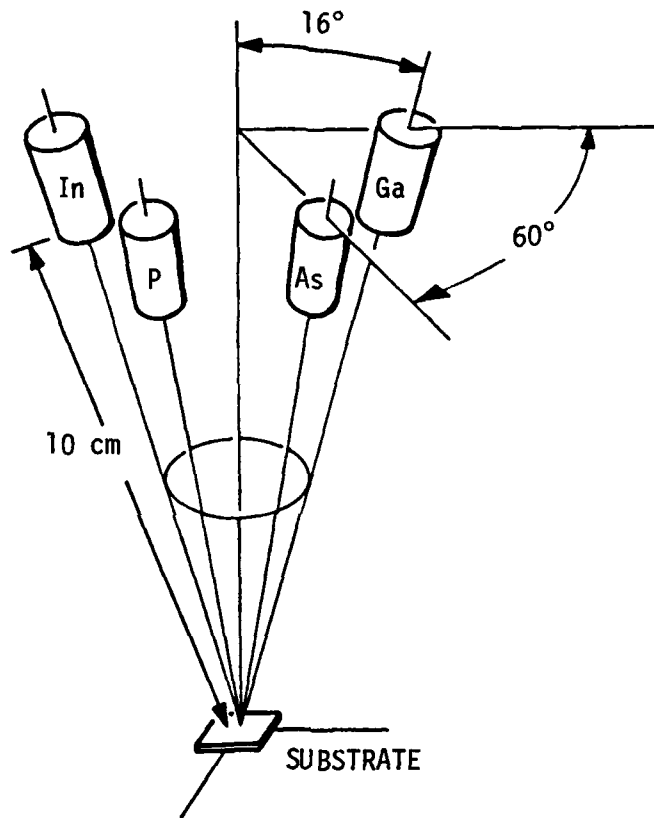


Figure 36. Source-Substrate Geometry in the Quaternary MBE System.

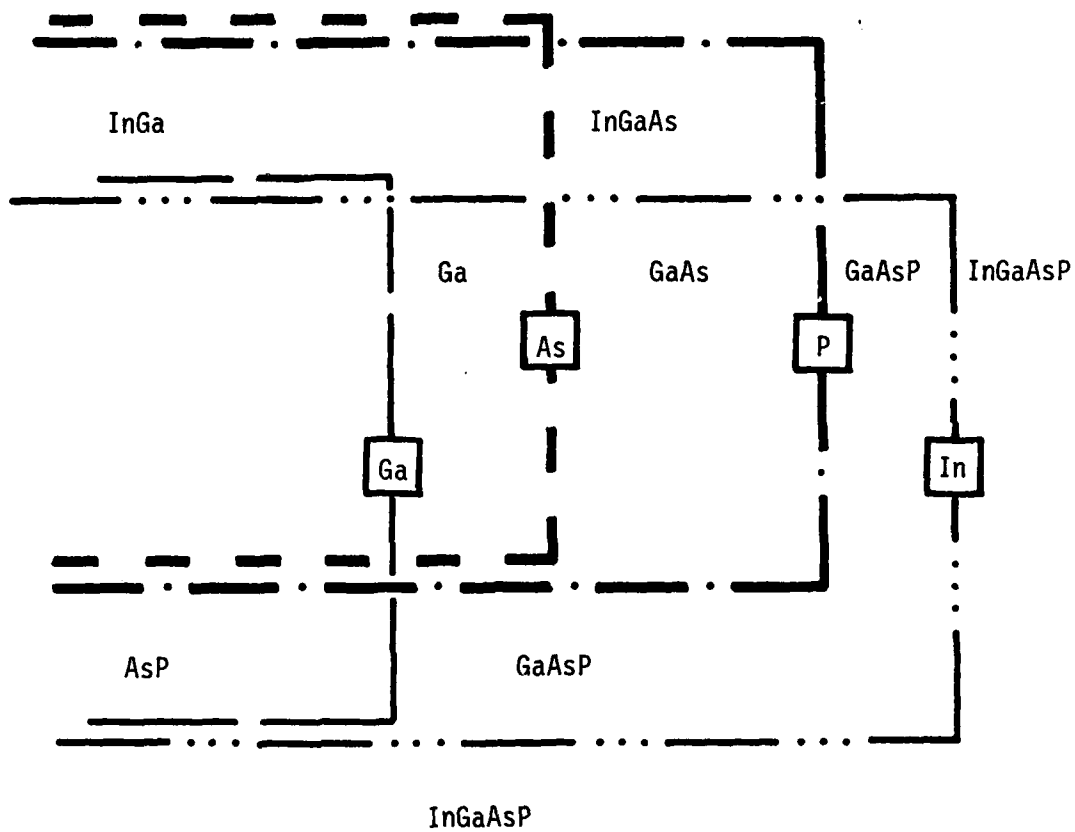
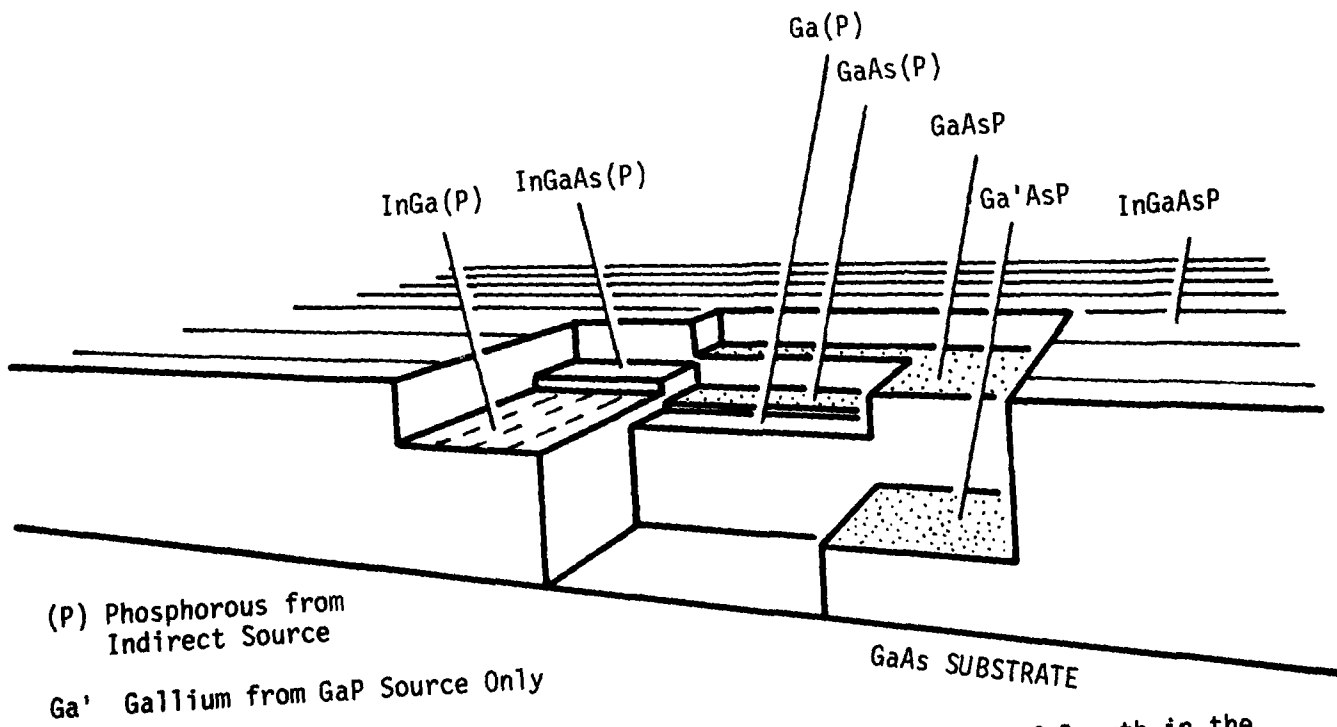
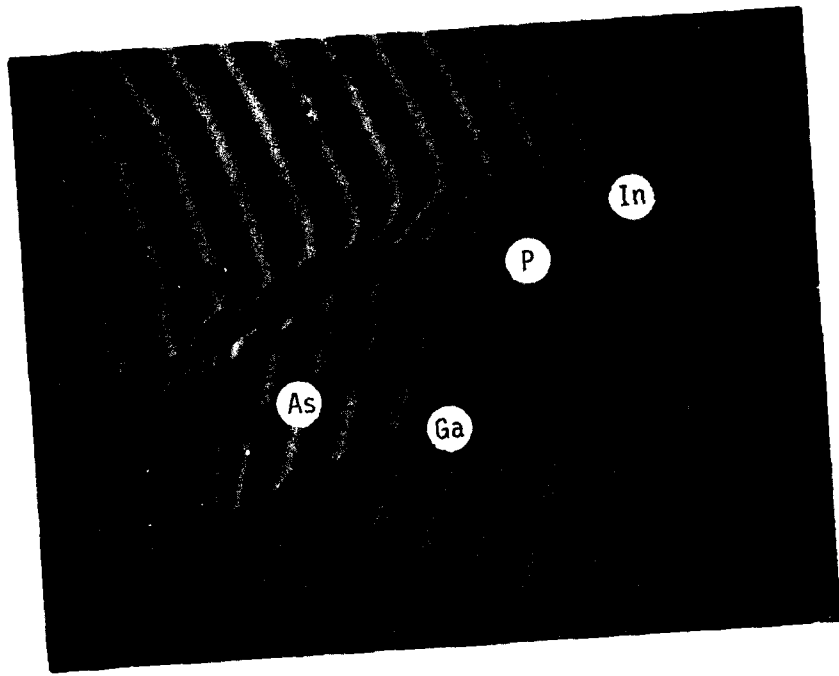


Figure 37. Shadow Pattern Produced by Noncoincident, Molecular Beams of In, Ga, As, and P



(P) Phosphorous from Indirect Source

Ga' Gallium from GaP Source Only

GaAs SUBSTRATE

Figure 38. Micrograph of the Interference Fringe Pattern of Growth in the Shielded Area of Layer C1109-II,  $\text{In}_{0.08}\text{Ga}_{0.92}\text{As}_{0.12}\text{P}_{0.88}$ .

P source acts as a secondary Ga source and the difference in step heights can be used to compare the incorporation of primary and secondary Ga flux. For layer C1109-II shown in Figure 38, 30 percent of the Ga comes from the GaP source.

Figure 37 indicates that there are areas where free Ga or In and Ga would be expected. These areas have frequently been observed on the  $\text{In}_x\text{Ga}_{1-x}\text{As}$  layers (Figure 39) but so far have not been observed when P was present. Thus, the directionality of the P beam is significantly destroyed by intransit collision, by multiple reflections under the shield edges, or by high mobility of the P on the surface of the growing material. There is a high background pressure of As and P in the system during growth and one would expect similar behavior for both fluxes. Arsenic, however, seems to retain a great deal more directionality than P. The dark area shown in Figure 38 is attributed to As masking. Also, a very shallow edge can be seen in Figure 37 where the As shadow edge should be. One explanation of this shallow edge would be that the directionality of the P source is very poor and there is P present over most of the masked area. The edge is caused by the difference in lattice constant of the alloy when As is partially substituted for P at the As shadow edge. The apparent difference in the directionality of the P and As sources may be due to a difference in surface mobility. The As from a pure As source arrives primarily in the form of  $\text{As}_4$  molecules whereas the P from a GaP source is primarily  $\text{P}_2$  molecules.

Micrographs such as Figure 38 were used to establish the thickness of each area of interest in the shadow masked region. The incorporation of Ga and hence the composition  $x$  may be estimated from the ratio of the step

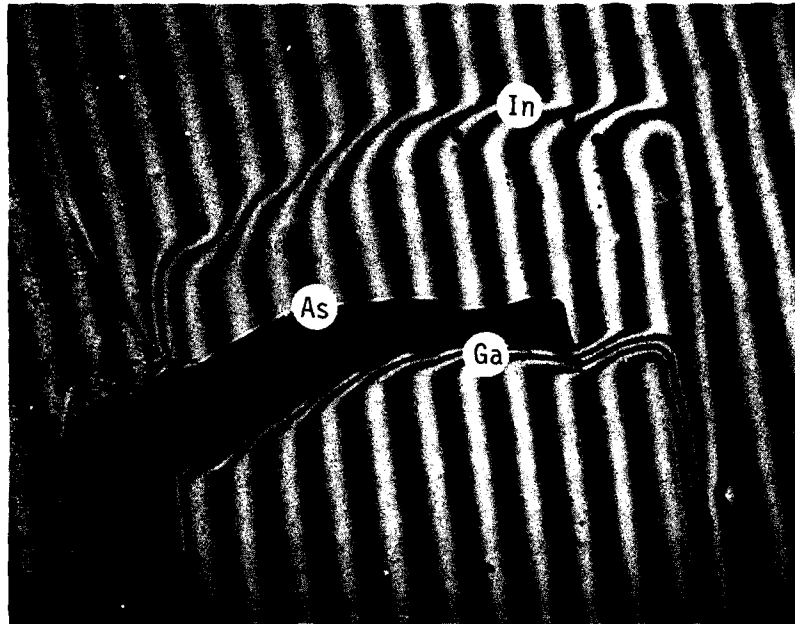


Figure 39. Optical Micrograph of  $\text{In}_x\text{Ga}_{1-x}\text{As}$  Layer C1107-II Showing the Dark As Shadow in Addition to the Ga and In Shadows

height at the In shadow edge and the overall layer thickness. Values of  $x$  computed by the step height technique are compared in Table 10 with composition data derived from Auger analyses.

Table 10. Composition  $x$  in  $\text{In}_{1-x}\text{Ga}_x\text{As}_y\text{P}_{1-y}$  by Step Height and Auger Analyses

Layer	$x_{\text{thickness}}$	$x_{\text{Auger}}$
C1108-II	0.85	0.91
C1109-II	0.86	0.92
C1115-II	0.69	0.62
C1204-II	0.60	0.60
C1206-II	0.71	0.86

## 7.0 FUTURE WORK

Further work is identified in the areas of preparing InP substrates, controlling molecular flux intensities, developing suitable MBE dopants for quaternary layers, and demonstrating the quality of MBE quaternary layers in device structures. The interest in forming  $\text{In}_{1-x}\text{Ga}_x\text{As}_y\text{P}_{1-y}$  with  $x \approx 0.25$  and  $y \approx 0.56$  places particular emphasis on the predeposition treatment of InP substrates. A passivation procedure has been developed which achieves the highly desirable goal of eliminating C without resorting to a sputter etch/thermal anneal sequence. However, electrical data and X-ray rocking curve data for  $\text{In}_x\text{Ga}_{1-x}\text{As}$  films deposited on InP suggest additional work may be needed on substrate preparation. Part of the problem may also involve establishing tighter control of the molecular flux intensities during the growth of alloy semiconductors. The rocking curves for the quaternary lattice-matched to GaAs provide support for this view if there are significant compositional inhomogeneities along the thickness direction. The relationship between deposition parameters and the electrical and optical properties of unintentionally doped quaternary layers should be established. Tin and zinc are the n- and p-type dopants, respectively, that are commonly employed in  $\text{In}_{1-x}\text{Ga}_x\text{As}_y\text{P}_{1-y}$  layers grown by LPE. Since Sn segregates and neutral Zn has a low sticking coefficient in MBE GaAs, neither dopant is particularly attractive for use in MBE  $\text{In}_{1-x}\text{Ga}_x\text{As}_y\text{P}_{1-y}$ , and other alternatives will be investigated. Device structures such as FETs, TEOs, and double heterostructure lasers form useful vehicles for evaluating the quality of intentionally doped quaternary layers and the characteristics of the  $\text{In}_{1-x}\text{Ga}_x\text{As}_y\text{P}_{1-y}/\text{InP}$  heterojunctions formed by MBE.

APPENDIX I. EFFECT OF CARRIER CONCENTRATION, COMPENSATION, AND TEMPERATURE  
UPON THE MOBILITY OF ELECTRONS IN GaAs

The mobility of electrons in GaAs is governed by several scattering mechanisms including polar optical mode scattering, piezoelectric scattering, deformation potential scattering, and ionized impurity scattering. It is assumed for the present discussion that Matthiesen's rule is valid for the various component mobilities:

$$\mu_n^{-1} = \sum_i (\mu_i)^{-1} \quad (\text{A.1})$$

Following Katoda and Sugano [112], these component mobilities ( $\text{cm}^2 \text{V}^{-1} \text{sec}^{-1}$ ) are expressed as:

polar optical mode scattering,

$$\mu_{po} = 5.31 \cdot 10^3 x(z) (e^z - 1) z^{-1/2}, \quad (\text{A.2})$$

where

$$z = \theta/T,$$

$\theta$  = longitudinal optical phonon temp (416 °K for GaAs),

$x(z)$  = a tabulated function from a variational solution of the Boltzmann equation [113],

piezoelectric scattering,

$$\mu_{pe} = 3.16 \cdot 10^5 (300/T)^{1/2}, \quad (\text{A.3})$$

deformation potential scattering,

$$\mu_{dp} = 5.5 \cdot 10^8 T^{-3/2}, \quad (\text{A.4})$$

and ionized impurity scattering [111],

$$\mu_i = \frac{3.28 \cdot 10^{15} (m/m^*)^{1/2} \epsilon_0^2 T^{3/2} (1-\theta_c)}{n[\ln(b+1) - b/(b+1)] (1+\theta_c)}, \quad (\text{A.5})$$

where

$$b = \frac{1.29 \cdot 10^{14} (m^*/m) \epsilon_0 T^2}{n}$$

$m^*/m$  = effective mass ratio

$\epsilon_0$  = dielectric constant,

$\theta_c = N_A^-/N_D^+$ , and

$n = N_D - N_A$ .

Therefore, the level of compensation  $\theta_c$  can be estimated by comparing the measured low temperature mobilities with the low temperature variation in mobility predicted by Equation A.1 (Equation 11, p. 59) where  $\theta_c$  is treated as an adjustable parameter. Experimental data analyzed in this way are displayed in Figure 22 (p. 58).

APPENDIX II. COMPOSITION OF ALLOY SEMICONDUCTORS DETERMINED FROM X-RAY ROCKING CURVES

The technique of determining the composition of heteroepitaxial films of alloy semiconductors using X-ray rocking curves is based on precisely measuring the lattice parameter  $a_f$  of the film by measuring the angular shift between the diffraction peaks of the film and the foreign substrate. Under optimum conditions, angular shifts in X-ray diffraction peaks as small as 10 seconds of arc ( $\Delta a \approx 0.0005 \text{ \AA}$ ) can be observed. A relationship is formed between  $a_f$  and the alloy composition. In the particular case of  $\text{In}_x\text{Ga}_{1-x}\text{As}$  films on InP substrates, it is convenient to employ Vegard's law which predicts that a linear relationship exists between the unit cell volume of the alloy and the composition  $x$ . Since the lattice parameters for GaAs ( $x = 0$ ) and InAs ( $x = 1$ ) are known with high accuracy, the alloy composition is readily defined with a single measurement of  $a_f$ .

The lattice parameter of the film can be expressed in terms of wavelength  $\lambda$ , the lattice parameter of the substrate  $a_s$ , and the difference between the diffraction angle for the film and substrate  $\Delta_{\text{OBS}}$  as follows for a (400) reflection:

$$a_f = \frac{2\lambda}{\sin\{\Delta_{\text{OBS}} + \sin^{-1}(2\lambda/a_s)\}} \quad (\text{A.6})$$

Rocking curves for two MBE  $\text{In}_x\text{Ga}_{1-x}\text{As}$  films deposited on (001) InP substrates are shown in Figure 27 (p. 73). The curves were obtained by monitoring the (400) diffraction of the epilayer and substrate under illumination by  $\text{Cu K}_\alpha$  radiation. The measured shift in the (400) peak of

0.166 degrees for sample B0525 yields a lattice parameter of 5.841 Å and a composition  $x = 0.45$ . The corresponding data for sample B0515 are an angular shift of 0.458 degrees, a lattice parameter of 5.794 Å, and a composition  $x = 0.32$

## REFERENCES

1. A.Y. Cho and J.R. Arthur, "Molecular Beam Epitaxy," Progress in Solid-State Chemistry (J.O. McCaldin and G. Somorjai, eds.) 10, pp. 157-191 (1975).
2. R.E. Nahory, M.A. Pollack, W.D. Johnston, Jr., and R.L. Barnes, "Band Gap Versus Composition and Demonstration of Vegard's Law for  $\text{In}_{1-x}\text{Ga}_x\text{As}_y\text{P}_{1-y}$  Lattice Matched to InP," Appl. Phys. Lett., 33, pp. 659-661 (1978).
3. R.L. Moon, G.A. Antypas, and L.W. James, "Bandgap and Lattice Constant of GaInAsP as a Function of Alloy Composition," J. Electron. Mater., 3, pp. 635-644 (1974).
4. C.J. Nuese, "III-V Alloys for Optoelectronic Applications," J. Electron. Mater., 6, pp. 253-293 (1977).
5. G.A. Antypas and L.Y.L. Shen, "Orientation Dependence of the Incorporation of Ga, As, and Zn During LPE Growth of InGaAsP Alloys," GaAs and Related Compounds (St. Louis), 1976, Inst. Phys. Conf. Ser. No. 33b, London, pp. 96-104 (1977).
6. H. Nagai and Y. Noguchi, "InP-Ga<sub>x</sub>In<sub>1-x</sub>As<sub>y</sub>P<sub>1-y</sub> Double Heterostructure for 1.5  $\mu\text{m}$  Wavelength," Appl Phys. Lett., 32, pp. 234-236 (1978).
7. S. Machida, H. Nagai, and T. Kimura, "Modulation Characteristics of InGaAsP/InP L.E.D.S at 1.5  $\mu\text{m}$  Wavelength," Electron. Lett., 15, pp. 175-177 (1979).
8. P.D. Wright, Y.G. Chai, and G.A. Antypas, "InGaPAs-InP Double-Heterojunction High-Radiance LED's," IEEE Trans. Electron Devices, ED-26, pp. 1220-1227 (1979).
9. J.J. Coleman, N. Holonyak, Jr., R. Chin, B.L. Marshall, W.O. Groves, A.H. Herzog, and D.J. Keune, "Room-Temperature Visible  $\text{In}_{1-x}\text{Ga}_x\text{P}_{1-z}\text{As}_z$  ( $x \leq 1$ ,  $z \sim 0.6$ ) Heterojunction Lasers," Gallium Arsenide and Related Compounds (St. Louis), 1976, Inst. Phys. Conf. Ser., No. 33b, London, pp. 339-345 (1977).
10. P.D. Wright, E.A. Rezek, N. Holonyak, Jr., G.E. Stillman, J.A. Rossi, and W.O. Groves, "Multiple Liquid Phase Epitaxy of  $\text{In}_{1-x}\text{Ga}_x\text{P}_{1-z}\text{As}_z$  Double Heterojunction Lasers: The Problem of Lattice Matching," Appl. Phys. Lett., 31, pp. 40-42 (1977).
11. J.J. Hsieh, "Room Temperature Operation of GaInAsP/InP Double Heterostructure Diode Lasers Emitting at 1.1  $\mu\text{m}$ ," Appl. Phys. Lett., 28, pp. 283-285 (1976).

12. T. Yamamoto, K. Sakai, S. Akiba, and Y. Suematsu, "In<sub>1-x</sub>Ga<sub>x</sub>As<sub>y</sub>P<sub>1-y</sub>/InP DH Lasers Fabricated on InP (100) Substrates," IEEE J. Quant. Electron., QE-14, pp. 95-98 (1978).
13. R.E. Nahory and M.A. Pollack, "Threshold Dependence on Active-Layer Thickness in InGaAsP/InP D. H. Lasers," Electron. Lett., 14, pp. 727-729 (1978).
14. J.J. Coleman, P.W. Foy, R.B. Zetterstrom, S. Sumski, H.C. Casey, Jr., and G.A. Rozgonyi, "Growth and Characterization of InP-Ga<sub>x</sub>In<sub>1-x</sub>P<sub>y</sub>As<sub>1-y</sub> Heterostructure Lasers," GaAs and Related Compounds 1978 (Inst. Phys. Conf. Ser. No. 45) pp. 380-386 (1979).
15. H. Kawanishi, Y. Suematsu, K. Utaka, Y. Itaya and S. Arai, "Ga<sub>x</sub>In<sub>1-x</sub>As<sub>y</sub>P<sub>1-y</sub>/InP Injection Laser Partially Loaded with First-Order Distributed Bragg Reflector," IEEE J. Quantum Electron., QE-15, pp. 701-706 (1979).
16. H.H. Wieder, A.R. Clawson, and G.E. McWilliams, "In<sub>x</sub>Ga<sub>1-x</sub>As<sub>y</sub>P<sub>1-y</sub>/InP Heterojunction Photodiodes," Appl. Phys. Lett., 31, pp. 468-470 (1977).
17. A.R. Clawson, W.Y. Lum, G.E. McWilliams, and H.H. Wieder, "Quaternary Alloy In<sub>x</sub>Ga<sub>1-x</sub>As<sub>y</sub>P<sub>1-y</sub>/InP Photodetectors," Appl. Phys. Lett., 32, pp. 549-551 (1978).
18. C.E. Hurwitz and J.J. Hsieh, "GaInAsP/InP Photodiodes," Appl. Phys. Lett., 32, pp. 487-489 (1978).
19. M.A. Washington, R.E. Nahory, M.A. Pollack, and E.D. Beebe, "High-Efficiency In<sub>1-x</sub>Ga<sub>x</sub>As<sub>y</sub>P<sub>1-y</sub>/InP Photodetectors with Selective Wavelength Response Between 0.9 and 1.7 μm," Appl. Phys. Lett., 33, pp. 854-856 (1978).
20. J.A. Copeland, A.G. Dentai, and T.P. Lee, "p-n-p-n Optical Detectors and Light-Emitting Diodes," IEEE J. Quantum Electron., QE-14, pp. 810-813 (1978).
21. T.P. Lee, C.A. Burrus, Jr., and A.G. Dentai, "InGaAsP/InP Photodiodes: Microplasma-Limited Avalanche Multiplication at 1 - 1.3 μm Wavelength," IEEE J. Quantum Electron., QE-15, pp. 30-35 (1979).
22. H.D. Law, K. Nakano, and L.R. Tomasetta, "III-V Alloy Heterostructure High Speed Avalanche Photodiodes," IEEE J. Quantum. Electron., QE-15, pp. 549-558 (1979).
23. S. Sakai, M. Umeno, T. Aoki, M. Tobe and Y. Amemiya, "InGaAsP/InP Photodiodes Antireflectively Coated with InP Native Oxide," IEEE J. Quantum Electron., QE-15, pp. 1077-1078 (1979).

24. K. Nishida, K. Taguchi, and Y. Matsumoto, "InGaAsP Heterostructure Avalanche Photodiodes with High Avalanche Gain," Appl. Phys. Lett., **35**, pp. 251-253 (1979).
25. M.A. Littlejohn, J.R. Hauser, and T.H. Glisson, "Velocity-Field Characteristics of  $\text{Ga}_{1-x}\text{In}_x\text{P}_{1-y}\text{As}_y$  Quaternary Alloys," Appl. Phys. Lett., **30**, pp. 242-244 (1977).
26. M.A. Littlejohn, J.R. Hauser, T.H. Glisson, D.K. Ferry and J.W. Harrison, "Alloy Scattering and High Field Transport in Ternary and Quaternary III-V Semiconductors," Solid-State Electron., **21**, pp. 107-114 (1978).
27. H. Morkoc, S.G. Bandy, G.A. Antypas, and R. Sankaran, "Submicrometre  $\text{Al}_{0.5}\text{Ga}_{0.5}\text{As}$  Heterojunction Gate GaAs F.E.T.," Electron. Lett., **13**, pp. 487-488 (1977).
28. R.E. Hayes and R.M. Raymond, "Observation of the Transferred-Electron Effect in  $\text{Ga}_x\text{In}_{1-x}\text{As}_y\text{P}_{1-y}$ ," Appl. Phys. Lett., **31**, pp. 300-301 (1977).
29. H. Morkoc, J.T. Andrews, Y.M. Houg, R. Sankaran, S.G. Bandy and G.A. Antypas, "Microwave  $\text{In}_{1-x}\text{Ga}_x\text{As}_y\text{P}_{1-y}$ /InP FET," Electron. Lett., **14**, pp. 448-449 (1978).
30. P.D. Greene, S.A. Wheeler, A.R. Adams, A.N. El-Sabbahy, and C.N. Ahmad, "Background Carrier Concentration and Electron Mobility in LPE  $\text{In}_{1-x}\text{Ga}_x\text{As}_y\text{P}_{1-y}$  Layers," Appl. Phys. Lett., **35**, pp. 78-80 (1979).
31. J.E. Davey and T. Pankey, "Epitaxial GaAs Films Deposited by Vacuum Evaporation," J. Appl. Phys., **39**, pp. 1941-1948 (1968).
32. A.Y. Cho, "Morphology of Epitaxial Growth in GaAs by a Molecular Beam Method: The Observation of Surface Structures," J. Appl. Phys., **41**, pp. 2780-2786 (1970).
33. L.L. Chang, L. Esaki, W.E. Howard, R. Ludeke and G. Schul, "Structures Grown by Molecular Beam Epitaxy," J. Vac. Sci. Technol., **10**, pp. 655-662 (1973).
34. R.F.C. Farrow, "Growth of Indium Phosphide Films from In and P<sub>2</sub> Beams in Ultra-High Vacuum," J. Phys. D: Appl. Phys., **7**, pp. L121-L124 (1974).
35. J.H. McFee, B.I. Miller, and K.J. Bachmann, "Molecular Beam Epitaxial Growth of InP," J. Electrochem. Soc., **124**, pp. 259-272 (1977).
36. Y. Kawamura, M. Ikeda, H. Asahi and H. Okamoto, "Photoluminescence of Undoped (100) InP Homoepitaxial Films Grown by Molecular Beam Epitaxy," Appl. Phys. Lett., **35**, pp. 481-484 (1979).
37. M.T. Norris and C.R. Stanley, "Substrate Temperature Limits for Epitaxy of InP by MBE," Appl. Phys. Lett., **35**, pp. 617-620 (1979).

38. J.E. Davey and T. Pankey, "Structural and Optical Evaluation of Vacuum Deposited GaP Films," J. Appl. Phys., 40, pp. 212-219 (1969).
39. J.R. Arthur and J.J. LePore, "GaAs, GaP, and GaAs<sub>x</sub>P<sub>1-x</sub> Epitaxial Films Grown by Molecular Beam Deposition," J. Vac. Sci. Technol., 6, pp. 545-548 (1969).
40. M. Naganuma and K. Takahashi, "GaAs, GaP and GaAs<sub>1-x</sub>P<sub>x</sub> Films Deposited by Molecular Beam Epitaxy," phys. status solidi (a), 31, pp. 187-200 (1975).
41. M. Naganuma and K. Takahashi, "GaAs, GaP and GaAs<sub>1-x</sub>P<sub>x</sub> Films Deposited by Molecular Beam Epitaxy," Thin Solid Films, 32, p. 42 (1976).
42. Shun-ichi Gonda, Y. Matsushima, S. Mukai, Y. Makita, and O. Igarashi, "Heteroepitaxial Growth of GaP on Silicon by Molecular Beam Epitaxy," Jpn. J. Appl. Phys., 17, pp. 1043-1048 (1978).
43. M. Yano, M. Nogami, Y. Matsushima, and M. Kimata, "Molecular Beam Epitaxial Growth of InAs," Jpn. J. Appl. Phys., 16, pp. 2131-2137 (1977).
44. B.T. Meggitt, E.H.C. Parker, and R.M. King, "Thin InAs Epitaxial Layers Grown on (001) GaAs Substrates by Molecular Beam Deposition," Appl. Phys. Lett., 33, pp. 528-530 (1978).
45. S. Baba, H. Horita, and A. Kinbara, "Synthesis of Stoichiometric InSb Thin Films by a Simple Molecular Beam Technique," J. Appl. Phys., 49, pp. 3632-3633 (1978).
46. L. Esaki and L.L. Chang, "Semiconductor Superfine Structures of Computer-Controlled Molecular Beam Epitaxy," Thin Solid Films, 36, pp. 285-298 (1976).
47. A.Y. Cho and M.B. Panish, "Magnesium-Doped GaAs and Al<sub>x</sub>Ga<sub>1-x</sub>As by Molecular Beam Epitaxy," J. Appl. Phys., 43, pp. 5118-5123 (1972).
48. M. Ilegems, "Beryllium Doping and Diffusion in Molecular-Beam Epitaxy of GaAs and Al<sub>x</sub>Ga<sub>1-x</sub>As," J. Appl. Phys., 48, pp. 1278-1287 (1977).
49. L. Esaki, "Computer-Controlled Molecular Beam Epitaxy," Jpn. J. Appl. Phys., Suppl. 2, Pt. 1, pp. 821-828 (1974).
50. H.C. Casey, Jr., A.Y. Cho, and P.A. Barnes, "Application of Molecular-Beam Epitaxial Layers to Heterostructure Lasers," IEEE J. Quantum Electron., QE-11, pp. 467-470 (1975).
51. K. Ploog and A. Fischer, "In Situ Characterization of MBE Grown GaAs and Al<sub>x</sub>Ga<sub>1-x</sub>As Films Using RHEED, SIMS and AES Techniques," Appl. Phys. 13, pp. 111-121 (1977).

52. N. Matsunaga and K. Takahashi, "Graded Band-Gap  $pAl_xGa_{1-x}As-nGaAs$  Heterojunction Solar Cells Prepared by Molecular Beam Epitaxy," Int. J. Electron., 45, pp. 273-282 (1978).
53. Shun-ichi Gonda and Y. Matsushima, "Effect of Substrate Temperature on Composition Ratio  $x$  in Molecular-Beam Epitaxial  $GaAs_{1-x}P_x$ ," J. Appl. Phys., 47, pp. 4198-4200 (1976).
54. K. Tateishi, M. Naganuma, and K. Takahashi, "Molecular Beam Epitaxial GaP, Ga(AsP)," Electrical Engineering in Japan, 95, pp. 181-186 (1975).
55. K. Tateishi, M. Naganuma, and K. Takahashi, "Graded-Bandgap III-V Ternary Compound Films by Molecular Beam Epitaxy," Jpn. J. Appl. Phys., 15, pp. 785-789 (1976).
56. H. Sakaki, L.L. Chang, R. Ludeke, Chin-An Chang, G.A. Sai-Halasz, and L. Esaki, " $In_{1-x}Ga_xAs-GaSb_{1-y}As_y$  Heterojunctions by Molecular Beam Epitaxy," Appl. Phys. Lett., 31, pp. 211-213 (1977).
57. Chin-An Chang, R. Ludeke, L.L. Chang and L. Esaki, "Molecular-Beam Epitaxy (MBE) of  $In_{1-x}Ga_xAs$  and  $GaSb_{1-y}As_y$ ," Appl. Phys. Lett., 31, pp. 759-761 (1977).
58. A.Y. Cho, H.C. Casey, Jr. and P.W. Foy, "Back-Surface Emitting  $GaAs_xSb_{1-x}$  LEDs ( $\lambda = 1.0\mu m$ ) Prepared by Molecular-Beam Epitaxy," Appl. Phys. Lett., 30, pp. 397-399 (1977).
59. T. Waho, S. Ogawa and S. Maruyama, " $GaAs_{1-x}Sb_x$  ( $0.3 < x < 0.9$ ) Grown by Molecular Beam Epitaxy," Jpn. J. Appl. Phys., 16, pp. 1875-1876 (1977).
60. Chin-An Chang and A. Segmuller, "Substrate Effect on the Lattice Constants of the MBE-Grown  $In_{1-x}Ga_xAs$  and  $GaSb_{1-y}As_y$ ," J. Vac. Sci. Technol., 16, pp. 285-286 (1979).
61. C.T. Foxon and B.A. Joyce, "Surface Processes Controlling the Growth of  $Ga_xIn_{1-x}As$  and  $Ga_xIn_{1-x}P$  Alloy Films by MBE," J. Crystal Growth, 44, pp. 75-83 (1978).
62. B.I. Miller and J.H. McFee, "Growth of  $Ga_yIn_{1-y}As/InP$  Heterostructures by Molecular Beam Epitaxy," J. Electrochem. Soc., 125, pp. 1310-1320 (1978).
63. B.I. Miller, J.H. McFee, R.J. Martin, and P.K. Tien, "Room-Temperature Operation of Lattice-Matched  $InP/Ga_{0.47}In_{0.53}As/InP$  Double Hetero-structure Lasers Grown by MBE," Appl. Phys. Lett., 33, pp. 44-47 (1978).

64. S. Hiyamizu, T. Fujii, K. Nanbu, and S. Maekawa, "Properties of Hetero-epitaxial  $\text{In}_x\text{Ga}_{1-x}\text{As}$  by Molecular Beam Epitaxy," Jpn. J. Appl. Phys., 17, pp. 79-85 (1978).
65. A.Y. Cho, "Recent Developments in Molecular Beam Epitaxy (MBE)," J. Vac. Sci. Technol., 16, pp. 275-284 (1979).
66. B.A. Joyce and C.T. Foxon, "Growth and Doping Kinetics of Molecular Beam Epitaxy," Japan. J. of Appl. Phys., 16, Supplement 16-1, pp. 17-23 (1977).
67. C.T. Foxon, J.A. Harvey, and B.A. Joyce, "The Evaporation of GaAs Under Equilibrium and non Equilibrium Conditions Using a Modulated Beam Technique," J. Phys. Chem. Solids, 34, pp. 1693-1701 (1973).
68. R.F.C. Farrow, "The Evaporation of InP Under Knudsen (equilibrium) and Langmuir (free) Evaporation Conditions," J. Phys. D., 7, pp. 2436-2448 (1974).
69. W.T. Tsang and M. Ilegems, "Selective Area Growth of GaAs/ $\text{Al}_x\text{Ga}_{1-x}\text{As}$  Multilayer Structures with Molecular Beam Epitaxy Using Si Shadow Masks," Appl. Phys. Lett., 31, pp. 301-304 (1977).
70. W.T. Tsang and M. Ilegems, "The Preparation of GaAs Thin-Film Optical Components by Molecular Beam Epitaxy Using Si Shadow Masking Technique," Appl. Phys. Lett., 35, pp. 792-795 (1979).
71. W.T. Tsang and A.Y. Cho, "Molecular Beam Epitaxial Writing of Patterned GaAs Epilayer Structures," Appl. Phys. Lett., 32, pp. 491-493 (1978).
72. W.T. Tsang and A.Y. Cho, "Growth of GaAs- $\text{Ga}_{1-x}\text{Al}_x\text{As}$  over Preferentially Etched Channels by Molecular Beam Epitaxy: A Technique for Two-Dimensional Thin-Film Definition," Appl. Phys. Lett., 30, pp. 293-296 (1977).
73. S. Nagata and T. Tanaka, "Self-Masking Selective Epitaxy by Molecular-Beam Method," J. Appl. Phys., 48, pp. 940-942 (1977).
74. W.C. Bellamy and A.Y. Cho, "Planar Isolated GaAs Devices Produced by Molecular Beam Epitaxy," IEEE Trans. Electron Devices, ED-23, pp. 481-484 (1976).
75. A.Y. Cho and H.C. Casey, Jr., "Properties of Schottky Barrier and p-n Junctions Prepared with GaAs- $\text{Al}_x\text{Ga}_{1-x}\text{As}$  Molecular Beam Epitaxial Layers," J. Appl. Phys., 45, pp. 1258-1264 (1974).
76. D.W. Covington and W.H. Hicklin, " $\text{p}^+$ -n Hyperabrupt GaAs Varactors Grown by Molecular Beam Epitaxy," Electron. Lett., 14, pp. 752-753 (1978).

77. A.Y. Cho, C.N. Dunn, R.L. Kuvass and W.E. Schroeder, "GaAs IMPATT Diodes Prepared by Molecular Beam Epitaxy," Appl. Phys. Lett., 25, pp. 224-226 (1974).
78. M.V. Schneider, R.A. Linke, and A.Y. Cho, "Low-Noise Millimeter-Wave Mixer Diodes Prepared by Molecular Beam Epitaxy (MBE)," Appl. Phys. Lett., 31, pp. 219-221 (1977).
79. E.L. Meeks, G.N. Hill, D.W. Covington, and W.B. Day, "Millimeter Mixer Diodes by Molecular Beam Epitaxy," M.B.E.78, First International Symposium on Molecular Beam Epitaxy, Paris (25-27 April 1978).
80. R.A. Linke, M.V. Schneider and A.Y. Cho, "Cryogenic Millimeter-Wave Receiver Using Molecular Beam Epitaxy Diodes," IEEE Trans. Microwave Theory Tech., MTT-26, pp. 935-938 (1978).
81. A.Y. Cho and D.R. Ch'en, "GaAs MESFET Prepared by Molecular Beam Epitaxy (MBE)," Appl. Phys. Lett., 28, pp. 30-31 (1976).
82. C.E.C. Wood, "Molecular Beam Epitaxial GaAs Layers for MESFET's," Appl. Phys. Lett., 29, pp. 746-748 (1976).
83. A.Y. Cho, J.V. DiLorenzo, B.S. Hewitt, W.C. Niehaus, W.O. Schlosser, and C. Radice, "Low-Noise and High-Power GaAs Microwave Field-Effect Transistors Prepared by Molecular Beam Epitaxy," J. Appl. Phys., 48, pp. 346-349 (1977).
84. S.G. Bandy, D.M. Collins and C.K. Nishimoto, "Low-Noise Microwave F.E.T.S Fabricated by Molecular-Beam Epitaxy," Electron. Lett., 15, pp. 218,219 (1979).
85. M. Wataze, Y. Mitsui, T. Shimanoe, M. Nakatani, and S. Mitsui, "High-Power GaAs F.E.T. Prepared by Molecular-Beam Epitaxy," Electron. Lett., 14, pp. 759-761 (1978).
86. J.V. DiLorenzo, W.C. Niehaus, and A.Y. Cho, "Nonalloyed and in situ Ohmic Contacts to Highly Doped n-Type GaAs Layers Grown by Molecular Beam Epitaxy (MBE) for Field-Effect Transistors," J. Appl. Phys., 50, pp. 951-954 (1979).
87. J.H. McFee (private communication).
88. R. Glang, R.A. Holmwood, and J.A. Kurtz in Handbook of Thin Film Technology, (L.I. Maissel and R. Glang, ed.) McGraw Hill, New York, Chap. 2, pp. 2-1 to 2-142 (1970).
89. R. Glang, *ibid*, Chap. 1, pp. 1-3 to 1-130.
90. D.J. Ashen, P.J. Dean, D.T.J. Hurle, J.B. Mullin, A.M. White, and P.D. Greene, "The Incorporation and Characterization of Acceptors in Epitaxial GaAs," J. Phys. Chem. Solids, 36, pp. 1041-1053 (1975).

91. J.D. Wiley, "Mobility of Holes in III-V Compounds," Semiconductors and Semimetals, (R.K. Willardson and A.C. Beer, ed.) Vol. 10, Academic Press, New York, pp. 91-174 (1975).
92. J. Lacombe, J.P. Duchemin, M. Bonnet, and D. Huyghe, "Schottky Mixer Diodes Made by a New Method," Electron. Lett., 13, pp. 472-473 (1977).
93. J.C. Irvin and N.C. Vanderwal, "Schottky Barrier Devices" in Microwave Semiconductor Devices and Their Circuit Applications (H.A. Watson, ed.) McGraw Hill, New York, pp. 340-369 (1969).
94. J.E. Davey (private communication).
95. R.J.M. Griffiths, I.B. Blenkinsop, D.R. Wight, "Preparation and Properties of GaAs Layers for Novel F.E.T. Structures," Electron. Lett., 15, pp. 629-630 (1979).
96. M.G. Adlerstein, R.N. Wallace, and S.R. Steele, "Millimeter-Wave GaAs Read IMPATT Diodes," IEEE Trans. Electron. Devices, ED-25, pp. 1151-1156 (1978).
97. R.I. Schwarz and E. Bonek, "Current-Tuned GaAs Schottky Barrier IMPATT Diodes for 60-96 GHz Operation," Electron. Lett., 14, pp. 812-814 (1978).
98. Final Report, Molecular Beam Epitaxial Materials Study for Microwave and Millimeter Wave Devices, Contract No. N00173-76-C-0372, Georgia Tech, Atlanta, Georgia (October 1978).
99. A.Y. Cho, "Impurity Profiles of GaAs Epitaxial Layers Doped with Sn, Si, and Ge Grown with Molecular Beam Epitaxy," J. Appl. Phys., 46, pp. 1733-1735 (1975).
100. K. Ploog and A. Fischer, "Surface Segregation of Sn During MBE of n-type GaAs Established by SIMS and AES," J. Vac. Sci. Technol., 15, pp. 255-259 (1978).
101. C.E.C. Wood, "Tin Incorporation in M.B.E. GaAs," M.B.E.78, First International Symposium on Molecular Beam Epitaxy, Paris (25-27 April 1978).
102. J. Pribetich, M. Chive, E. Constant, and A. Farayre, "Design and Performance of Maximum-Efficiency Single- and Double-Drift-Region GaAs IMPATT Diodes in the 3-18 GHz Frequency Range," J. Appl. Phys., 49, pp. 5584-5594 (1978).
103. D.W. Covington and E.L. Meeks, "Unintentional Dopants Incorporated in GaAs Layers grown by Molecular Beam Epitaxy," J. Vac. Sci. Technol., 16, pp. 847-850 (1979).
104. H. Morkoç and A.Y. Cho, "High-Purity GaAs and Cr-Doped GaAs Epitaxial Layers by MBE," J. Appl. Phys., pp. 6413-6416 (1979).

105. K. Nakai, K. Kitahara, A. Shibatomi, and S. Ohkawa, "Growth of Iron-Doped Epitaxial Layers for GaAs Field Effect Transistors," J. Electrochem. Soc., 124, pp. 1635-1640 (1977).
106. C.E.C. Wood and B.A. Joyce, "Tin-Doping Effects in GaAs Films Grown by Molecular Beam Epitaxy," J. Appl. Phys., 49, pp. 4854-4861 (1978).
107. W.V. McLevige, K.V. Vaidyanathan, B.G. Streetman, M. Ilegems, J. Comas, and L. Plew, "Annealing Studies of Be-Doped GaAs Grown by Molecular Beam Epitaxy," Appl. Phys. Lett., 33, pp. 127-129 (1978).
108. P.W. Yu, "Deep Emission Centers in Ge-Implanted GaAs," J. Appl Phys., 50, pp. 7165-7167 (1979).
109. L.J. van der Pauw, "A Method of Measuring Specific Resistivity and Hall Effect of Discs of Arbitrary Shape," Philips Res. Repts., 13, pp. 1-9 (1958).
110. W. Walukiewicz, L. Lagowski, L. Jastrzebski, M. Lichtengteiger, and H.C. Gatos, "Electron Mobility and Free-Carrier Absorption in GaAs: Determination of the Compensation Ratio," J. Appl. Phys., 50, pp. 899-908 (1979).
111. G.E. Stillman, C.M. Wolfe, and J.O. Dimmock, "Far-Infrared Photoconductivity in High Purity GaAs," Semiconductors and Semimetals, 12, edited by R.K. Willardson and A.C. Beer, Academic Press, New York, pp. 169-290 (1977).
112. T. Katoda and T. Sugano, "Hall Effect, Schottky Barrier Capacitance, and Photoluminescence Spectra Measurements for GaAs Epitaxial Layers and Their Correlation," J. Electrochem. Soc., 121, pp. 1066-1073 (1974).
113. R.L. Petritz and W.W. Scanlon, "Mobility of Electrons and Holes in the Polar Crystal, PbS," Phys. Rev., 97, pp. 1620-1626 (1955).
114. R.W. Haisty, "On the Temperature Dependence of the Iron Acceptor Level in GaAs," Appl. Phys. Lett., 7, pp. 208-210 (1965).
115. G.A. Allen, "The Activation Energies of Chromium, Iron and Nickel in Gallium Arsenide," Brit. J. Appl. Phys. (J. Phys. D.), 1, pp. 593-602 (1968).
116. W. Plesiewicz, "Photo Hall Effect in Semi-Insulating GaAs:Fe," phys. stat. sol., 16, pp. 485-491 (1973).
117. V.I. Fistul', L. Ya. Pervova, É.M. Omelyánovskii, E.P. Rashevskaya, N.N. Solov'ev, and O.V. Pelevin, "Properties of Iron-Doped Semi-insulating Gallium Arsenide," Sov. Phys. Semicomd., 8, pp. 311-316 (1974).
118. D.W. Covington, E.L. Meeks, and W.H. Hicklin (unpublished report, 31 July 1979).

119. S.M. Sze, Physics of Semiconductor Devices, Wiley Interscience, New York, p. 29 (1969).
120. Y. Mori and N. Watanabe, "A New Etching Solution System,  $H_3PO_4-H_2O_2-H_2O$ , for GaAs and Its Kinetics," J. Electrochem. Soc., 125, pp. 1510-1514 (1978).
121. H.H. Wieder, "Electrical and Galvanomagnetic Measurements on Thin Films and Epilayers," Thin Solid Films, 31, pp. 123-128 (1976).
122. K. Kajiyama, Y. Mizushima, and S. Sakata, "Schottky Barrier Height of n- $In_xGa_{1-x}As$  Diodes," Appl. Phys. Lett., 23, pp. 458-459 (1973).
123. D.V. Morgan and J. Frey, "Increasing the Effective Barrier Height of Schottky Contacts to n- $In_xGa_{1-x}As$ ," Electron. Lett., 14, pp. 737-739 (1978).
124. T.B. Reed, Free Energy of Formation of Binary Compounds, MIT Press, Cambridge, Massachusetts, pp. 66,67 (1971).
125. A. Christou, "Semiconductor Measurement Technology: Automated Scanning Low-Energy Electron Probe (ASLEEP) for Semiconductor Wafer Diagnostics," NBS Special Publication 400-30, U.S. Gov. Printing Office, Washington, D.C. (1978).
126. T.P. Pearsall, R. Bisaro, P. Merenda, G. Laurencin, R. Ansel, J.P. Portal, C. Houlbert, and M. Quillec, "The Characterization of  $Ga_{0.47}In_{0.53}As$  Grown Lattice-Matched on InP Substrates," Gallium Arsenide and Related Compounds, 1978, (Inst. Phys. Conf. Ser. No. 45, London, 1979) pp. 94-102.
127. R.E. Nahory, M.A. Pollack, and J.C. DeWinter, "Growth and Characterization of Liquid-Phase Epitaxial  $In_xGa_{1-x}As$ ," J. Appl. Phys., 46, pp. 775-782 (1975).
128. K. Takahashi, T. Morizumi, and S. Shirosé, "Preparation and Properties of  $In_xGa_{1-x}As$  Single Crystals by Solution Growth Technique," J. Electrochem. Soc., 118, pp. 1639-1644 (1971).
129. B.J. Baliga and S.K. Ghandhi, "Growth and Properties of Heteroepitaxial GaInAs Alloys on GaAs Substrates Using Trimethylgallium, Triethylindium, and Arsine," J. Electrochem. Soc., 122, pp. 683-687 (1975).
130. M. Glicksman, R.E. Enstrom, S.A. Mittleman, and J.R. Appert, "Electron Mobility in  $In_xGa_{1-x}As$  Alloys," Phys. Rev. B., 9, pp. 1621-1626 (1974).
131. S.B. Hyder, "Thin Film Epitaxial Growth of  $In_xGa_{1-x}As$  on GaAs," J. Electrochem. Soc., 123, pp. 1503-1508 (1976).

132. A.R. Calawa, "MBE Growth of GaAs and InGaAs," MBE Workshop, University of Illinois at Urbana-Champaign, IL (20-21 September 1979).
133. R.W. Conrad, P.L. Hoyt, and D.D. Martin, "Preparation of Epitaxial  $\text{Ga}_x\text{In}_{1-x}\text{As}$ ," J. Electrochem. Soc., 114, pp. 164-166 (1967).